

A Study of Decays of the Tau Lepton with Charged Kaons

by

Sherry Meleah Jean Towers B.Sc., M.Sc.

A thesis submitted to the Faculty of Graduate Studies and Research in partial
fulfilment of the requirements for the degree of Doctor of Philosophy

Ottawa-Carleton Institute of Physics
Department of Physics, Carleton University
Ottawa, Ontario, Canada

January, 2000

©copyright, 2000

Sherry Towers



National Library
of Canada

Acquisitions and
Bibliographic Services

395 Wellington Street
Ottawa ON K1A 0N4
Canada

Bibliothèque nationale
du Canada

Acquisitions et
services bibliographiques

395, rue Wellington
Ottawa ON K1A 0N4
Canada

Your file *Votre référence*

Our file *Notre référence*

The author has granted a non-exclusive licence allowing the National Library of Canada to reproduce, loan, distribute or sell copies of this thesis in microform, paper or electronic formats.

The author retains ownership of the copyright in this thesis. Neither the thesis nor substantial extracts from it may be printed or otherwise reproduced without the author's permission.

L'auteur a accordé une licence non exclusive permettant à la Bibliothèque nationale du Canada de reproduire, prêter, distribuer ou vendre des copies de cette thèse sous la forme de microfiche/film, de reproduction sur papier ou sur format électronique.

L'auteur conserve la propriété du droit d'auteur qui protège cette thèse. Ni la thèse ni des extraits substantiels de celle-ci ne doivent être imprimés ou autrement reproduits sans son autorisation.

0-612-48355-X

Abstract

Precise studies of the decays of the tau (τ^-) lepton have been made possible by the availability of large, low-background tau samples, such as those produced in e^+e^- collisions at the Z^0 resonance at LEP. This thesis describes a study of tau decay modes containing charged kaons, using data collected by the OPAL experiment at LEP. A charged kaon (K^-) is a meson composed of a bound state of a strange quark and an up anti-quark, and has a mass of $0.492 \text{ GeV}/c^2$. Another example of a meson is the charged pion (π^-), which is composed of a down quark and an up anti-quark, and has a mass of $0.139 \text{ GeV}/c^2$. Charged pions are often produced in tau decays, but decays including charged kaons only occur approximately 5% of the time. One way to experimentally distinguish between the predominant charged pions and the kaons in tau decays is to determine the energy lost by the particle as it traverses a gas and ionises molecules in that gas: the energy lost in this process is a function of the particle mass.

The OPAL detector provides precise measurements of the ionisation energy loss of charged particles, and it is primarily this capability that is exploited in this work to study these tau final states and obtain precise measurements of their branching ratios.

Acknowledgements

There are a number of people who have made the completion of this degree possible. Foremost is my advisor, Dean Karlen. The chance to learn under his tutelage was one of my primary reasons for deciding to pursue my doctoral studies at Carleton. As a mentor, Dean has more than lived up to my expectations, and I would have been hard pressed to find anyone else in the world who could have given me such a thorough and excellent education, both in physics, and in the statistical analysis of data.

I am grateful to Michael Hauschild for freely sharing his dE/dx expertise, and I am also deeply indebted to the high energy physics group at the University of Pennsylvania (in particular, Nigel Lockyer, Joe Kroll, and Brig Williams) for giving me the office space I needed to complete my degree, and especially for making me feel exactly like one of their own.

The funding of this research by grants from the Natural Sciences and Engineering Research Council (NSERC) is appreciated. In addition, the personal financial support provided by an NSERC Postgraduate Scholarship is gratefully acknowledged.

Last, but certainly not least, I would like to thank my husband, Matthew, for all his love and support over the years (and for heavily subsidising the last two years of this degree). Through ten years together we have lived in five different cities, amassed six degrees between us, and had one beautiful daughter. Time will only tell what the next ten years will hold...

Candidate's Contributions to this Thesis

The analyses presented in this thesis represent work done almost exclusively by the author. One of the most critical aspects of these studies is the calibration of the charged particle ionisation energy loss recorded by OPAL detector, the quantity that is used in these analyses to identify charged kaons. I have written several OPAL internal documents on the ionisation energy loss parameterisation and optimisation procedure that I developed for these studies, information that has since been used in other OPAL tau analyses that rely on charged particle identification.

A second key technical aspect of these analyses is the development of Monte Carlo algorithms to model the tau decay chains of interest. OPAL is among the first experiments to precisely examine many of the tau decay final states that include charged kaons, and the available Monte Carlo generators do not adequately model these decays. Thus I have had to develop specialised Monte Carlo algorithms to address this issue. The Monte Carlo techniques and software I have established have also been used in other OPAL analyses that study tau decays to charged and neutral kaons.

This thesis is dedicated to the memory of my paternal grandmother, Ruth Eileen Towers. As a young woman, she studied to become a nurse, but gave up her career to become a full-time mother and housewife when she married my grandfather in the 1930's. She always kept a lifelong interest in learning, however, which only intensified after the death of my grandfather in 1980. During the next six years, before her own untimely death in 1986, she enrolled in a university degree english programme, travelled widely, and allowed her longtime interest in artistic pursuits to bloom.

In her own quiet way, she always encouraged me to follow my interests, and I think that she would be proud of what I have so far achieved in life, academically and otherwise.

Contents

Abstract	vii
Acknowledgements	vii
1 Introduction	1
1.1 The Standard Model	2
1.2 Quantum Chromodynamics	5
1.3 Quantum Electrodynamics	8
1.4 Weak Interactions	8
1.5 Success of the Standard Model	11
2 The Tau Lepton	14
2.1 Tau Mass	17
2.2 Tau Lifetime	18
2.3 Leptonic Tau Decays	19
2.4 Semi-Leptonic Tau Decays	21
2.4.1 Tau Decays to Final States with Charged Kaons	24
3 LEP and the OPAL Detector	30
3.1 The LEP Synchrotron	30
3.2 The OPAL Detector	33
3.2.1 Tracking Detectors	34
3.2.2 Time-of-Flight	46
3.2.3 The Electromagnetic Calorimeter	46

3.2.4	The Hadronic Calorimeter	47
3.2.5	The Muon Chambers	48
4	Calibration of Ionisation Energy Loss	49
4.1	dE/dx in the Tau Decay Environment	51
4.1.1	dE/dx in the Three-Prong Tau Decay Environment	59
5	The OPAL Data Sample	64
5.1	The Tau-Pair Sample	64
6	Monte Carlo Simulation	74
7	One-Prong Branching Ratios	78
7.1	Event Selection	79
7.2	Inclusive $\tau^- \rightarrow \nu_\tau K^- \geq 0h^0$ Branching Ratio	79
7.2.1	The Branching Ratio Calculation	81
7.2.2	dE/dx Systematic Studies	87
7.2.3	Efficiency Correction	88
7.2.4	Background Correction	89
7.3	Exclusive Branching Ratios	89
7.3.1	Corrections to the Modelling of E/p and N_{clus}	91
7.3.2	The $\tau^- \rightarrow \nu_\tau K^-$ Branching Ratio	94
7.3.3	dE/dx Systematic Error	97
7.3.4	Systematic Uncertainty Associated with the Efficiency Cor- rection	99
7.3.5	Systematic Uncertainty Associated with the Modelling of E/p and N_{clus}	100
8	Three-Prong Branching Ratios	102
8.1	Event Selection	102
8.1.1	Inclusive Candidate Samples (no π^0 Identification)	103

8.1.2	π^0 Identification	104
8.2	Estimation of the Number of Kaons in the Samples	106
8.3	The Branching Ratio Calculation	109
8.4	dE/dx Systematic Studies	111
8.5	Efficiency Correction	115
8.6	Kaon Background Correction	116
9	Three-Prong Resonant Structure	118
9.1	Event Selection	119
9.2	$\tau^- \rightarrow \nu_\tau K^- \pi^- \pi^-$	120
9.2.1	$\tau^- \rightarrow \nu_\tau K_1^-$	123
9.3	$\tau^- \rightarrow \nu_\tau K^- \pi^- K^-$	127
10	Summary of Results and Conclusions	132
10.1	One-prong Tau Decays	132
10.2	Three-prong Tau Decays	133
10.3	Conclusions	136
A	Phenomenological Parameterisation of Resonant Amplitudes	139
A.1	Decay of a Resonance to Two Stable Particles	140
A.2	Decay of a Resonance to a Stable Particle and a Secondary Resonance	140
B	OPAL Track Parameters	142
C	The OPAL Collaboration	145

List of Tables

1.1	The known leptons and quarks	3
2.1	Measurements and theoretical predictions for various tau semi-leptonic branching ratios	27
2.2	Measurements and theoretical predictions for tau branching ratios to allowed final states which include charged kaons	28
2.3	Forbidden tau decays with charged kaons in the final state	29
3.1	Some properties of the OPAL tracking chambers	36
3.2	Energy resolution of the electromagnetic calorimeter	47
5.1	Integrated luminosity delivered by LEP between the years 1990 and 1995	65
5.2	Biases introduced by the tau-pair selection	67
6.1	Intermediate resonant structure assumptions made in the generation of simulated signal tau decay modes	77
7.1	Hadron composition of the one-prong tau decay sample	82
7.2	One-prong inclusive branching ratio and sources of systematic uncertainty	86
7.3	Branching ratios and efficiencies used to extract the $\tau^- \rightarrow \nu_\tau K^- \geq 0h^0$ and $\tau^- \rightarrow \nu_\tau \pi^- \geq 0h^0$ branching ratios	90
8.1	The number of kaons within each data sample	112

8.2	Summary of the branching ratio central values and sources of uncertainty	113
8.3	Correlations between the exclusive branching ratios	114
9.1	Summary of the binned likelihood fit to the $\tau^- \rightarrow \nu_\tau K^- \pi^- \pi^+$ candidates	126
9.2	Summary of the binned likelihood fits to the $\tau^- \rightarrow \nu_\tau K^- \pi^- K^+$ candidates	130
10.1	Branching ratio summary of one-prong tau decays with charged kaons in the final state	134
10.2	Branching ratio summary of three-prong tau decays with charged kaons in the final state	137

List of Figures

1.1	First and second order Feynman diagrams used in the calculation of low-energy electron/muon scattering	6
1.2	Measured cross-sections for $e^+e^- \rightarrow \text{hadrons}$ and $e^+e^- \rightarrow \mu^+\mu^-$ at various centre-of-mass energies	13
2.1	Behaviour of the $e^+e^- \rightarrow \tau^+\tau^-$ cross-section near threshold	16
2.2	The world average tau lifetime versus the $\tau^- \rightarrow e^-\bar{\nu}_e \nu_\tau$ branching ratio	20
2.3	Fully-leptonic decays of the τ^- and μ^- leptons	21
2.4	Semi-leptonic decay of the τ^-	23
3.1	LEP and environs	32
3.2	The OPAL detector	35
3.3	Schematic of the OPAL jet chamber	38
3.4	Typical distribution of the sampled energy loss in the OPAL jet chamber	40
3.5	Ionisation energy loss resolution in the OPAL detector as a function of $N_{dE/dx}$	41
3.6	Typical jet chamber wire response within a dense track environment	43
3.7	Charge saturation within the jet chamber	45
4.1	Ionisation energy loss in the OPAL detector as a function of momentum	52
4.2	dE/dx resolution for various particle detectors	53

4.3	Measured dE/dx versus β for one-prong control samples	55
4.4	Momentum versus $Q = -\log(1 - \beta^2)$ for various particle species . . .	56
4.5	Stretch dE/dx of the $\tau^- \rightarrow \mu^- \bar{\nu}_\mu \nu_\tau$ sample	57
4.6	dE/dx versus ϕ for $e^+e^- \rightarrow \mu^+\mu^-$ events	58
4.7	dE/dx of tracks in one-prong tau decays before and after corrections	60
4.8	Stretch dE/dx of $\tau^- \rightarrow \nu_\tau \pi^- \pi^- X^+(\pi^0)$ candidates	62
4.9	dE/dx of hadrons from three-prong tau decays before and after corrections	63
5.1	A typical $e^+e^- \rightarrow \tau^+\tau^-$ event in the OPAL detector	68
5.2	Another typical $e^+e^- \rightarrow \tau^+\tau^-$ event in the OPAL detector	69
5.3	A typical hadronic Z^0 decay in the OPAL detector	70
5.4	A typical cosmic ray event in the OPAL detector	71
5.5	A typical $e^+e^- \rightarrow e^+e^-$ event in the OPAL detector	72
5.6	A typical $e^+e^- \rightarrow \mu^+\mu^-$ event in the OPAL detector	73
7.1	Stretch dE/dx distribution of tracks in the $\tau^- \rightarrow \nu_\tau h^- \geq 0h^0$ candi- date sample	83
7.2	Momentum distribution of charged hadrons in the one-prong tau decay sample	84
7.3	E/p and N_{clus} distributions of $\tau^- \rightarrow \nu_\tau \pi^- \geq 0h^0$ decays	92
7.4	E/p distribution of one-prong tau decays with charged kaons	98
8.1	$E/\sum p$ distributions for Monte Carlo generated $\tau^- \rightarrow \nu_\tau K^- \pi^- \pi^+(\pi^0)$ and $\tau^- \rightarrow \nu_\tau K^- \pi^- K^+(\pi^0)$ events	105
8.2	Stretch dE/dx distribution of the like-sign and unlike-sign samples	108
8.3	Efficiency as a function of momentum for signal events to contribute to the candidate samples	117
9.1	Invariant mass distributions of the data $\tau^- \rightarrow \nu_\tau K^- \pi^- \pi^+$ candidate sample	124

9.2	Invariant mass distributions of the data $\tau^- \rightarrow \nu_\tau \pi^- \pi^- K^+$ candidate sample	125
9.3	Invariant mass distributions of the $\tau^- \rightarrow \nu_\tau K^- \pi^- K^+$ candidate sample	131
B.1	Geometry associated with the OPAL track parameters	143

Chapter 1

Introduction

This thesis describes a study of the decays of the tau lepton with one or three charged mesons in the final state, where at least one of the mesons contains a strange quark. This study is based on data collected by the OPAL detector at the LEP e^+e^- colliding beam accelerator at CERN, which produced large numbers of $\tau^+\tau^-$ pairs at the Z^0 resonance. This large, low-background sample of tau data, combined with the excellent charged particle identification capabilities of the OPAL detector, enabled this study to extract precise branching ratios for the tau lepton to these final states, and allowed one of the more comprehensive studies of the properties of the three charged meson ('three-prong') final states to-date.

Chapters 1 and 2 of this thesis provide the background material necessary for the discussion of this analysis. They include an overview of the Standard Model, followed by a description of the properties of the tau lepton, and a summary of previous measurements related to the work presented here. Chapter 3 describes the LEP collider and the OPAL detector, with special emphasis on those portions of the detector most critical to charged particle identification. Chapter 4 details the parameterisation of the ionisation energy loss in the OPAL detector, the quantity that is used in this analysis to distinguish between the various types of charged particles produced in tau decays.

Chapter 5 describes the data sets used in this analysis, while Chapter 6 details

the Monte Carlo simulation of the decays of interest to this study. Chapters 7 and 8 outline the methods used to determine the branching ratios of the tau lepton to these final states, and Chapter 9 describes the study of the resonant properties of the three-prong final states. Chapter 10 summarises the results of the analyses and compares them to the current world average results, and also to theoretical predictions.

1.1 The Standard Model

Until the early 1930's, physicists viewed all matter as consisting of only three 'fundamental' particles: the electron, the proton, and the neutron. At that time, quantum theory accounted well for the structure of the atom and for the radioactive alpha decay of nuclei. The neutrino had yet to be observed, but had been incorporated by Fermi into a successful theory of neutron beta decay.

Less than two decades later, however, the discovery of three new particles (the muon, pion, and positron) in cosmic ray and nuclear reactor experiments changed forever this simplified view of elementary particles and their interactions. Since this epiphany, many more particles (fundamental and otherwise) have been discovered, and classification schemes based upon common properties of these particles have been used to arrange them into groups. For instance, one can classify fundamental particles according to their spin: it has been found that all fundamental constituent particles of matter are fermions with spin $1/2$, while those that mediate the interactions between them are bosons with spin 1.

There are four known forces through which particles can interact: the strong force, the electromagnetic force, the weak force, and gravity. The Standard Model describes how the fundamental fermions interact via the first three of these four forces (no satisfactory quantum theory yet exists for gravity, and, in addition, the force of gravity is so weak that it is irrelevant for high energy physics processes). All known fundamental fermions are listed in Table 1.1 and are classified in the

Standard Model model by considering the forces experienced by them: the leptons interact via the electromagnetic (EM) and weak forces only, whereas the quarks can experience the strong, electromagnetic, and weak interactions. The neutral Z^0 and the charged W^\pm bosons mediate the weak force, while the photon and the gluon mediate the electromagnetic and strong forces, respectively.

The leptons and quarks are both grouped into three 'families':

$$\begin{pmatrix} e^- \\ \nu_e \end{pmatrix} \quad \begin{pmatrix} \mu^- \\ \nu_\mu \end{pmatrix} \quad \begin{pmatrix} \tau^- \\ \nu_\tau \end{pmatrix} \quad (1.1)$$

$$\begin{pmatrix} u \\ d \end{pmatrix} \quad \begin{pmatrix} c \\ s \end{pmatrix} \quad \begin{pmatrix} t \\ b \end{pmatrix}$$

where, in general, each family is heavier than the former, but all otherwise share similar properties. The number of such families is not predicted by the Standard Model, but experimental evidence indicates that there are only these three.

	name	symbol	charge [e]	mass [MeV/c ²]	interactions
LEPTONS	electron	e^-	-1	0.511	EM, weak
	muon	μ^-	-1	106	EM, weak
	tau	τ^-	-1	1777	EM, weak
	electron neutrino	ν_e	0	$< 15 \times 10^{-6}$	weak
	muon neutrino	ν_μ	0	< 0.17	weak
	tau neutrino	ν_τ	0	< 18	weak
QUARKS	up	u	+2/3	~ 5	strong, EM, weak
	down	d	-1/3	~ 10	strong, EM, weak
	strange	s	-1/3	~ 100	strong, EM, weak
	charm	c	+2/3	~ 1200	strong, EM, weak
	bottom	b	-1/3	~ 4300	strong, EM, weak
	top	t	+2/3	$173.8 \pm 5.2 \text{ GeV}/c^2$	strong, EM, weak

Table 1.1: The known leptons and quarks. The corresponding anti-particles have opposite charges but equal masses. Masses are taken from [1].

Particle interactions in the Standard Model are governed by various conservation laws. For instance, in this model each lepton is assigned a lepton number $+1$, with anti-leptons having lepton number -1 . It is found that lepton number is always conserved in all interactions. Similarly, all quarks in the Standard Model are assigned a 'baryon' number of $1/3$ ($-1/3$ for anti-quarks), and it is found that the total baryon number is also conserved in all interactions. Additional global conservation laws in particle interactions include conservation of charge, energy, momentum, and angular momentum. Other conservation laws specific to the strong, electromagnetic, and weak interactions will be discussed in the following sections. In general, any conceivable particle interaction can occur, unless it is expressly forbidden by some conservation law.

The calculational framework of the Standard Model of particle interactions is built around a quantized, relativistically invariant theory known as quantum field theory. In this scheme, 'fields' are mathematical objects used to describe particles and their interactions. Calculations of particle interaction observables cannot generally be performed exactly in field theories, and thus perturbative expressions are usually used to yield approximate estimates instead. Although the mathematical expressions for the terms in the resulting perturbation series can be rather complicated, their structure is such that they can be represented by graphs, which are referred to as Feynman diagrams. These diagrams can be useful in visualizing the particle interactions, but further, they are a calculational aid to writing down the terms in the perturbative expansion, as each element of every graph has an associated well-defined term in the mathematical expression of the perturbation series.

Figure 1.1 shows examples of Feynman diagrams used in the calculation of the interaction probability in electron/muon elastic scattering, an electromagnetic process. Figure 1.1(a) represents the lowest order or 'tree-level' diagram, and Figure 1.1(b) displays the second order diagrams for this process. The terms in the perturbation series for the interaction probability calculation corresponding to

the diagrams in Figure 1.1(b) only yield a correction to the tree-level calculation of order 10% or less. Higher order terms contribute even less.

Many symmetries are observable in the interactions of fundamental particles and the mathematical formalism that describes such symmetries is known as group theory. Collections of particle fields that yield the same predictions for observables when input to the interaction Lagrangian are classified into groups under this formalism, and transformations that map (or ‘rotate’) one field in a group into another field belonging to the same group are known as gauge transformations. If the gauge transformations for a particular group of fields can be represented as hermitian $N \times N$ matrices, the group is known as a unitarity group of degree N , or $U(N)$. If, in addition, the matrices are traceless, the group is known as a special unitarity group, or $SU(N)$.

The following sections describe the strong, electromagnetic, and weak quantum field theories and the symmetries inherent in each. These three theories, taken together, form the Standard Model.

1.2 Quantum Chromodynamics

The theory of quark and gluon interactions via the strong force is known as quantum chromodynamics, or QCD. In this scheme, every quark has an associated ‘colour’ charge, which can either be red, green, or blue. The colours are nomenclature only, and bear no relation to the real colours of everyday life. Since the definition of which colour is which is arbitrary, the observable physical properties of the strong interaction must be invariant under ‘rotations’ in colour space, which corresponds to invariance under $SU(3)$ gauge transformations. In addition to this, the properties of this interaction are also invariant under parity transformations (that is to say, $\vec{x} \rightarrow -\vec{x}$ and $t \rightarrow t$) and charge conjugation (particle \rightarrow anti-particle).

The mediators of the force between coloured particles are massless vector bosons called gluons. The gluons also carry colour charge, and thus can self-

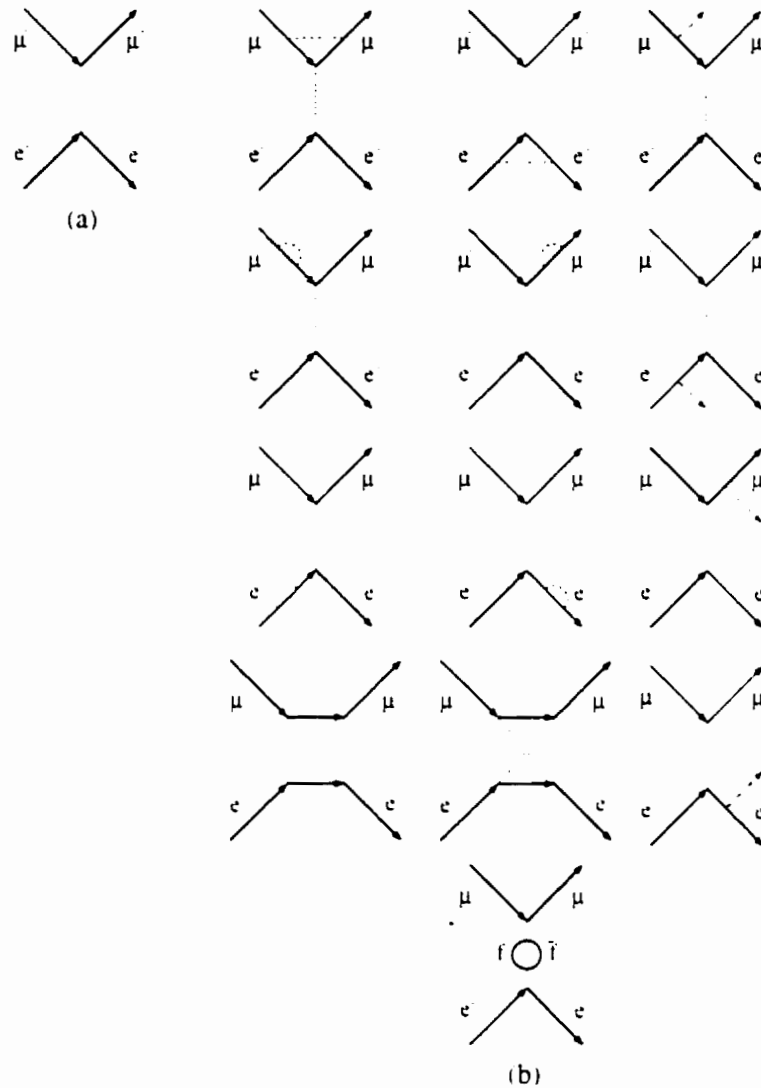


Figure 1.1: (a) shows the first-order ('tree-level') diagram used in the calculation of the elastic electron/muon scattering probability via the exchange of a photon, indicated by the dashed line. (b) shows the second-order diagrams. The $f\bar{f}$ loop in the bottom diagram in (b) represents the creation and annihilation of a virtual charged fermion pair. The terms in the perturbation series for the calculation corresponding to the diagrams in (b) only yield a correction to the tree-level calculation of order 10% or less. The time axis in all diagrams points to the right.

interact. A direct result of this is the phenomenon known as asymptotic freedom of quarks: as quarks move apart, the strength of the quark/gluon coupling increases, and further separation will cause a quark-antiquark pair to be produced. The result is that quarks are only observed in nature in colourless bound states with other quarks and anti-quarks, called hadrons. Hadrons consisting of a quark/anti-quark pair or three quarks are called mesons and baryons, respectively. More complicated combinations of quarks and gluons may possibly form bound states, but such objects have yet to be positively identified.

Like any quantum-mechanical bound system, combinations of quarks forming hadrons will have discrete energy spectra corresponding to the different modes of quark excitations, rotations, vibrations, etc. These discrete states correspond to the observable hadron states. In the case of a quark and an anti-quark forming a meson, the total spin J of the meson is obtained from the vector sum of the total intrinsic spin S of the quarks and their relative orbital angular momentum L . Different meson states can thus be classified using spectroscopic notation, $^{2S+1}L_J$. The 1S_0 $L = 0$ ground state mesons composed of the light u and d quarks are the charged and neutral pions, π^\pm and π^0 . Ground state mesons containing a strange quark are nearly four times heavier than the pions, and are called the charged and neutral kaons, K^\pm , K^0 , and \bar{K}^0 .

Occasionally, the term ‘SU(3) flavour symmetry’ is used when discussing hadrons composed of u , d , and/or s quarks (such as pions and kaons). This phrase refers to the exact symmetry which would be observed in such hadron states if the u , d , and s quarks all had exactly the same mass. This is not actually true, and thus SU(3) flavour symmetry is only approximate, but is nevertheless sometimes useful when deriving theoretical predictions for various observables of these states. It is completely unrelated to QCD colour SU(3), which is an exact symmetry of fundamental origin.

1.3 Quantum Electrodynamics

Quantum electrodynamics (QED) is a field theory with underlying $U(1)$ gauge symmetry, and is perhaps the most familiar of all field theories, as it describes the interaction of charged particles with photons. Like the strong interaction, the electromagnetic interaction is invariant under parity transformations and charge conjugation. Unlike the strong interaction, however, the photon does not carry electric charge, and therefore does not self-interact. As a direct result, the electromagnetic coupling strength decreases as two charges are pulled apart.

1.4 Weak Interactions

The weak interaction is classified into the charged weak interaction, mediated by the W^\pm gauge bosons, and the neutral weak interaction, mediated by the Z^0 gauge boson.

It was found in early nucleon β -decay experiments that the W^- boson preferentially couples to leptons and quarks which have their spins, $\vec{\sigma}$, opposed to their momentum vectors, \vec{p} . Such leptons and quarks are referred to as 'left-handed'.¹ This chiral nature of the charged weak interaction implies that it is not invariant under parity transformations, because such transformations do not change the spin of a particle, but do change the momentum (and thus a left-handed particle becomes a right-handed particle). For similar reasons, the charged weak interaction is also not invariant under charge conjugation. However, to a good approximation, the interaction is invariant under a combination of both charge conjugation and parity (CP) transformations.

In analogy to the colour charge of the strong interaction, and the electric charge of the electromagnetic interaction, the weak interaction conserves weak hypercharge, T_3^f . The left-handed leptons and quarks are therefore classified as

¹The W also preferentially couples to right-handed anti-leptons and right-handed anti-quarks.

follows:

$$\begin{pmatrix} e^- \\ \nu_e \end{pmatrix}_L \quad \begin{pmatrix} \mu^- \\ \nu_\mu \end{pmatrix}_L \quad \begin{pmatrix} \tau^- \\ \nu_\tau \end{pmatrix}_L$$

$$\begin{pmatrix} u \\ d' \end{pmatrix}_L \quad \begin{pmatrix} c \\ s' \end{pmatrix}_L \quad \begin{pmatrix} t \\ b' \end{pmatrix}_L \quad . \quad (1.2)$$

where the upper and lower members of each doublet have $T_3^f = +1/2$ and $T_3^f = -1/2$, respectively.² The d -type quarks listed in Equation 1.2 are related to the quark states that participate in the strong interaction by a unitary transformation, parameterised by the Cabibbo-Kobayashi-Maskawa (CKM) matrix:

$$\begin{pmatrix} d' \\ s' \\ b' \end{pmatrix} = \begin{pmatrix} V_{ud} & V_{us} & V_{ub} \\ V_{cd} & V_{cs} & V_{cb} \\ V_{td} & V_{ts} & V_{tb} \end{pmatrix} \begin{pmatrix} d \\ s \\ b \end{pmatrix} .$$

For only two generations of quarks, the corresponding 2×2 matrix could be specified in terms of a single parameter, the Cabibbo mixing angle, θ_C , while for three generations, the full CKM matrix can be specified in terms of four parameters (three mixing angles and a single complex phase).

The definition of which charge is which in each left-handed weak doublet is arbitrary, thus the observable physical properties of the weak interaction must be invariant under ‘rotations’ in weak hypercharge space, which corresponds to invariance under $SU(2)$ gauge transformations.

There are three gauge bosons which must be introduced to achieve invariance of the weak interaction Lagrangian under $SU(2)$ rotations. In the simplest form of this theory, these gauge bosons must be massless to ensure that calculations of physical observables predicted by the theory remain finite. However, experimental

²The right-handed quarks and leptons are contained in singlets with $T_3^f = 0$.

evidence indicates that the W^\pm and Z^0 gauge bosons are some of the most massive particles yet discovered.

An additional curiosity of the first attempts at deriving a model of weak interactions was that the Z^0 gauge boson was hypothesized to couple to particles with either electric charge or non-zero weak hypercharge. This dual electromagnetic/weak nature of the Z^0 couplings suggested that perhaps electromagnetism and the weak interaction are aspects of a unified 'electroweak' theory, in a manner somewhat similar to the unified nature of the electric and magnetic interactions.

The formulation of a unified theory of the weak and electromagnetic interactions in the 1960's by Glashow, Weinberg, and Salam [2] addressed the latter of these issues. Again, in its simplest form, this theory still required that the gauge bosons be massless. However, Higgs showed how the addition of a complex scalar doublet of fields (and thus four additional degrees of freedom) to the electroweak interaction Lagrangian could solve this problem [5] [6]: it was shown that the gauge bosons would couple to this scalar doublet in a way which produced the required effective mass terms in the Lagrangian for the W^\pm and Z^0 bosons (using three of the four extra degrees of freedom), while leaving the photon massless. In addition, the leptons and quarks would also couple to the added scalar doublet with a strength proportional to the fermion mass, and in a way which would produce mass terms in the interaction Lagrangian for the fermions. The values of the fermion masses, however, are not predicted by electroweak theory, and can only be determined by experiment. In the most basic form of electroweak theory, the W^\pm , Z^0 , and photon are hypothesized to couple to all three lepton families equally, regardless of mass, a phenomenon referred to as 'lepton universality'. There is no corresponding 'quark universality' of the weak interaction because the quark states that participate in the weak interaction are not the same as the quark states that participate in the strong interaction.

The fourth degree of freedom added by the Higgs scheme should be observable as a neutral scalar particle, called the Higgs boson. Electroweak theory again

places no constraints on the mass of this boson, and it has yet to be observed. Calculations that relate the mass of the Higgs to experimental constraints on other Standard Model parameters, however, indicate that the Higgs boson mass is about 170_{-80}^{+80} GeV/ c^2 [7]. Despite the fact that the Higgs boson has yet to be observed, the electroweak model has been dramatically successful.

1.5 Success of the Standard Model

In the 1970's, long before direct evidence for the W^\pm and the Z^0 was obtained from experiment, the first evidence for the weak neutral current was obtained from electron/neutrino scattering experiments. It was not until the early 1980's that direct evidence for W and Z bosons was obtained in data collected by the UA1 and UA2 experiments from proton/anti-proton collisions at the super-proton synchrotron (SPS) accelerator at CERN [8][9]. The estimates of the W^\pm and Z^0 masses obtained from these data were in agreement with the electroweak predictions, confirming the success of the Standard Model.

More precise tests of the Standard Model required the low-background and large data samples that could be obtained from a Z^0 factory, where electrons and positrons are collided at centre-of-mass energies close to the Z^0 mass [10]. Figure 1.2 shows the probability, or 'cross-section', for hadron and muon pair production in e^+e^- annihilation data collected over a wide range of centre-of-mass energies. Note the large resonant enhancement in the cross-section at centre-of-mass energies near the Z^0 mass. The overlaid curves in the figure represent the Standard Model prediction for the cross-section, and are in agreement with the data.

The Large Electron Positron (LEP) collider at CERN, which we will discuss in further detail in Chapter 3, began colliding e^+e^- beams at centre-of-mass energies close to the Z^0 mass in 1989, and continued in this mode until 1995. Most of the precision tests of aspects of the neutral and charged weak currents have been

derived from the data collected during this period by the experiments at LEP [11]. A good overview of these results, and similar results from other experiments, can be found on pages 63-67 of reference [1].

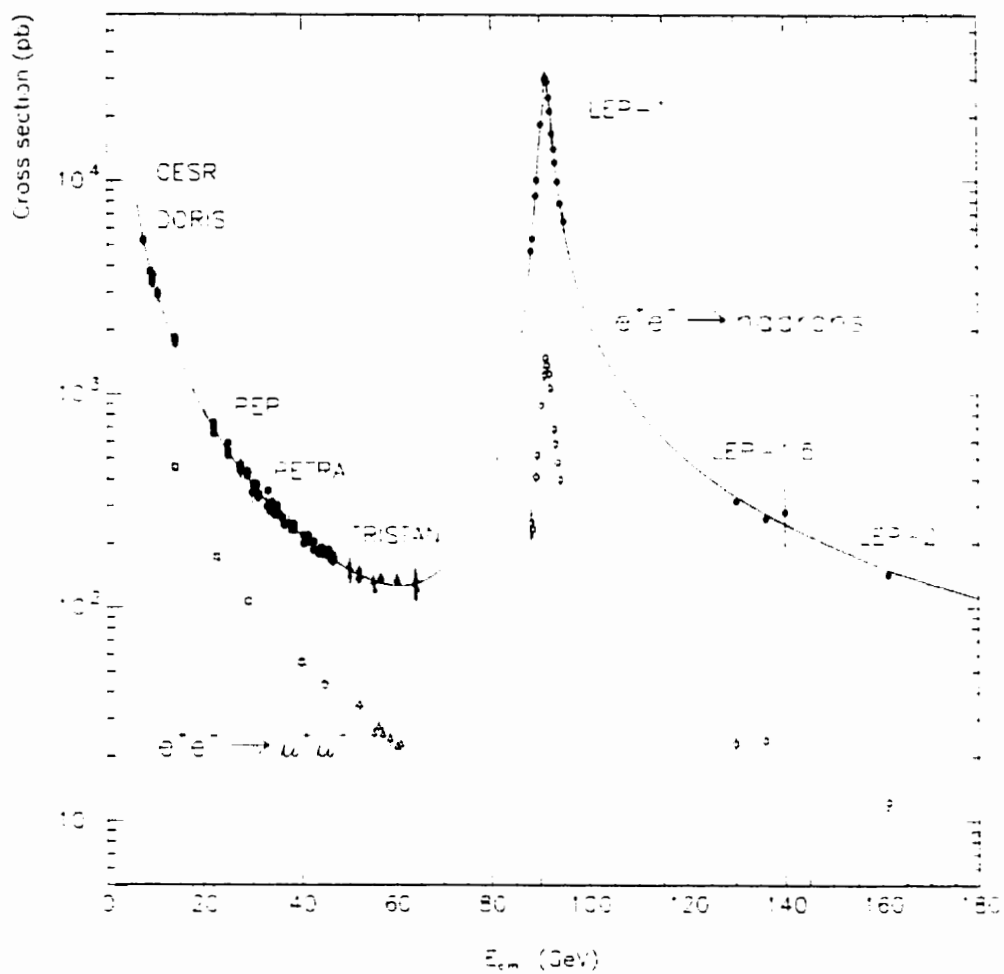


Figure 1.2: Measured cross-sections for $e^+e^- \rightarrow \text{hadrons}$ and $e^+e^- \rightarrow \mu^+\mu^-$ at various centre-of-mass energies. The overlaid curves represent the Standard Model predictions.

Chapter 2

The Tau Lepton

In 1995, Martin Perl received the Nobel prize in physics for his discovery of the heaviest known member of the lepton family, which he termed the τ , after the first letter of the Greek word $\tau\rho\iota\tau\omicron\nu$ (third), heralding the first evidence of a third, heavier generation of leptons and quarks.

This discovery was made in 1975 by searching for events of the type

$$e^+e^- \rightarrow \mu^\pm e^\mp (+ \text{ missing energy}) \quad (2.1)$$

in data collected by the MARK I detector at the SPEAR colliding beams facility of the Stanford Linear Accelerator Center (SLAC) [12] [13]. This experiment co-discovered the J/ψ meson in 1974 and was primarily occupied with the investigation of this, and the newly discovered charmed mesons, in e^+e^- collisions at centre-of-mass energies close to the $\psi(3770)$ resonance. Although relatively little was known about charmed mesons by 1975, they had never been observed to decay purely leptonically. Thus the detection of events in the reaction seen in Equation 2.1 could be viewed as indicative of the possible production and decay of a pair of new high-mass particles, $e^+e^- \rightarrow \tau^+\tau^-$.

In the initial search for the reaction shown in Equation 2.1, 105 events were found. The angular distribution of the muons and electrons in these events was

found to be consistent with that of decay products from a particle of fixed mass, and the momentum spectrum of the electrons and muons was used to show that it was very unlikely that the proposed fixed-mass parent particle was a boson. In addition, the electron and muon momentum distributions were consistent with those of particles originating from a parent particle that most likely decayed to three particles in the final state, two of which exited the detector undetected. Studies which systematically eliminated other possibilities for the undetected particles showed that they were most likely neutrinos. Since no $e^+e^- \rightarrow \mu^\pm e^\mp (+ \text{missing energy})$ events were observed for an e^+e^- centre-of-mass energy less than 3.8 GeV, it was determined that the mass of the parent particle was approximately 1.9 GeV.

The threshold behaviour of the cross-section for the production of $e^+e^- \rightarrow \tau^+\tau^-$ events in the MARK I data was found to be consistent with the production of spin 1/2, pointlike particles. An example of additional subsequent experimental evidence for this behaviour is shown in Figure 2.1, which shows the $e^+e^- \rightarrow \tau^+\tau^-$ production cross-section versus centre-of-mass energy of data collected by the DELCO detector in 1978 at the SPEAR electron-positron collider at SLAC [14]. Overlaid on this plot are the best fits to the DELCO data assuming the τ is a pointlike particle of spin 0, 1/2, and 1.

All studies of the $e^+e^- \rightarrow \mu^\pm e^\mp (+ \text{missing energy})$ events therefore indicated that, if they were to be explained by a single hypothesis, then they must have arisen from the production and decay of a pair of pointlike spin 1/2 particles, each of which decayed to a charged lepton and two neutrinos. The new particle was thus a candidate for being a heavy lepton. Acceptance of this new charged lepton was somewhat slow at first, but subsequent experiments (for instance [14]) confirmed that production of anomalous $e^+e^- \rightarrow \mu^\pm e^\mp (+ \text{missing energy})$ events occurred below the threshold for charm meson production, thus eliminating any lingering possibility that this phenomenon was somehow associated with purely leptonic charm meson decays. By the end of the 1970's, belief by the physics community in the existence of the tau lepton was widespread.

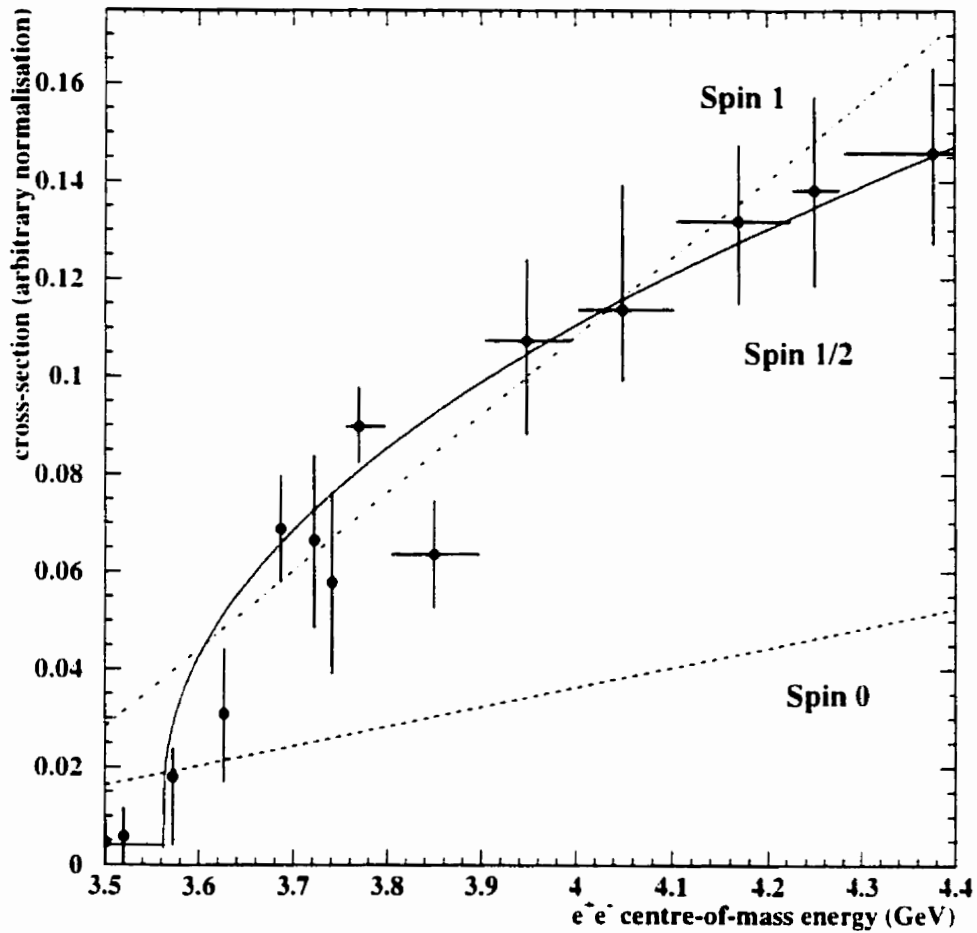


Figure 2.1: Behaviour of the $e^+e^- \rightarrow \tau^+\tau^-$ cross-section versus centre-of-mass energy of data taken by the DELCO collaboration [14]. The three fitted curves indicate the predicted threshold behaviour of a pointlike tau of different spins.

Since the confirmation of its discovery, the τ has provided important opportunities for testing fundamental aspects of the Standard Model, such as lepton universality and aspects of both the charged and neutral current weak interactions. Moreover, as the only lepton heavy enough to decay into hadrons, tau decays provide a favourable clean environment for the study of strong interaction phenomena, such as meson resonances, without the usual large non-resonant effects present in hadron collisions.

Although a complete overview of tau physics is beyond the scope of this thesis, the following sections describe the current status of experimental measurements and theoretical predictions for a few key properties of the tau lepton, including the tau mass, lifetime, and branching ratios. A ‘branching ratio’ is the probability that the tau will decay into a particular final state, and is the partial width of the tau to that final state divided by the total width. The total width of the tau is inversely proportional to the tau lifetime. Particular attention will be paid here to the semi-leptonic tau decay branching ratios and resonant structure, especially for those decay modes that include a charged kaon in the final state, as this is the main focus of this thesis.

2.1 Tau Mass

The Standard Model does not predict the quark and lepton masses. The most accurate experimental determination of the tau mass was obtained in 1995 from a data-driven scan in the immediate vicinity of the tau-pair production threshold by the Beijing Spectrometer (BES) at the Beijing Electron-Positron Collider [15].

The experiment searched for the threshold in the tau cross-section, using a technique which exploited the very low background in events from the process $e^+e^- \rightarrow \tau^+\tau^-$, where one tau decays to a muon and two neutrinos, and the other tau decays to an electron and two neutrinos. Detection of $e^+e^- \rightarrow \mu^\pm e^\mp (+ \text{missing energy})$ events during the scan indicated that the centre-

of-mass energy was above the tau-pair production threshold, whereas the lack of such events indicated that the centre-of-mass energy was below threshold. The tau mass obtained by this procedure was $m_\tau = 1776.96^{+0.31}_{-0.27}$. The previous best measurement of this quantity had an uncertainty almost an order of magnitude larger [16]. The current world average of experimental measurements of the tau mass is $m_\tau = 1777.05^{+0.29}_{-0.26}$ MeV [1].

2.2 Tau Lifetime

The lepton universality prediction for the lifetime of the tau lepton, τ_τ , is

$$\tau_\tau = \tau_\mu \left[\frac{m_\mu}{m_\tau} \right]^5 \text{Br}(\tau^- \rightarrow e^- \bar{\nu}_e \nu_\tau), \quad (2.2)$$

where

τ_μ is the lifetime of the muon. The current world average for this quantity is

$$\tau_\mu = 2.19703 \pm 0.00004 \mu\text{s}.$$

m_μ is the mass of the muon. The current world average for this quantity is

$$m_\mu = 105.658389 \pm 0.000034 \text{ MeV}.$$

$\text{Br}(\tau^- \rightarrow e^- \bar{\nu}_e \nu_\tau)$ is the branching fraction of the tau to an electron and two neutrinos. The current world average for this quantity is

$$\text{Br}(\tau^- \rightarrow e^- \bar{\nu}_e \nu_\tau) = 0.1778 \pm 0.0008.$$

All world averages are taken from the 1998 particle data summary [1]. Equation 2.2 yields the prediction $\tau_\tau = 290.6 \pm 1.1$ fs, where the dominant source of uncertainty is due to uncertainty in the electronic branching fraction of the tau.

The most precise measurements of the tau lifetime have been obtained by experiments at LEP [17] [18]. All of these measurements rely, either directly or indirectly, on the precise determination of the tau decay length, which is related to the tau lifetime. The relatively high centre-of-mass energy of the e^+e^- beams

colliding at the Z^0 resonance boosts the tau leptons produced in the $e^+e^- \rightarrow \tau^+\tau^-$ interaction such that the resulting average tau decay length in the lab frame is about 2 mm.

The world average of the experimental measurements of the tau lifetime is $\tau_\tau = 290.0 \pm 1.2$ fs [1], which is in agreement with the lepton universality prediction to within 0.4σ of the combined uncertainties. Figure 2.2 shows the world average tau lifetime versus the $\tau^- \rightarrow e^- \bar{\nu}_e \nu_\tau$ branching ratio, along with the prediction of equation 2.2.

2.3 Leptonic Tau Decays

The leptonic partial width of the tau can be analytically calculated, allowing precision tests of lepton universality and the structure of the charged weak current. Figure 2.3 shows the Feynman diagram for the leptonic decays of the tau, and the Feynman diagram for the exactly analogous decay of the muon. Under the assumption of massless neutrinos, the branching ratio of the decay of a lepton l_1 that decays into another lepton l_2 is given by [19]:

$$\text{Br}(l_1 \rightarrow l_2 \nu_{l_1} \bar{\nu}_{l_2}) = \frac{G_{l_1} G_{l_2} m_{l_1}^5 \tau_{l_1}}{192\pi^3} \left(1 - 8x_{l_2} - 12x_{l_2}^2 \log x_{l_2} + 8x_{l_2}^3 - x_{l_2}^4 \right), \quad (2.3)$$

where $x_{l_2} = m_{l_2}^2/m_{l_1}^2$, and G_l is the Fermi effective coupling strength of lepton l to the W gauge boson.

All comparisons of the experimental measurements of the $\tau^- \rightarrow e^- \bar{\nu}_e \nu_\tau$, $\tau^- \rightarrow \mu^- \bar{\nu}_\mu \nu_\tau$, and $\mu^- \rightarrow e^- \nu_\mu \bar{\nu}_e$ branching ratios to the theoretical predictions calculated from Equation 2.3 have shown that the charged weak interaction is consistent with coupling equally to all leptons [1] ($G_e = G_\mu = G_\tau$).

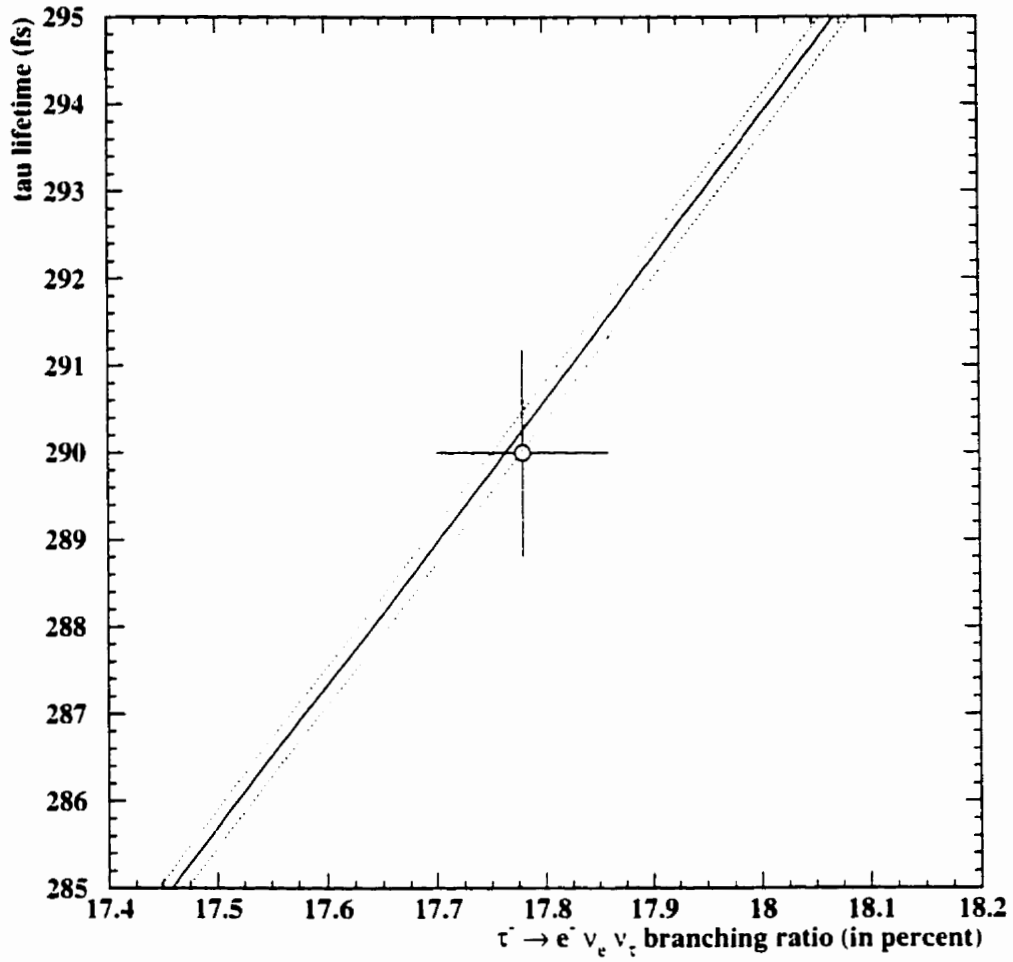


Figure 2.2: The world average tau lifetime versus the $\tau^- \rightarrow e^- \bar{\nu}_e \nu_\tau$ branching ratio. The line is the prediction under the assumption of lepton universality, and the dotted lines represent the uncertainty on this prediction due to the uncertainty in the measured tau mass.

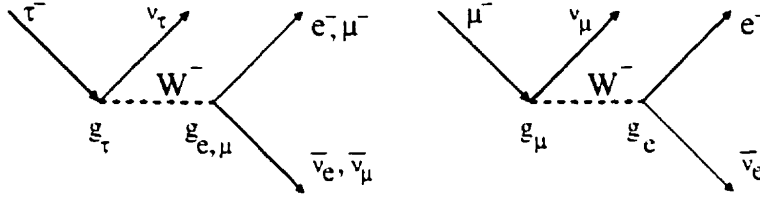


Figure 2.3: Tree-level Feynman diagrams depicting the fully-leptonic decays of the τ^- and μ^- leptons.

2.4 Semi-Leptonic Tau Decays

Figure 2.4 shows the Feynman diagram for the decay of the τ^- to a quark, an anti-quark, and a neutrino. The tau only has enough mass to decay to the three lightest quarks, therefore the final state of a τ^- decay to hadrons can only have strangeness 0 or -1 . These are referred to as Cabibbo-enhanced and Cabibbo-suppressed final states, respectively. The ratio of the tau branching fractions to Cabibbo-suppressed and Cabibbo-enhanced final states is approximately $\tan^2 \theta_C = 0.05$, where θ_C is the Cabibbo angle.

The quarks in the final state of the tau decay combine to form mesons, and this process is represented in Figure 2.4 by the hatched ellipse. Precise calculations of this process are not yet possible because the current perturbative treatment of QCD does not apply in the momentum regime of the quarks forming the final state mesons. In theoretical calculations of the tau semi-leptonic decay width, however, approximate descriptions of the decay can be achieved by the introduction of a dependence on the momentum transfer, q^2 , to the partial width of the process. This additional term is known as a spectral function, or form factor, and its functional form is derived from phenomenological models of the intermediate resonant structure of the final state hadrons.

Conservation of angular momentum requires that the ensemble of final state hadrons produced in tau decays can only have total spin $J=0$ or $J=1$, and, in

general, these final states can have either positive or negative parity¹. This limits the number of possible unique spin-parity and strangeness combinations in the final state to 8, which in turn limits the number of spectral functions we need to consider to obtain a complete description of the partial width of the tau decay to hadrons. The most general form of the partial width of the tau decay to hadrons is therefore given by [19]:

$$\begin{aligned} \Gamma(\tau^- \rightarrow \nu_\tau[\text{hadrons}]^-) = & \frac{G^2}{32\pi^2 m_\tau^3} \int_0^{m_\tau} dq^2 (m_\tau^2 - q^2)^2 \\ & \times \cos^2 \theta_C \left[(m_\tau^2 + 2q^2) (\mathbf{v}_1 + \mathbf{a}_1) + m_\tau^2 (\mathbf{v}_0 + \mathbf{a}_0) \right] \\ & \times \sin^2 \theta_C \left[(m_\tau^2 + 2q^2) (\mathbf{v}_1^s + \mathbf{a}_1^s) + m_\tau^2 (\mathbf{v}_0^s + \mathbf{a}_0^s) \right]. \end{aligned}$$

where

\mathbf{v}_1 , \mathbf{a}_1 , \mathbf{v}_0 and \mathbf{a}_0 are the spectral functions corresponding to the non-strange vector, axial-vector, scalar, and pseudo-scalar final states, respectively. All four are functions of the momentum transfer, q^2 .

\mathbf{v}_1^s , \mathbf{a}_1^s , \mathbf{v}_0^s and \mathbf{a}_0^s are the corresponding spectral functions for the strange final states. Again, all are functions of the momentum transfer, q^2 .

In tau decays to non-strange final states, where the quarks involved are very light, helicity considerations predict suppression of the scalar meson final state (ie: $\mathbf{v}_0 \sim 0$)[20], in a manner somewhat analogous to the suppression of $\pi^- \rightarrow e^- \bar{\nu}_e$ decays.² Experimental evidence supports this prediction [21]. These helicity constraints additionally imply that the non-strange axial-vector meson tau decay final

¹The intrinsic parity of a meson describes how its wavefunction transforms under a parity transformation. Axial-vector and scalar mesons have positive intrinsic parity, while vector and pseudo-scalar mesons have negative intrinsic parity.

²Since the pion has spin 0, conservation of angular momentum implies that the spin of the anti-neutrino must be opposite that of the electron. Since the anti-neutrino is necessarily right-handed, this implies that the electron, if highly relativistic, must also be right-handed. Thus, since the mass of the pion is much larger than the mass of the final state, and since the W^- preferentially couples to left-handed electrons, the decay is suppressed.

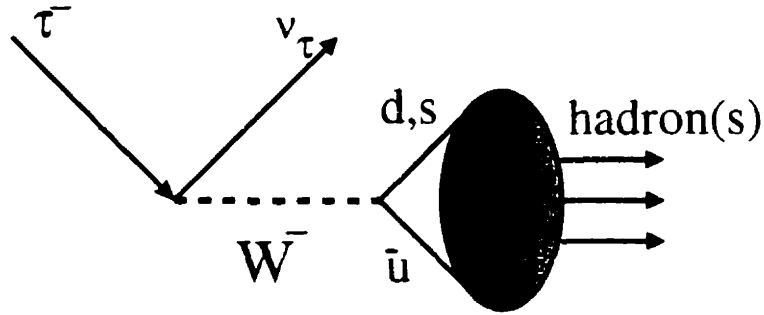


Figure 2.4: Tree-level Feynman diagram depicting semi-leptonic decays of the τ^- .

state will be completely dominated by the 3P_1 $a_1(1260)$ meson, rather than the 1P_1 $b_1(1235)$ meson. Helicity arguments in the light-quark limit also imply that tau decays to an odd/even number of pions in the final state are completely dominated by the axial-vector/vector part of the charged weak current, respectively. Thus the intermediate resonance structure of the three-pion tau decay final state, for instance, is dominated by the a_1 axial-vector meson, while the two-pion final state is dominated by the ρ vector meson [22] [23] [24]. Note that the higher mass mesons produced in tau decays, such as the ρ and a_1 , are extremely short-lived, thus their existence is only observed as a resonance in the reconstructed mass spectrum of the pions and/or kaons in the final state.

Helicity suppression is not as severe in the strange sector because the s quark is heavier than the u and d . Thus some signal from the $K^*(1430)$ scalar meson may possibly be present in tau decay final states (although this has not yet been observed) [25] [26]. In addition, both the 3P_1 and 1P_1 axial-vector K_{1A} and K_{1B} mesons are expected to be produced in tau decays, mixing to form the physically observable $K_1(1270)$ and $K_1(1400)$ axial-vector mesons [25] [28]. The degree of the mixing of these two states and the resulting relative ratios of $K_1(1270)$ and $K_1(1400)$ in tau decays is intimately related to the degree of $SU(3)$ flavour symmetry breaking introduced by the ‘heaviness’ of the s quark, and is thus of some theoretical interest [29] [30].

There are several theoretical constraints which can be used to either predict the branching ratio of the tau to particular semi-leptonic decay modes, or to inter-relate the branching ratios for various decays. A subjective list of the two most useful of these is:

Conserved Vector Current (CVC) hypothesis: the CVC theorem relates the vector part of the strangeness conserving weak current to the iso-vector part of the total cross-section for e^+e^- annihilations into hadrons [31] [32] [33]. Thus the CVC hypothesis can be used to obtain predictions for the branching ratios of tau decays dominated by the vector current, such as tau decays into final states containing an even number of pions.

Das-Mathur-Okubo (DMO) sum rules: the DMO sum rules relate, through SU(3) flavour symmetry arguments, the strangeness changing part of the weak current to the strangeness non-changing current [34]. Thus, for example, the DMO sum rules relate the $\tau^- \rightarrow \nu_\tau K^*(892)$ branching ratio to the $\tau^- \rightarrow \nu_\tau \rho(770)$ branching ratio.

Table 2.1 lists the dominant semi-leptonic tau decays, along with the current world average branching ratio measurements taken from [1]. Also shown in the table are the predicted branching ratios for these decays, some of which are derived from either the CVC theorem or the DMO sum rules. For the $\tau^- \rightarrow \nu_\tau K^-$ and $\tau^- \rightarrow \nu_\tau \pi^-$ branching ratios there are well-defined theoretical predictions (see, for instance, [19]), but for the higher multiplicity final states assumptions usually must first be made about the resonant structure of the decay. The resonant structure assumptions used in the theoretical calculation of the predicted branching ratios are also shown in Table 2.1.

2.4.1 Tau Decays to Final States with Charged Kaons

The study of tau decays to final states that include charged kaons is complicated by the relative rarity of these decays due to Cabibbo and/or phase-space suppression.

In addition, there are experimental difficulties involved in the identification of charged kaons and pions. Table 2.2 lists tau decays with a charged kaon in the final state, along with a summary of the current world averages and theoretical predictions for the branching ratios of these decays.

The tau decays of this type which have the highest branching ratios are the $\tau^- \rightarrow \nu_\tau K^-$ and $\tau^- \rightarrow \nu_\tau K^- \pi^0$ decays. Consequently, these are also the most extensively studied decays in this class. The latter decay has been found to be dominated by $K^*(892)$ production [36]. Although the heaviness of the s quark theoretically makes it possible for the $K_0^*(1430)$ scalar meson to contribute to the $\tau^- \rightarrow \nu_\tau K^- \pi^0$ channel, such an effect has not yet been observed [26]. There has perhaps been some evidence for small $K^*(1410)$ vector meson contributions to the resonant structure of this final state [27], but the difficulties involved in distinguishing between the $K^*(1410)$ and the $K_0^*(1430)$ make the results difficult to interpret.

The $\tau^- \rightarrow \nu_\tau K^- K^0$ decay is expected to occur through the high-mass tail of the $\rho(770)$ vector resonance and/or through the $\rho(1700)$ vector resonance [32], thus the theoretical prediction for the branching ratio to that final state is obtained from the CVC theorem. There has been no satisfactory experimental exploration of the resonant structure of this decay due to the difficulties involved in simultaneous charged/neutral kaon identification [36] [26].

The resonant substructure of tau decays to three-meson final states that include kaons is even more complicated. As mentioned earlier, the $\tau^- \rightarrow \nu_\tau (K\pi\pi)^-$ final state is thought to be dominated by the K_1 axial-vector resonances [37] [38]. Experimental evidence supports this prediction [40] [41]. However, unlike tau decays to three pions, which are dominated by the axial-vector current in the light-quark limit, the relative heaviness of the s quark implies that there may be some contribution of the $K^*(1410)$ vector meson to the resonant structure of these decays. However, this contribution is expected to be small [37] [38], and is difficult to distinguish from the $K_1(1400)$ intermediate state.

Again, because of the heaviness of the s quark, the $\tau^- \rightarrow \nu_\tau (K\pi K)^-$ final

state can possibly be dominated by either or both of the a_1 axial-vector or ρ vector resonances, where each resonance subsequently decays to $(K^*(892)K)^-$ [37] [38]. Distinguishing the two channels is difficult, however, and requires many more tau events than have been collected by any experiment to date.

The wide range of predicted branching ratios seen in the three-meson tau final states listed in Table 2.2 is due to various resonant substructure hypotheses used in the various models. Thus the precise experimental determination of these branching ratios may aid theorists in distinguishing between the models and therefore give some insight into the resonant structure of these decays. It has even been suggested in reference [38] that the $\tau^- \rightarrow \nu_\tau (K\pi\pi)^-$ branching ratio is sensitive to the widths of the K_1 resonances, parameters which hitherto have only been measured in the high-background environment of hadron-collision experiments [39].

The resonant substructure of the heavily phase-space suppressed tau decays to four-meson final states which include kaons is unknown due to a dearth of experimental data. As in the case of two-meson final states with kaons, the relative heaviness of the s quark implies that these states need not be dominated by the vector current, as they would be if only pions were present in the final state. Beyond this, not much more is known.

As already mentioned, an important constraint on all tau decays to kaons is the fact that the τ^- can only decay to final states of strangeness 0 or -1 . The K^- and K^+ mesons have strangeness -1 and $+1$, respectively. This implies that a decay such as $\tau^- \rightarrow \nu_\tau \pi^- \pi^- K^+$ cannot occur as a first-order weak interaction because the final state has strangeness $+1$, and is therefore highly suppressed. Table 2.3 lists strangeness suppressed decays of the tau where all the kaons in the final state are charged, along with the current experimental limits on these decays.

τ^- decay mode	measured BR (%)	dominant resonant structure	theoretical BR (%)	comments
$\tau^- \rightarrow \nu_\tau \pi^-$	11.07 ± 0.18	none	10.95 ± 0.12	<i>a</i>
$\tau^- \rightarrow \nu_\tau K^-$	0.694 ± 0.027	none	0.705 ± 0.008	<i>b</i>
$\tau^- \rightarrow \nu_\tau \pi^- \pi^0$	25.31 ± 0.18	$\rho(770)$	24.25 ± 0.77	<i>c</i>
$\tau^- \rightarrow \nu_\tau K^- \pi^0$	0.449 ± 0.034	$K^*(892)$	0.48 ± 0.02	<i>d</i>
$\tau^- \rightarrow \nu_\tau \pi^- K^0$	0.78 ± 0.06	$K^*(892)$	0.97 ± 0.04	<i>d</i>
$\tau^- \rightarrow \nu_\tau \pi^- \pi^- \pi^+$	9.57 ± 0.11	$a_1(1250)$	6.4 ± 0.8	<i>e</i>
$\tau^- \rightarrow \nu_\tau \pi^- \pi^0 \pi^0$	8.95 ± 0.33	$a_1(1250)$	6.4 ± 0.8	<i>e</i>
$\tau^- \rightarrow \nu_\tau \pi^- \pi^- \pi^+ \pi^0$	4.45 ± 0.11	unknown	4.27 ± 0.54	<i>c, f</i>
$\tau^- \rightarrow \nu_\tau \pi^- \pi^0 \pi^0 \pi^0$	1.22 ± 0.10	unknown	1.05 ± 0.10	<i>c, f</i>

^a Theoretical calculation assumes $a_0(q^2) \propto \delta(q^2 - m_\pi^2)$ [19].

^b Theoretical calculation assumes $a_0^{\text{str}}(q^2) \propto \delta(q^2 - m_K^2)$ [19].

^c Theoretical calculation uses the CVC theorem [32].

^d Theoretical calculation uses the DMO sum rules [19].

^e Theoretical calculation assumes a_1 intermediate resonant structure [35].

^f No explicit charged pion/kaon identification in the experimental measurements.

Table 2.1: Measurements and theoretical predictions for the branching ratios of the dominant tau semi-leptonic decay modes (BR > 0.5%). The experimental measurements for modes without charged kaons are world averages taken from [1]. The world averages for tau decay modes with a charged kaon in the final state are the author's own calculation based on results appearing in references [1] and [36].

τ^- decay mode	world average BR (%)	theoretical BR (%)	dominant resonant structure
$\tau^- \rightarrow \nu_\tau K^-$	0.694 ± 0.029	0.705 ± 0.008 [19]	none
$\tau^- \rightarrow \nu_\tau K^- \pi^0$	0.449 ± 0.034	0.48 ± 0.02 [19]	$K^*(892)$
$\tau^- \rightarrow \nu_\tau K^- K^0$	0.158 ± 0.019	0.111 ± 0.031 [32]	$\rho(770)$ and/or $\rho(1700)$
$\tau^- \rightarrow \nu_\tau K^- \pi^0 \pi^0$	0.058 ± 0.024	0.12 ± 0.02 [38]	$K_1(1270)$ and/or $K_1(1400)$
$\tau^- \rightarrow \nu_\tau K^- K^0 \pi^0$	0.144 ± 0.026	0.155 ± 0.005 [38]	$\rho(770)$ and/or $a_1(1250)$
$\tau^- \rightarrow \nu_\tau K^- \pi^0 \pi^0 \pi^0$	0.037 ± 0.024	-	unknown
$\tau^- \rightarrow \nu_\tau K^- K^0 \pi^0 \pi^0$	< 0.018	-	unknown
$\tau^- \rightarrow \nu_\tau K^- \pi^- \pi^+$	0.263 ± 0.037	0.18 to 0.77 [37] [38] [42]	$K_1(1270)$ and/or $K_1(1400)$
$\tau^- \rightarrow \nu_\tau K^- \pi^- \pi^+ \pi^0$	0.070 ± 0.026	-	unknown
$\tau^- \rightarrow \nu_\tau K^- \pi^- K^+$	0.156 ± 0.020	0.20 to 0.26 [37] [42]	$\rho(770)$ and/or $a_1(1250)$
$\tau^- \rightarrow \nu_\tau K^- \pi^- K^+ \pi^0$	0.043 ± 0.016	-	unknown
$\tau^- \rightarrow \nu_\tau K^- K^- K^+$	< 0.019	-	unknown

Table 2.2: Measurements and theoretical predictions for tau branching ratios to allowed exclusive final states which include at least one charged kaon. The world averages are the author's own calculation based on results appearing in references [1] [36] [41] [66]. The limits are the 95% confidence limits.

τ^- decay mode	final State strangeness	measured BR (%)
$\tau^- \rightarrow \nu_\tau \pi^- \pi^- K^- (\pi^0)$	+1	< 0.25 TPC/2 γ 94[40]
$\tau^- \rightarrow \nu_\tau K^- K^- \pi^- (\pi^0)$	-2	< 0.09 TPC/2 γ 94[40]

Table 2.3: Branching ratio measurements of tau decays with charged kaons in the final state which are forbidden due to strangeness constraints in first-order weak decays. The limits are the 95% confidence limits.

Chapter 3

LEP and the OPAL Detector

3.1 The LEP Synchrotron

The LEP (Large Electron Positron) synchrotron, located at CERN¹ near Geneva, Switzerland (see Figure 3.1), accumulates and accelerates electrons and positrons in an underground tunnel approximately 27 km in circumference. Between 1989 and 1995, during a period of operation known as LEP I, the synchrotron collided the e^+e^- beams near the Z^0 resonance at a centre-of-mass energy of roughly 91 GeV.

Electrons and positrons circulate in the LEP ring in beams consisting of several 'bunches', each containing on the order of 10^{11} particles. The two beams are brought into collision at four interaction regions around the ring at which the collaborations ALEPH, DELPHI, L3, and OPAL have detectors.

The rate, \mathcal{R} , at which physics interactions occur at each beam crossing is given by $\mathcal{R} = \mathcal{L}\sigma$, where σ is the cross-section for an e^+e^- collision to produce a given physics process, and \mathcal{L} is the luminosity of the colliding beams. The luminosity

¹European Laboratory for Particle Physics

depends on the properties of the e^+e^- beams:

$$\mathcal{L} = \frac{I_b^2 k_b}{4\pi e^2 f_0 \sigma_x^* \sigma_y^*}.$$

where

e is the electron charge.

f_0 is the orbit frequency. The value of f_0 at LEP is about 11.5 kHz.

I_b is the bunch current. The maximum value of I_b obtainable during the operation of LEP I was about 1 mA.

k_b is the number of colliding bunches.

σ_x^* and σ_y^* are the typical bunch sizes in x and y , respectively, and are given in terms of the width of the Gaussian profile of the bunch along those axes. During the operation of LEP I, typical values of these parameters were $\sigma_x^* \sim 150 \mu\text{m}$ and $\sigma_y^* \sim 12 \mu\text{m}$.

The luminosity is measured at LEP by counting the number of small-angle $e^+e^- \rightarrow e^+e^-$ events. The production of such events is dominated by Bhabha scattering, and the cross-section for this process can be reliably calculated. Between 1989 and 1991, LEP operated as it was originally designed, colliding four bunches of electrons with four bunches of positrons. Peak luminosities on the order of $11 \times 10^{30} \text{ cm}^{-2}\text{s}^{-1}$ were achieved in this 4×4 scheme [43]. To increase the luminosity further, LEP doubled the number of circulating bunches, running in a 8×8 configuration for most of the remaining period of LEP I operation. This resulted in peak luminosities of $23 \times 10^{30} \text{ cm}^{-2}\text{s}^{-1}$, exceeding the original LEP design luminosity of $16 \times 10^{30} \text{ cm}^{-2}\text{s}^{-1}$.

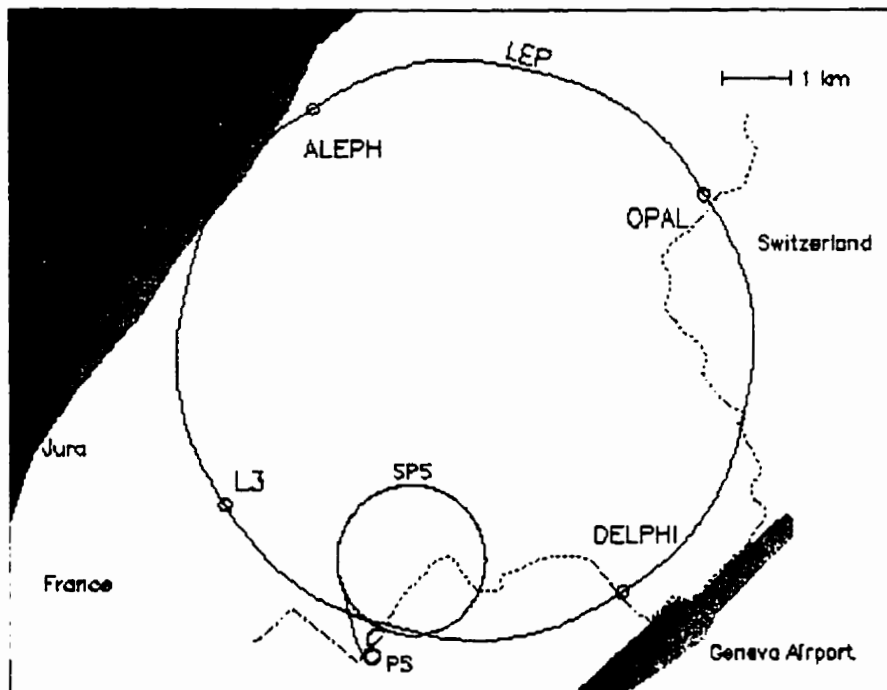


Figure 3.1: LEP and environs.

3.2 The OPAL Detector

OPAL (Omni Purpose Apparatus at LEP) is one of the four large detectors built to record the e^+e^- interactions at LEP, and it was designed in the 1980's using detector technologies conventional at the time [44]. Since the physics topics at LEP are quite varied, OPAL was designed to be a general purpose detector which would satisfy the requirements of most topics of interest.

OPAL is built around the LEP beam pipe and has the cylindrical geometry characteristic of most detectors at symmetric colliding beam experiments. The general layout of the detector is shown in Figure 3.2, which indicates the location and relative size of the various components. A right-handed coordinate system is used at OPAL, with the $+z$ -axis in the direction of the circulating electron beam, and the $+x$ -axis horizontal and pointing toward the centre of the LEP ring. The LEP ring, and thus the z -axis, is inclined at an angle of 13 mrad with respect to the horizontal. The y -axis is therefore similarly inclined with respect to the vertical. The angle θ is the polar angle with respect to the $+z$ -axis, and ϕ is the azimuthal angle with respect to the $+x$ -axis.

The OPAL subdetectors used in this analysis include:

- The tracking system, which measures the momentum, direction and ionisation energy loss of charged particles traversing the OPAL detector. Ionisation energy loss and momentum provide the only means of distinguishing charged kaons from pions in the momentum range of interest to this analysis.
- The time-of-flight system, which is used in this analysis to reject cosmic-ray backgrounds in the event samples.
- The electromagnetic calorimeter and presampler system, which is primarily used in this analysis to identify tau decays which include a π^0 in the final state.
- The hadronic calorimeter and muon chambers, which are mainly used in

this analysis to select control samples containing muons and to veto non-tau backgrounds in the event samples.

Each of these subdetectors is connected, via fast-readout, to a hardware trigger system which determines whether or not data from the event is to be recorded, based upon variables such as the event visible energy and vertex position, resulting in a data recording rate of approximately 1 to 5 Hz [45]. Once an event is flagged as potentially interesting by the trigger, the information from the sub-detectors is read out [46] and input to a filter system which acts as a second-level software trigger [47]. For events which are retained by the filter, the data is compressed and stored on disk. An online event reconstruction system then fetches this information and reconstructs quantities such as track momenta and vertex positions using the raw data from the various sub-detectors and pattern recognition algorithms [48]. These reconstructed quantities are then stored on disk or tape, ready to be analysed by members of the collaboration.

Further discussion of the OPAL detector components used in this analysis can be found in the following sections.

3.2.1 Tracking Detectors

The OPAL tracking detectors are designed to precisely determine the trajectory of charged particles traversing the detector, and also determine the ionisation energy loss, dE/dx , of these particles. There are three multi-wire drift chamber components to the central detector, all of which are contained within a pressure bell filled with a mixture of 88.2% argon, 9.8% methane, and 2.0% isobutane at a pressure of 4 atmospheres. The pressure bell is contained in a solenoidal magnetic field of 0.435 T, directed along the $+z$ -axis. The three tracking components are the vertex detector ($r < 25$ cm), the jet chamber ($25 < r < 185$ cm), and the z -chambers ($r = 185$ cm). A brief summary of the properties and spatial resolution of the tracking detectors is shown in Table 3.1. Detailed descriptions of each the tracking detectors are given below.

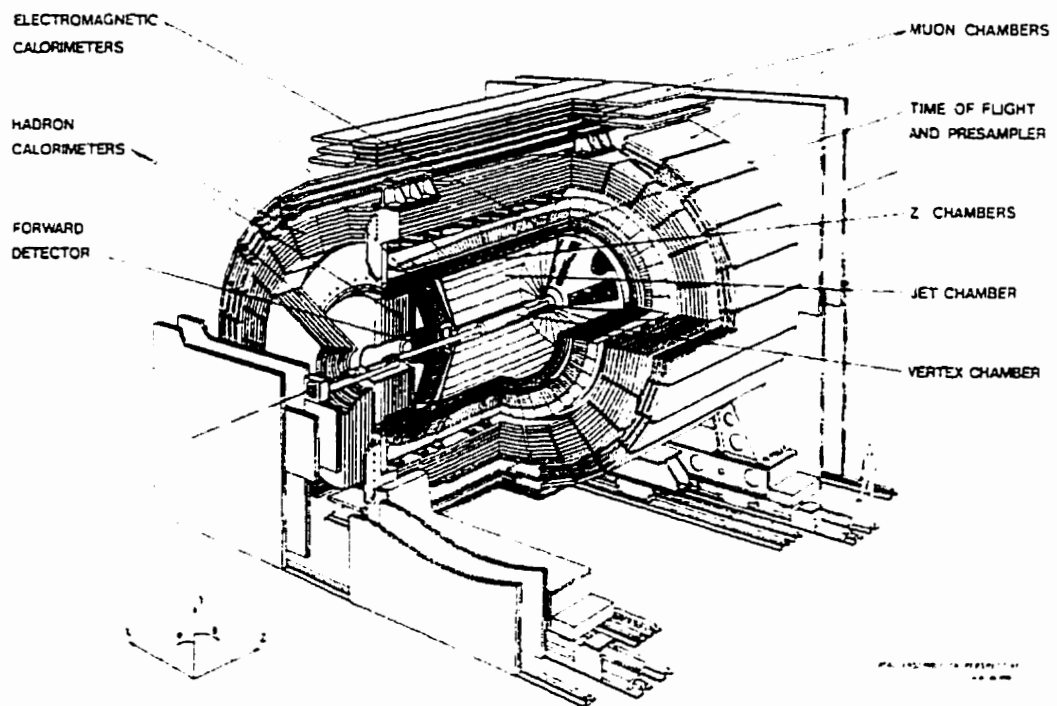


Figure 3.2: The OPAL detector.

	Vertex Detector	Jet Chamber	z-Chambers
Wire Organization	36 axial sectors (12 wires per axial sector), 36 stereo sectors (6 wires per stereo sector)	24 sectors 159 wires per sector	24 chambers 8 cells per chamber 6 wires per cell
Wire spacing Wire stagger	5.3 mm (axial), 5.0 mm(stereo) $\pm 40 \mu\text{m}$	10.0 mm $\pm 100 \mu\text{m}$	4.0mm $\pm 250 \mu\text{m}$
Maximum drift distance Maximum drift time	1.4 cm 0.5 μs	25 cm 5 μs	25 cm 5 μs
Gas	argon (88.2%), methane (9.8%), and isobutane(2.0%) at 4 bar		
Gas gain	2×10^4	10^4	$2 - 5 \times 10^4$
Angular coverage	$ \cos\theta < 0.92$ axial+stereo $ \cos\theta < 0.95$ axial	$ \cos\theta < 0.73$ 159 wires $ \cos\theta < 0.98 \geq 8$ wires	$ \cos\theta < 0.72$ and 94% in ϕ
ϕ determination ϕ resolution	drift time 50 μm .to 90 μm	drift time 135 μm	charge division 15 mm
z determination z resolution	ΔT and stereo 4 cm (ΔT), 700 μm (stereo)	charge division 6 cm	drift time 100 μm to 135 μm
Two-bit resolution	2.0 mm	2.5 mm	2.5 mm

Table 3.1: Some properties of the OPAL gaseous tracking chambers.

The Vertex Detector

The vertex detector is the drift chamber tracking component closest to the beam pipe, and, as its name implies, it precisely measures the position of the tracks of charged particles close to the e^+e^- interaction point and therefore aids in determination of event vertex positions.

In addition to this detector, a two-layer silicon micro-vertex detector was installed around the OPAL beam pipe in 1991. This detector provides high precision measurements of track trajectories close to the interaction point. Originally it only provided $r - \phi$ information, but was upgraded in 1993 to also measure the z -coordinate of hits and to extend the solid angle coverage.

The silicon micro-vertex detector greatly aids the study of short-lived particles such as B and D mesons, and also benefits the determination of the lifetime of the tau lepton.

The Jet Chamber

The primary purpose of the OPAL jet chamber is to sample, at regular intervals, the $r - \phi$ position of the path of a charged particle traversing the detector so that the 'track' of the particle can then be reconstructed from these measured space points. The transverse momentum of the particle is deduced from the curvature of the track in the magnetic field provided by the solenoid. The jet chamber is also designed to aid in charged particle identification through the precise determination of the energy loss of charged particles as they ionise the gas in the central detector.

The wires of the central jet chamber are approximately 4 m long and are organized in a jet-cell geometry, seen in Figure 3.3, where cathode wire planes divide the detector into 24 identical azimuthal sectors, each of which contains 159 sense wires to detect the ionisation produced by the passage of charged particles. All wires lie parallel to the beam direction and the anode wires are slightly staggered along the anode plane to resolve left/right ambiguities of particle trajectories.

The voltages of the wires within the central jet chamber are arranged to provide

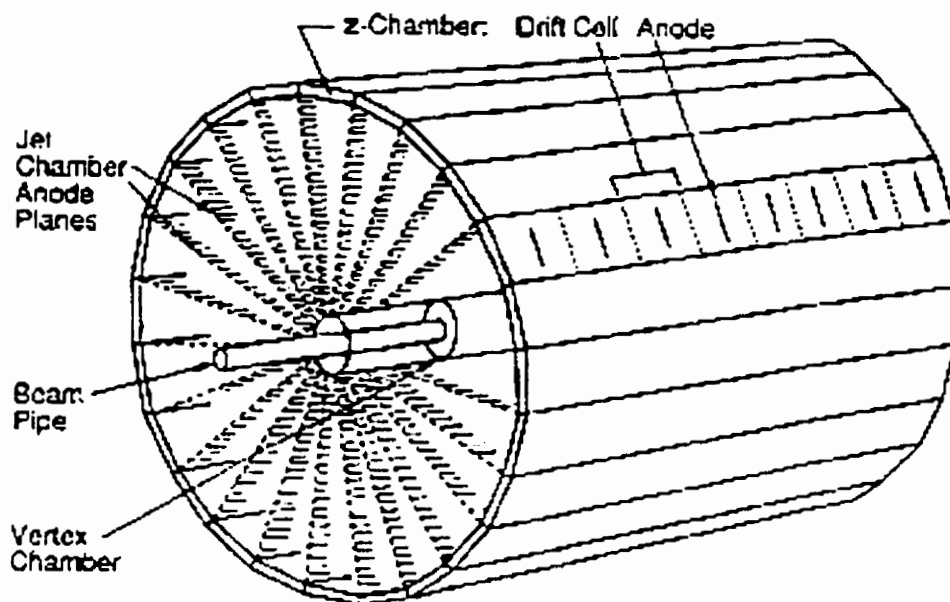


Figure 3.3: Schematic of the OPAL jet chamber and z -chambers.

a nearly constant electric field of about 1 kV/cm over the volume of the chamber.

As a charged particle traverses the gas inside the chamber, it ionises the gas, and the electrons from this primary ionisation begin to drift towards high-field amplification region close to the anode wires. Typical drift distances in the jet chamber are 10 cm and the drift times are on the order of $2 \mu\text{s}$. As the electrons approach the high field region near the anode, they accelerate rapidly, and begin to cause secondary ionisation of the gas. These secondary electrons then cause tertiary ionisation, and so on, thus producing an ionisation avalanche. The gas gain of the chamber is approximately 10^4 electrons reaching the anode wires per initial electron/ion pair.

The electrons produced by the passage of the charged particle initially accelerate in the electric field of the chamber, but very quickly reach a constant velocity known as the drift velocity. Thus the r -coordinates along the track are determined by the radial positions of the wires in the chamber sensing the electrons from the

ionisation, and the ϕ -coordinate is determined from the time it takes the electrons from the ionised gas to drift to the sense-wires. The spatial resolution in the $r - \phi$ plane of the jet chamber is $\sigma_{r-\phi} = 135 \mu\text{m}$, which leads to a transverse momentum resolution of

$$\frac{\sigma_p}{p} = \sqrt{(0.028)^2 + (0.0015p)^2},$$

where p is in units of GeV/c. The constant term inside the square root is due to multiple scattering of the charged particle as it traverses the gas in the chamber, and the second term is due to single hit resolutions.

The number of electron/ion pairs created by the charged particle as it traverses the chamber is directly proportional to the energy lost by the particle. Thus the integrated charge collected at the anodes is a measure of the ionisation energy loss of the particle. A particle traversing the jet chamber yields $N_{dE/dx}$ independent energy loss measurements (where $N_{dE/dx}$ can be as high as 159) which are approximately Landau distributed, as seen in Figure 3.4. The broad central peak in this distribution is due to soft collisions of the charged particle with the detector gas material. The long tail at high dE/dx is due to harder collisions, which can ‘knock-off’ electrons from the gas molecules to form δ rays, a process which involves a large energy transfer. It is the average energy lost by the particle to soft collisions that yields useful charged particle identification information, rather than the hard-collision energy loss.

Thus, to estimate the average energy loss in a way which minimises the impact of the hard-collision dE/dx tails, a truncated mean procedure is used. The highest 30% of the $N_{dE/dx}$ energy loss measurements for the track are rejected, and the mean of the distribution of the remaining dE/dx measurements is used to estimate the energy loss of the particle. The resulting dE/dx resolution as a function of $N_{dE/dx}$ is shown in Figure 3.5.

Various factors can cause non-uniform dE/dx response of the jet chamber. The most important of these is the degradation of the dE/dx resolution in a dense

simulated OPAL $e^+e^- \rightarrow \mu^+\mu^-$ data

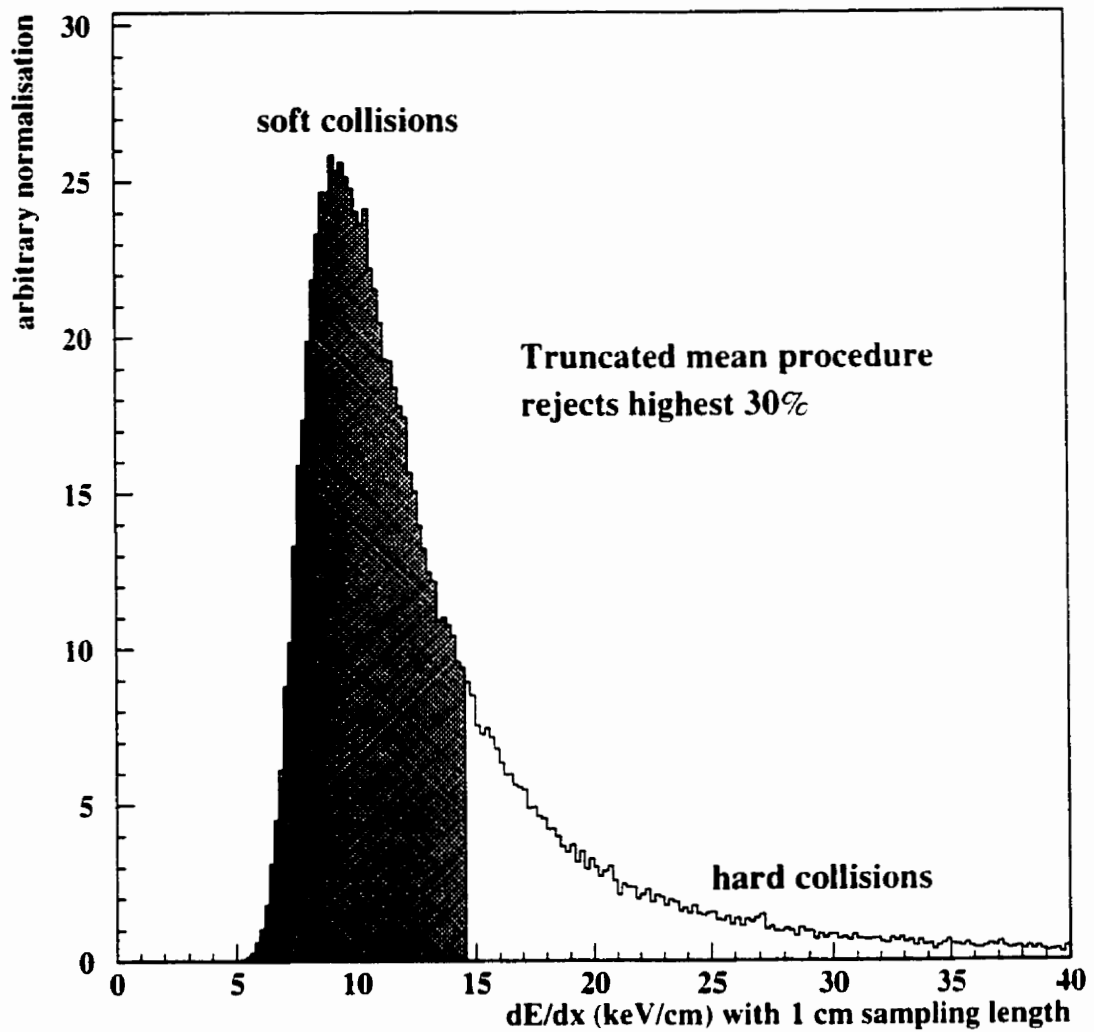


Figure 3.4: Typical distribution of the sampled energy loss in the OPAL jet chamber.

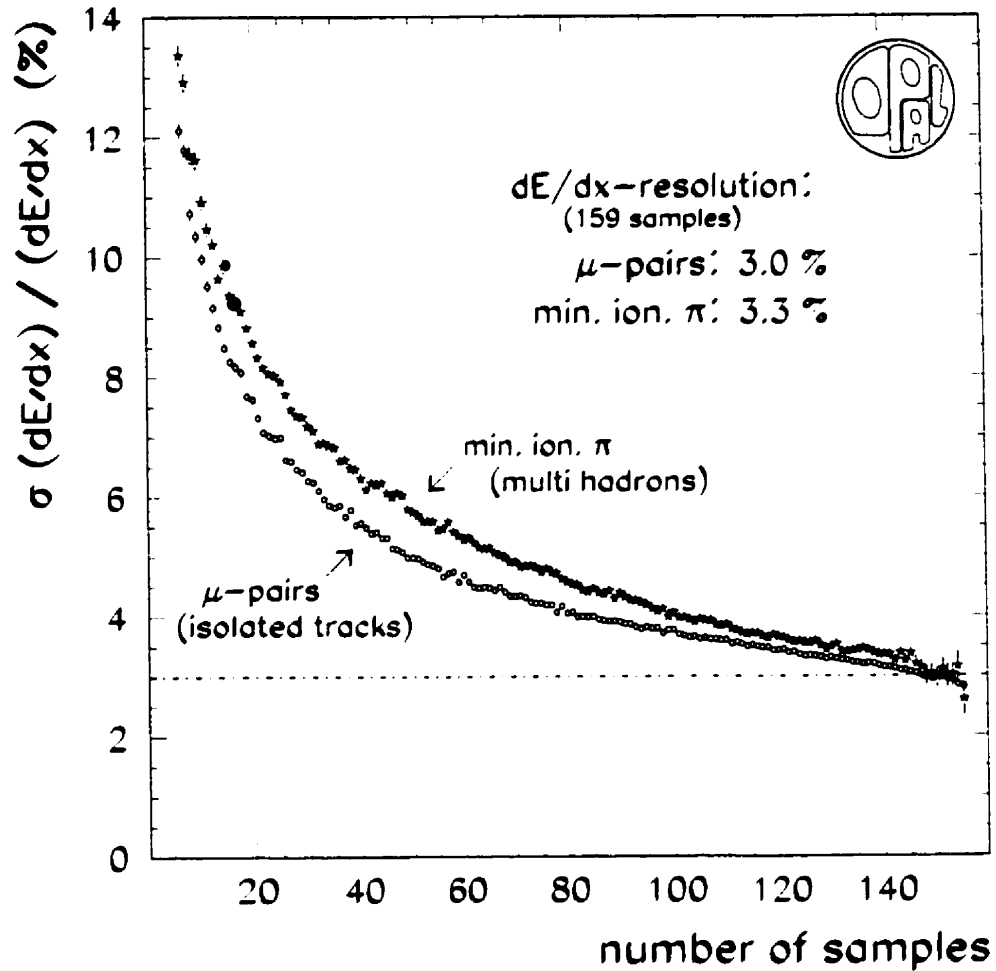


Figure 3.5: Resolution of the ionisation energy loss as a function of the number of samples, $N_{dE/dx}$, for tracks in the OPAL jet chamber.

track environment, such as hadronic Z^0 events, as is shown in Figure 3.5, which compares the dE/dx resolution of isolated tracks to that of tracks in hadronic Z^0 events. Figure 3.6 (a) shows the typical jet chamber wire response within a dense track environment. The sense wires of the jet chamber are read out with a sampling time of 10 ns, which corresponds to one bin in the plot. The integrated charge for the track collected by a particular sense wire is calculated by integrating the wire signal over a nominal period of 200 ns (20 bins), or until another leading edge of a pulse is detected, whichever comes first. In a dense track environment, the pulses overlap, making the determination of the total integrated charge for each pulse more difficult. Figures 3.6 (b) and (c) show an example of two overlapping jet chamber pulse signals. The integration length for the first pulse is from its leading edge, to the leading edge of the second pulse. In this case, this is shorter than the nominal integration length of 200 ns. Thus, to determine the total charge, the extrapolated charge from the first pulse lying under the second is determined using an ‘average’ pulse shape, and this is added to the charge from the original integration. In a similar fashion, the charge of the second pulse is integrated over 200 ns, and the extrapolated charge from the first pulse is subtracted. Since the ‘average’ pulse shape may differ from the actual pulse shape, this procedure results in somewhat worse dE/dx resolution than direct integration in a single-track environment, and can even result in a mis-assessment of the measured dE/dx if the actual pulse shape happens to be quite different than the ‘average’ shape. In addition, the effectiveness of this procedure is also limited by the detector efficiency for double hit recognition.

Other factors can result in non-uniform jet chamber dE/dx response. The most important of these are, roughly ordered from largest effect to least (shifts are relative to the absolute dE/dx):

Charge saturation: Figure 3.7 shows two tracks within the OPAL jet chamber, at large and small θ , respectively. The ionisation from the track at large θ has a large space charge density, which effectively screens the ionisation cloud

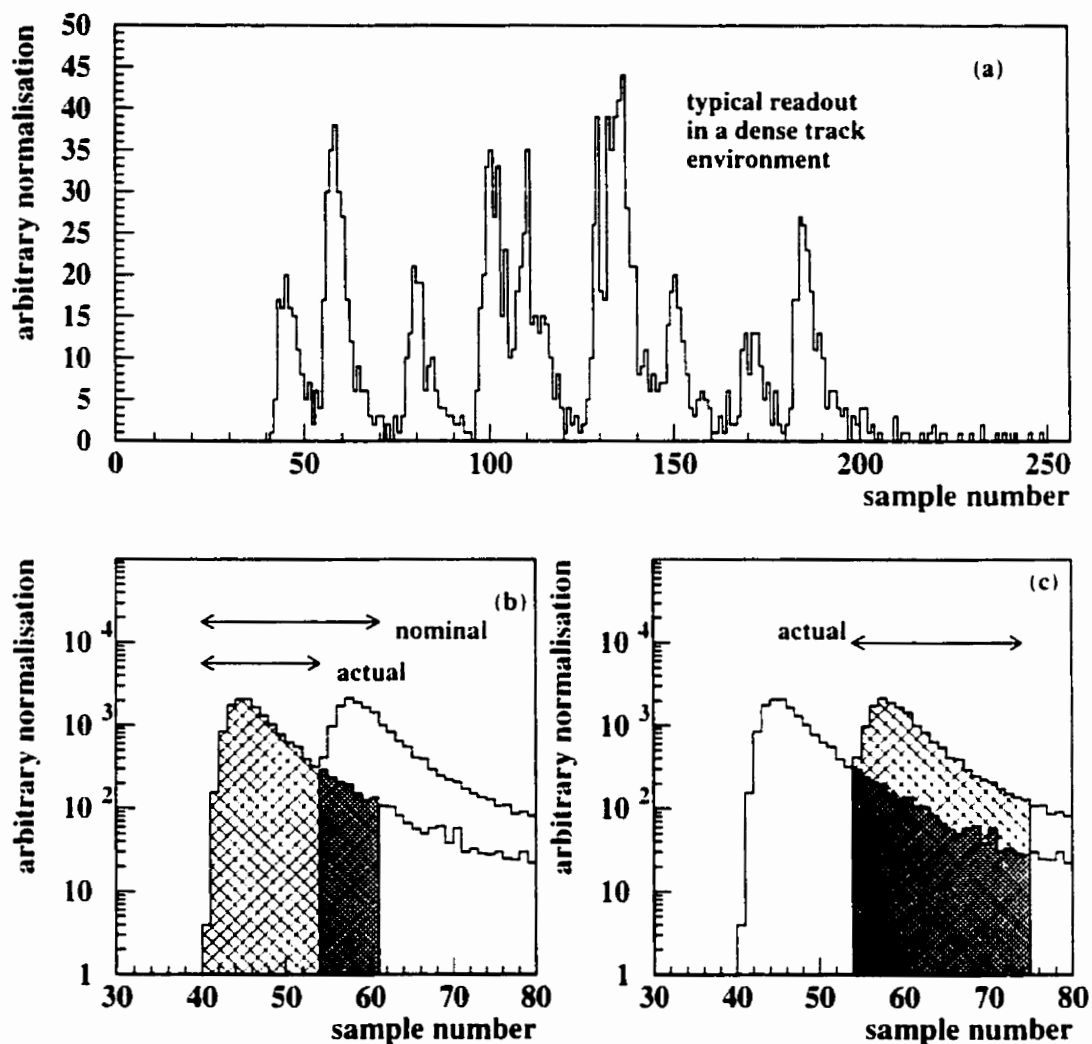


Figure 3.6: (a) shows the typical jet chamber wire response within a dense track environment. (b) shows an example of two overlapping pulses. The integrated charge from the first pulse is determined from the actual integrated charge, plus the extrapolated charge lying underneath the following pulse. (c) again shows an example of two overlapping pulses. The integrated charge from the second pulse is determined from the actual integrated charge, minus the extrapolated charge from the preceding pulse.

of electrons from the electric field of the jet chamber. Thus the gas gain of the chamber is reduced for such a track. The ionisation from the track at small θ has a low space charge density, and does not suffer from this effect. Charge saturation effects cause dE/dx shifts of between 6% to 12%.

Gas density: Time-dependent changes in the gas density within the jet chamber affect the dE/dx response. In general, higher gas density corresponds to smaller measured energy loss, and vice versa. Gas density variations cause up to 10% shifts in the dE/dx .

Electric field variation: The electric field within the jet chamber is nearly constant over almost the entire volume of the chamber. However, close to the entrance and exit to the chamber in r , there is non-uniformity in the field which causes variations in the measured dE/dx on the order of 10%.

Cross talk: The pulses from the sense wires are corrupted with induced crosstalk signals from neighbouring wires. A hardware crosstalk compensation network compensates for first and second neighbour crosstalk. The remaining crosstalk results in dE/dx shifts on the order of about 6%.

All of these effects are corrected offline such that the overall systematic variation in the measured dE/dx is less than the statistical uncertainty obtained from the truncated mean procedure. The overall combined uncertainty in dE/dx is approximately 3% of the mean dE/dx . The parameterisation of dE/dx after the application of the offline corrections is described in detail in Chapter 4.

The z -Chambers

The optimal spatial resolution of the central jet chamber is achieved in the $r - \phi$ plane, but some z -position information for the track is obtained from the division of charge read out from each end of the anode wires, with a resolution of about 6 cm. To improve this measurement, information is used from a layer of wire

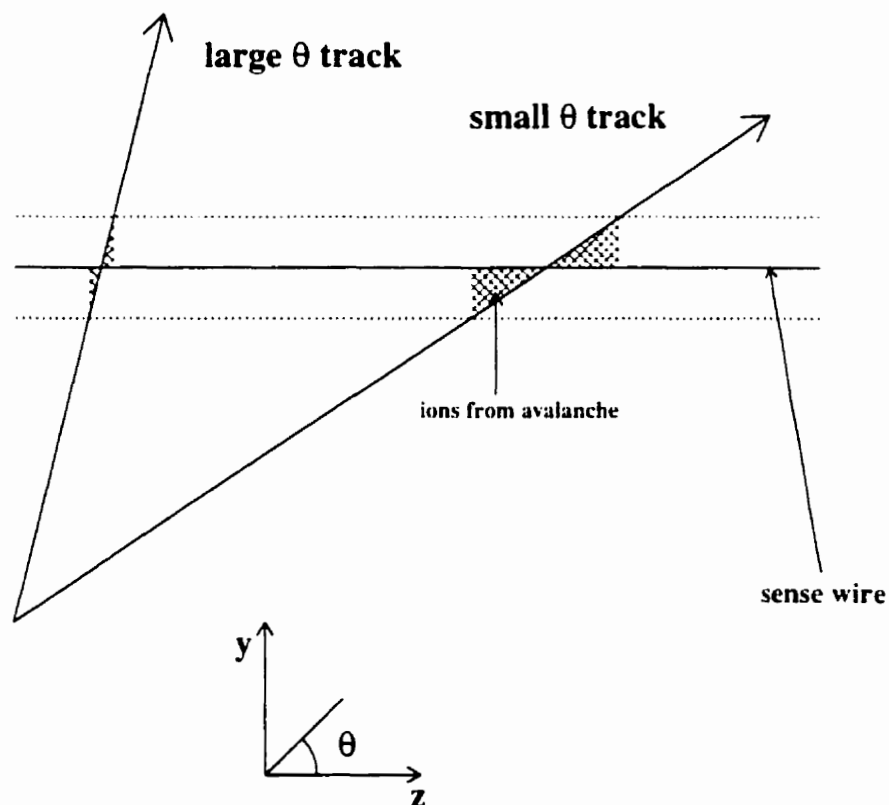


Figure 3.7: Schematic (not to scale) showing two tracks in the $z - y$ plane of the OPAL jet chamber. The space charge density of the ion avalanche cloud from the large θ track is quite high as it moves towards the sense wire, thus screening the charge in the cloud from the electric field of the chamber. This effectively reduces the gas gain of the chamber for such tracks. Ion clouds from tracks at small θ have a much smaller space charge density, and thus do not suffer as much from this effect.

chambers immediately outside the jet chamber, with drift direction parallel to the z -axis. These z -chambers consist of 24 modules in ϕ which can provide up to 6 measurements of the z -coordinate of the track. The information from the z -chambers improves the z -coordinate resolution of tracks in the central detector to $\sigma_z = 100 - 135 \mu\text{m}$.

The z -chambers cover the region $|\cos\theta| < 0.73$. For tracks with polar angles outside this region, some improvements in the measurement of θ can be obtained using the radius of the last wire hit in the jet chamber as the track exits the central tracking detector. This extra information is used to constrain the regular track fitting procedure, resulting in higher precision in the polar angle measurement of the track.

3.2.2 Time-of-Flight

The OPAL time-of-flight system consists of 160 bars of scintillator attached to photomultiplier tubes via light guides at each end. These are located in the barrel region just outside the solenoid coil and measure the times of arrival of charged particles with an accuracy of about 250 ps. Although this is not useful for measuring the velocity of particles with momentum greater than a few GeV, the system does provide useful trigger information. The time-of-flight system is primarily used in this analysis to veto cosmic ray backgrounds from the pre-selected tau decay candidate sample.

3.2.3 The Electromagnetic Calorimeter

The OPAL electromagnetic calorimeter is mounted between the solenoid coil and the magnet return yoke, and is designed to measure the energies and angular positions of electrons, positrons, and photons through the measurement of the amount of Cherenkov light produced in lead glass blocks by the electromagnetic showers of these particles.

	Barrel σ_E/E	Endcap σ_E/E
Intrinsic	$0.002 \oplus 0.063/\sqrt{E}$	$0.05/\sqrt{E}$
Measured	$0.015 \oplus 0.16/\sqrt{E}$	$0.018 \oplus 0.22/\sqrt{E}$
Corrected	$0.022 \oplus 0.13/\sqrt{E}$	-

Table 3.2: Intrinsic and measured energy resolutions of the OPAL barrel and endcap electromagnetic calorimeter, where E is measured in GeV. The corrected resolution for the barrel calorimeter is obtained using information from the pre-sampler chambers.

The barrel portion of the calorimeter is constructed of lead glass blocks fitted with photomultiplier tubes. Each block is approximately $10\text{ cm} \times 10\text{ cm}$ in the transverse plane, and is more than 20 radiation lengths in depth, which is sufficient to fully contain the electromagnetic showers typically encountered in tau decays. There are also two additional lead glass assemblies mounted on the endcap resulting in a total angular coverage of 98% of 4π .

The segmentation of the 11000 lead glass blocks used in the calorimeter could, in principle, allow the positions of electromagnetic showers to be measured to within about 11 mm. However, this resolution is significantly degraded by the presence of two radiation lengths of material in front of the calorimeter due to the presence of the central tracking pressure vessel and the solenoidal coil.

The resolution is improved in the barrel calorimeter by the addition of multi-wire pre-sampling chambers immediately in front of the calorimeter. These chambers allow the positions of showers entering the calorimeter to be determined with an accuracy of about 5 mm. The energy resolution of the barrel and endcap electromagnetic calorimeters is shown in Table 3.2.

3.2.4 The Hadronic Calorimeter

The iron return yoke of the OPAL solenoid is instrumented with streamer tubes to form the barrel hadronic calorimeter ($|\cos\theta| < 0.81$). Additional hadronic

calorimeters are located in the endcap ($0.81 < |\cos\theta| < 0.91$) and poletip regions ($0.91 < |\cos\theta| < 0.99$). The energy resolution of the calorimeter is about $\sigma_E/E = 120\%/\sqrt{E}$, where E is measured in GeV.

3.2.5 The Muon Chambers

The OPAL detector is surrounded by several layers of wire chambers designed to identify the position of charged particles leaving the hadron calorimeter. Since hadrons and electrons are likely to be absorbed by the OPAL calorimeters, the charged particles exiting the detector are predominantly muons. Hence these detectors are referred to as the muon chambers.

The coverage of the muon chambers extends to $|\cos\theta| < 0.98$. However, there are gaps in the acceptance caused by the presence of the OPAL beam pipe, detector support legs, and cables. The resulting reduced coverage is about 93% of the full solid angle.

Chapter 4

Calibration of Ionisation Energy Loss

As detailed in the description of the OPAL jet chamber in the previous chapter, a particle of charge q and speed β traversing a medium, such as a gas, ionises that medium and loses a small amount of energy in the process. The mean energy loss per unit distance due to this ionisation is approximately described by the Bethe-Bloch equation [49]:

$$dE/dx = -\frac{A_1 q^2}{\beta^2} \left[A_2 + \ln(\gamma^2 \beta^2) - \beta^2 - \delta(\beta)/2 \right]. \quad (4.1)$$

where A_1 and A_2 are constants that depend on the gas composition used in the OPAL jet chamber, and $\delta(\beta)$ is a function that describes effects due to polarisation of the gas.

The Bethe-Bloch ionisation energy loss parameterisation used by OPAL, D_{pred} , uses four parameters (A_1 , A_2 , and two parameters used by the function δ), plus two extra parameters used to scale the momentum and β . The uncertainty on D_{pred} is given by:

$$\sigma = \sqrt{T_1^2 + T_2^2 + T_3^2}$$

$$= \sim 3\% D_{\text{pred}}. \quad (4.2)$$

where

$$\begin{aligned} T_1 &= A \cdot (N_{dE/dx}/159)^b \cdot F_{\text{path}}(\theta) \cdot G_{\text{dens}} \cdot D_{\text{pred}} \\ T_2 &= H_{\text{path}}(\theta) \cdot D_{\text{pred}} \\ T_3 &= \Delta p \frac{\partial D_{\text{pred}}}{\partial p}. \end{aligned}$$

and where:

$N_{dE/dx}$ is the number of hits in the jet chamber used in the calculation of the measured dE/dx [50].

A and b are constants which depend on the geometry and gas composition of the OPAL jet chamber.

$F_{\text{path}}(\theta)$ is a path length correction.

$H_{\text{path}}(\theta)$ is an additional path length correction.

G_{dens} is a correction dependent on the track density in the event.

Δp is the uncertainty on the momentum measurement for the track.

Along with the six parameters used in the OPAL parameterisation, the quantities A and b are obtained from a fit to the measured energy loss of charged particles in hadronic Z^0 decays, yielding a dE/dx parameterisation, D_{pred} , that is accurate enough for nearly all analyses of OPAL data.

Figure 4.1(a) shows the dependence of dE/dx on the momentum of various particles in the OPAL jet chamber, as predicted by D_{pred} . Figure 4.1(b) shows the particle resolving power, \mathcal{R}_{ij} , versus momentum for various pairs of particle species i and j , where

$$\mathcal{R}_{ij} \equiv |D_{\text{pred}}^i - D_{\text{pred}}^j| / \sigma.$$

and where σ is the mean of the uncertainties of D'_{pred} and D'_{pred} . Note that the OPAL jet chamber yields a pion/kaon separation of at least 2σ for particles between about 2 and 30 GeV/c.

Figure 4.2 shows dE/dx resolution for various present-day detectors, taken from reference [51]. The dE/dx resolution of the OPAL detector is among the best yet achieved by any experiment.

4.1 dE/dx in the Tau Decay Environment

As mentioned above, the OPAL dE/dx parameterisation is tuned to the measured energy loss of charged particles in hadronic Z^0 decays. Tau decays, however, are characterised by lower multiplicity and narrower jets than those produced in hadronic Z^0 decays. This results in small systematic differences between the measured dE/dx in these two environments that must be corrected for accurate particle identification in the tau decay environment. In this analysis, three corrections are applied to the measured energy loss, D_{meas} , and to the OPAL dE/dx parameterisation and its uncertainty, D_{pred} and σ . For clarity of presentation, one-prong control samples are used to demonstrate the need for the corrections, but similar behaviour is also observed in the energy loss of three-prong tau decay samples. The three corrections are:

Multiplicative correction to D_{pred} : Figure 4.3 shows $D_{\text{meas}}/D_{\text{pred}}$ versus

$Q(\mathcal{J}) = -\log(1 - \mathcal{J}^2)$ for tracks in the $e^+e^- \rightarrow e^+e^-\mu^+\mu^-$ ($Q < 6$) and $\tau^- \rightarrow \mu^- \bar{\nu}_\mu \nu_\tau$ ($Q > 6$) candidate samples. If D_{pred} optimally describes the measured dE/dx of tracks in these low-multiplicity samples, this distribution would be consistent with a flat line centered at one. The structure seen in this plot, however, indicates that D_{pred} requires correction with a multiplicative factor $s(\mathcal{J})$. For this analysis, parameterising $s(\mathcal{J})$ as a second order polynomial in Q yields satisfactory results. Figure 4.4 shows the momentum versus Q for kaons, pions, and muons.

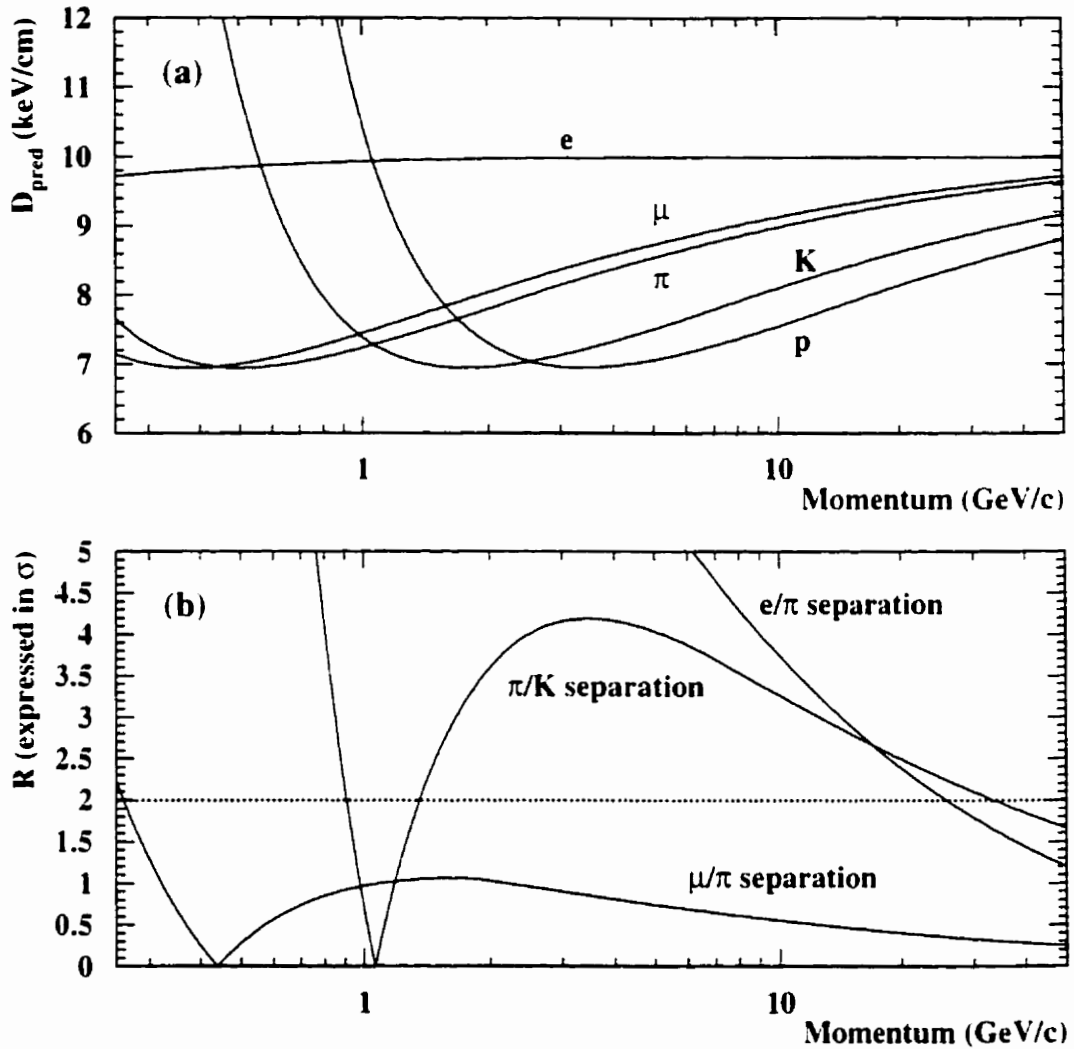


Figure 4.1: (a) shows the ionisation energy loss D_{pred} as a function of the momentum for various particles in the OPAL jet chamber. (b) shows the resolution power \mathcal{R}_{ij} expressed in terms of the dE/dx resolution σ , for various pairs of particle species i and j .

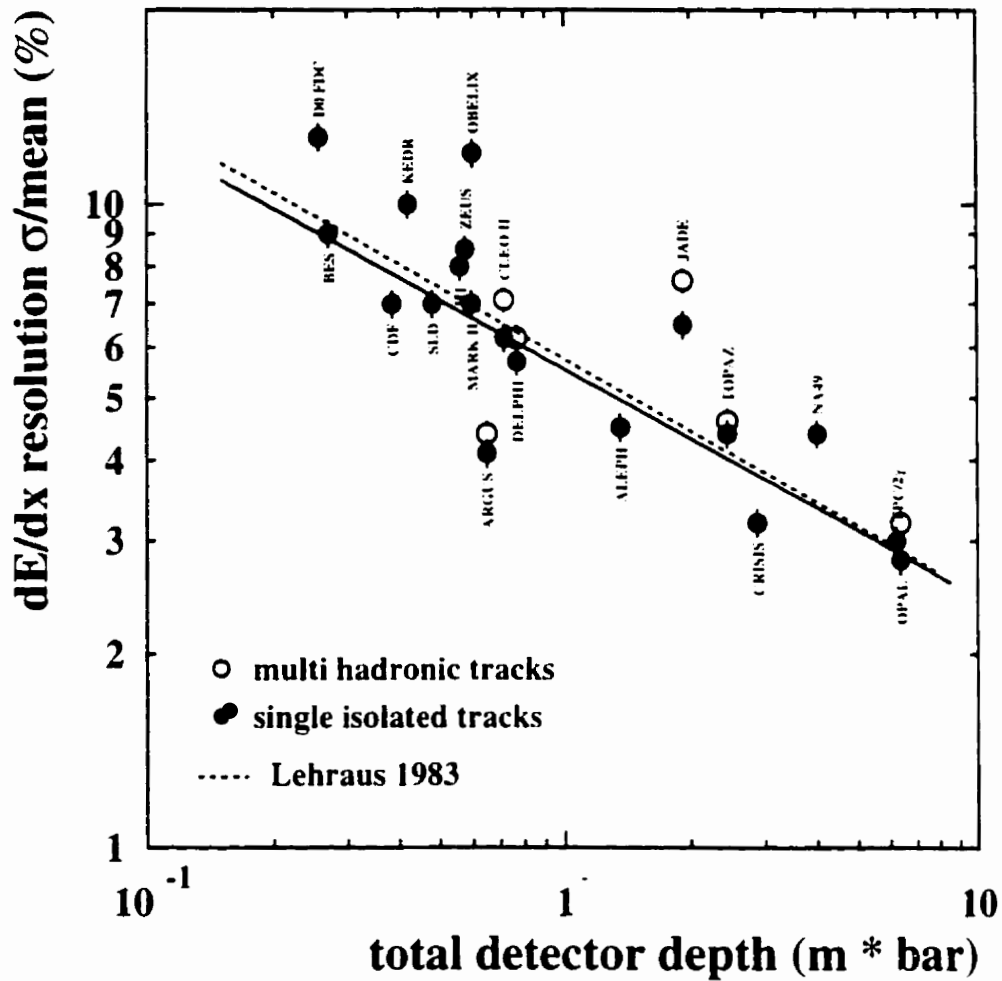


Figure 4.2: dE/dx resolution versus detector depth $L = N_{\text{samples}} \times l_{\text{samples}} \times \text{pressure}$ for various detectors, including OPAL. Full circles represent the resolution for isolated tracks, while the open circles represent the dE/dx resolution from tracks in hadronic Z^0 decays, where available. The solid and dotted lines represent fits to the dE/dx resolution versus L for isolated tracks [51].

Multiplicative correction to σ : Figure 4.5 shows the stretch dE/dx under a muon hypothesis, S_μ , for tracks in the $\tau^- \rightarrow \mu^- \bar{\nu}_\mu \nu_\tau$ candidate sample. The stretch dE/dx is defined as

$$S_i = (D_{\text{meas}} - D_{\text{pred}}^i) / \sigma_i,$$

where i is the particle hypothesis used to calculate D_{pred} and σ . For a pure sample of particles such as this, the stretch dE/dx in Figure 4.5 should be distributed as a unit Gaussian; the non-unit width of this distribution indicates that a multiplicative factor s_{res} is needed to correct σ . The non-zero mean of this distribution is corrected by the factor $s(\beta)$, discussed above.

Additive correction to D_{meas} : Figure 4.6 shows D_{meas} versus local ϕ (the track position within a jet chamber cell) for tracks in the $e^+e^- \rightarrow \mu^+\mu^-$ candidate sample. The strong dependence of D_{meas} on local ϕ is similar for all low-multiplicity samples, and requires correction to improve the dE/dx resolution in low-multiplicity events.

The corrections to the OPAL parameterisation are obtained as follows:

1. The local ϕ dependent corrections to the measured dE/dx , $f(\phi)$, are obtained directly from a χ^2 fit to the measured dE/dx of the $e^+e^- \rightarrow \mu^+\mu^-$ candidate sample.
2. The resolution correction, s_{res} , is obtained from a fit to the measured energy loss of tracks the $\tau^- \rightarrow \mu^- \bar{\nu}_\mu \nu_\tau$ sample.
3. The three parameters of the β dependent correction to D_{pred} , $s(\beta)$, are obtained in a fit to the energy loss of the data $\tau^- \rightarrow \mu^- \bar{\nu}_\mu \nu_\tau$ sample and muons from the two-photon process $e^+e^- \rightarrow e^+e^-\mu^+\mu^-$. These provide a fairly pure sample of muons over a wide range of Q (3.75 to 13.0).
4. Steps 2 and 3 are then repeated twice more, although convergence of s_{res} is obtained after only one extra iteration.

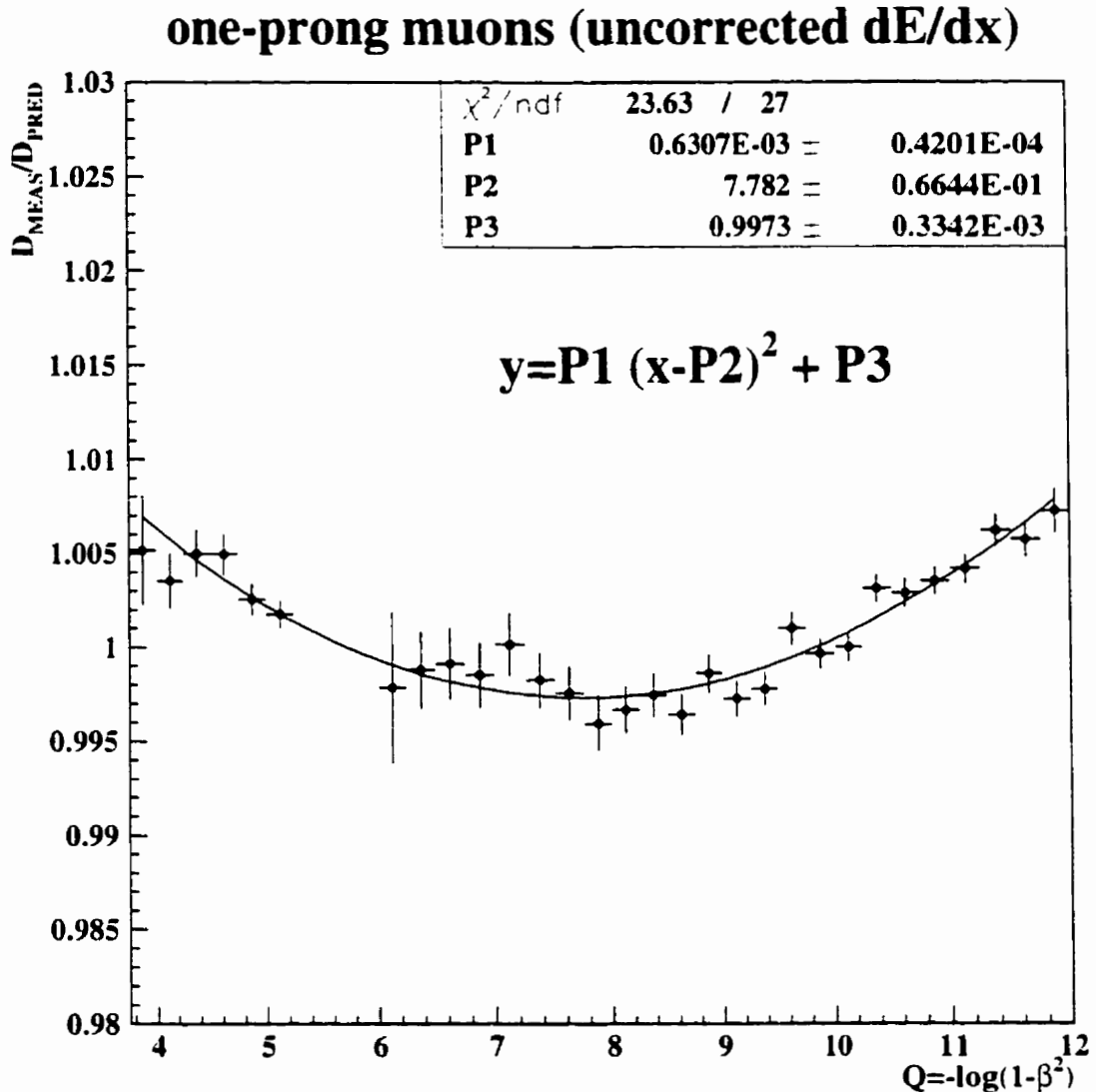


Figure 4.3: $D_{\text{meas}}/D_{\text{pred}}$ versus $Q = -\log(1 - \beta^2)$ for tracks in the $e^+e^- \rightarrow e^+e^-\mu^+\mu^-$ ($Q < 6$) and $\tau^- \rightarrow \mu^-\bar{\nu}_\mu \nu_\tau$ ($Q > 6$) candidate samples. D_{pred} is the uncorrected OPAL dE/dx parameterisation. The structure in this distribution indicates that D_{pred} does not optimally describe the measured dE/dx of these low-multiplicity samples. A multiplicative factor $s(\beta)$ is used to correct D_{pred} to resolve this discrepancy. For this analysis, $s(\beta)$ is parameterised as a second order polynomial in Q .

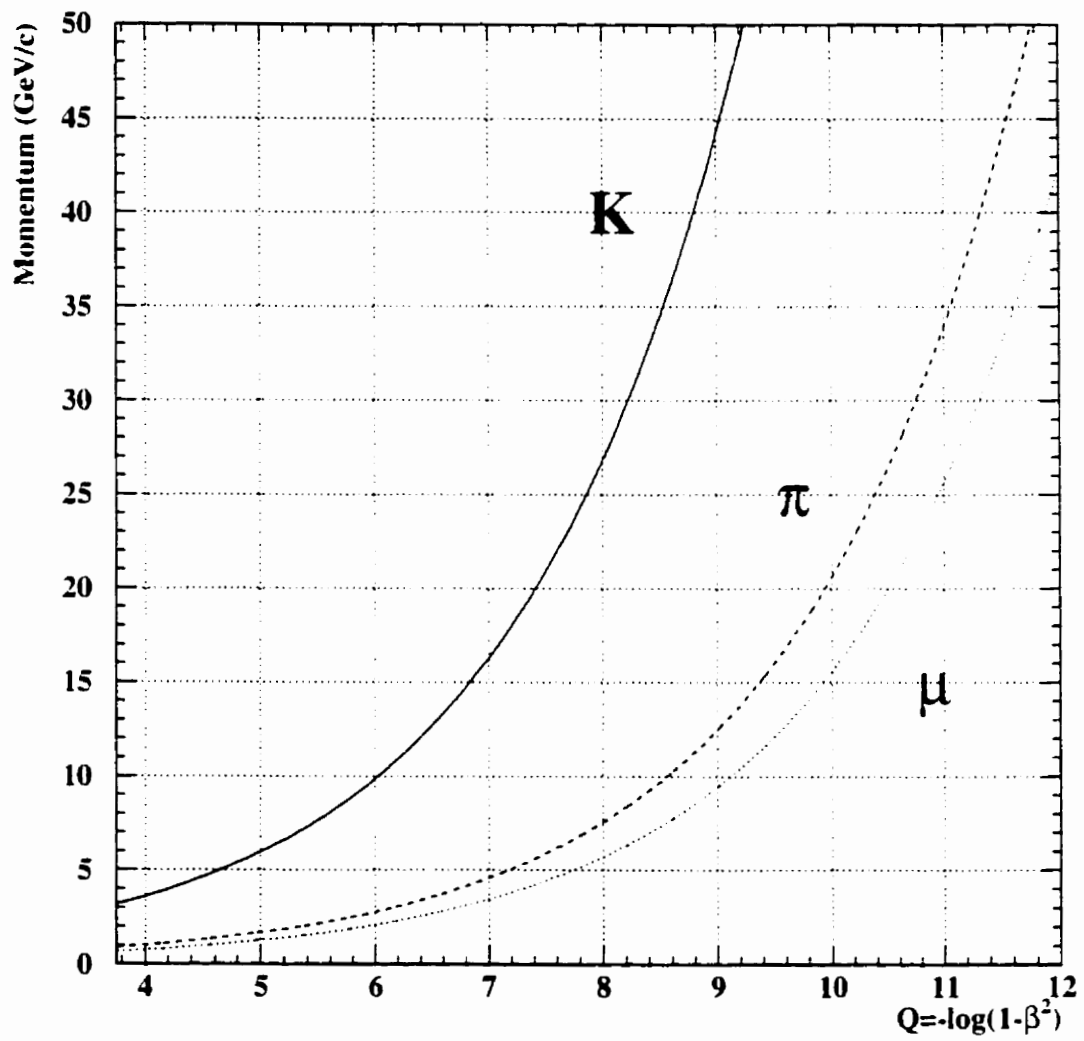


Figure 4.4: Momentum versus $Q = -\log(1 - \beta^2)$ for various particle species.

$\tau^- \rightarrow \mu^- \nu \nu$ sample (uncorrected dE/dx)

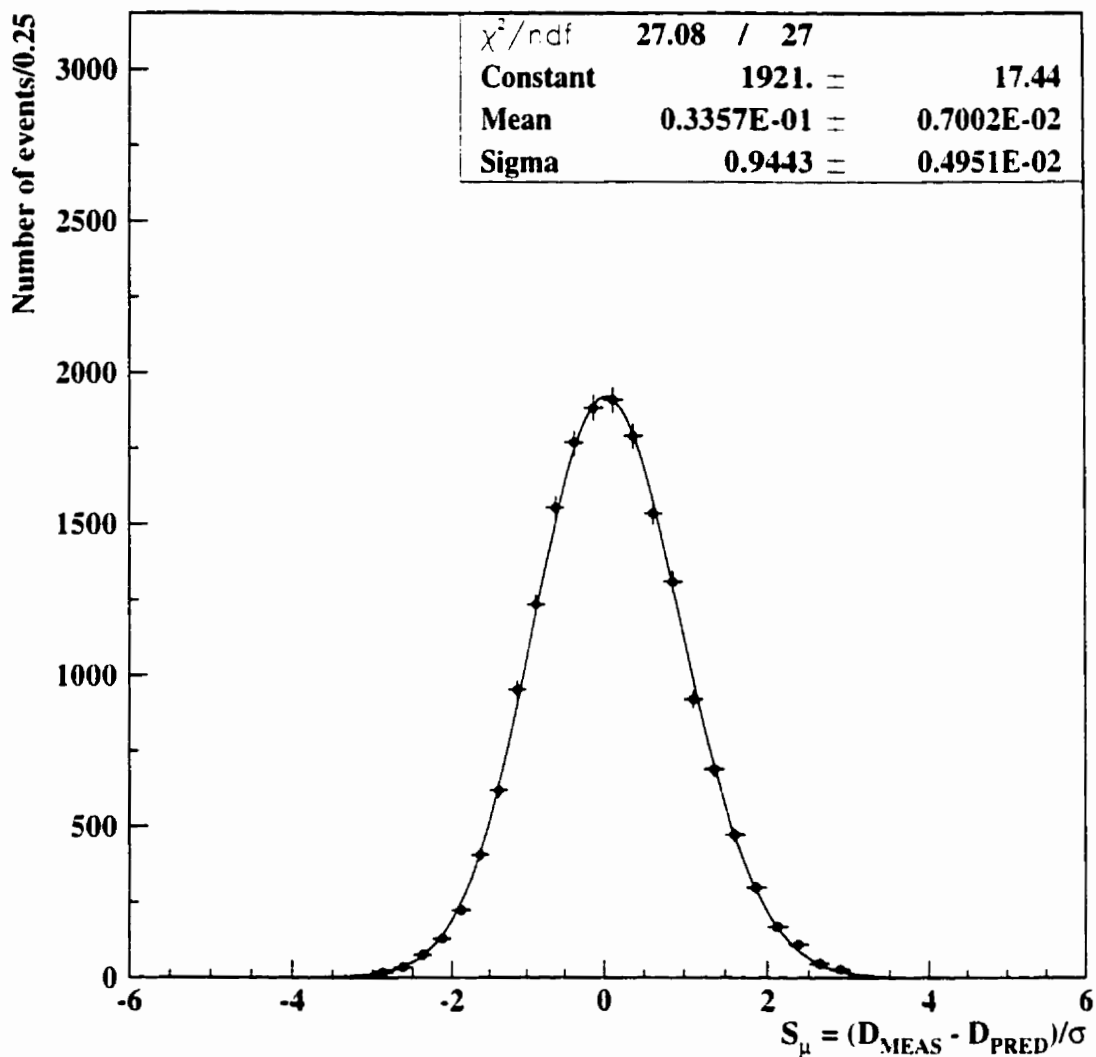


Figure 4.5: Stretch dE/dx under the muon hypothesis $S_\mu = (D_{\text{meas}} - D_{\text{pred}}^\mu)/\sigma_\mu$ of tracks in the $\tau^- \rightarrow \mu^- \bar{\nu}_\mu \nu_\tau$ candidate sample. The predicted dE/dx and σ are calculated using the uncorrected OPAL parameterisation. For a pure sample of particles such as this one, the stretch dE/dx should be distributed as a unit-Gaussian. The non-unit width of this distribution is corrected with a multiplicative factor s_{res} to σ . The non-zero mean is corrected with a multiplicative factor $s(\beta)$ to D_{pred} .

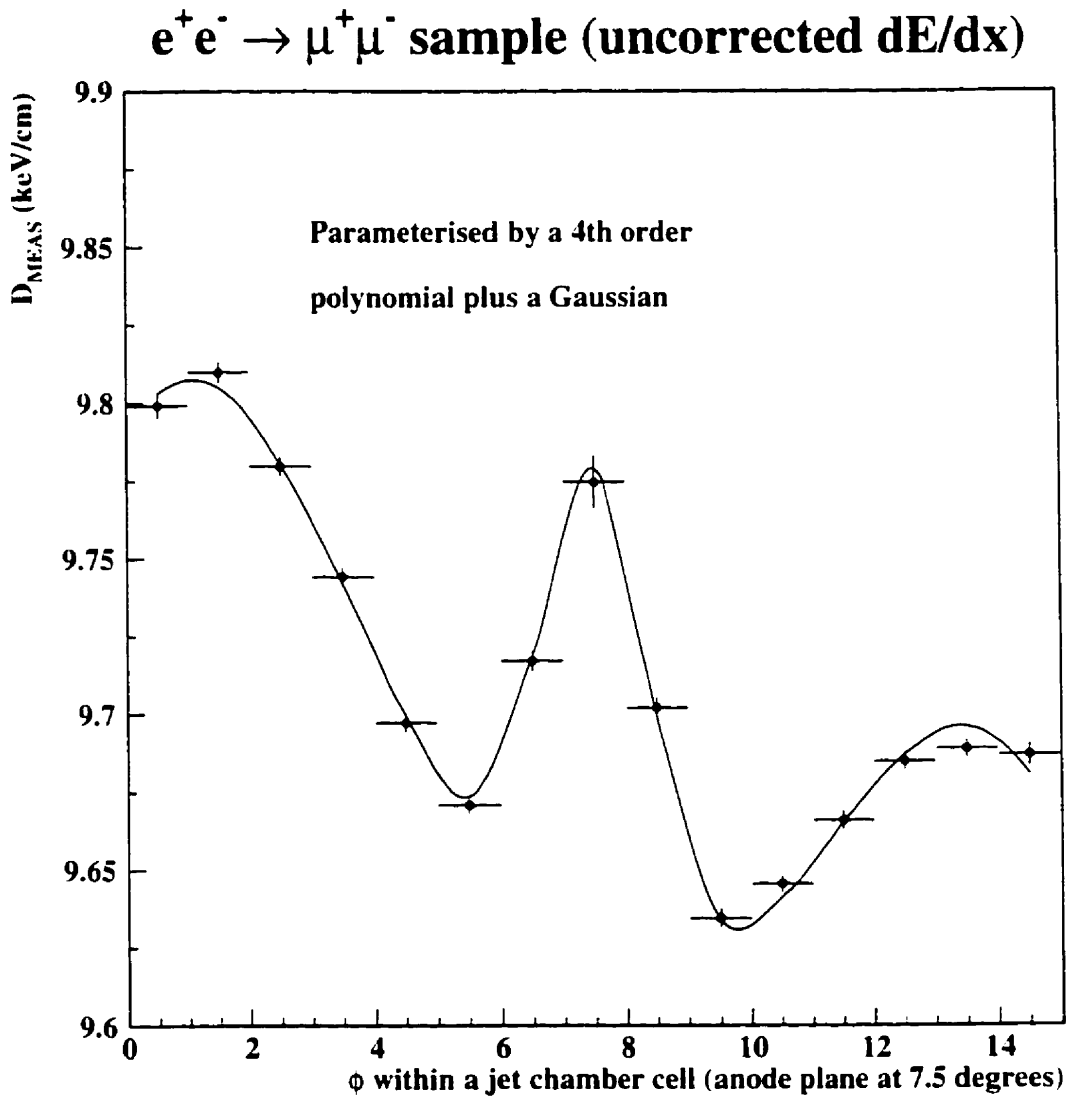


Figure 4.6: D_{meas} versus local ϕ (track position within a jet chamber cell) of tracks in the $e^+e^- \rightarrow \mu^+\mu^-$ candidate sample. The strong dependence of D_{meas} on local ϕ is similar in other low-multiplicity samples, and requires an additive correction of $f(\phi)$ to D_{meas} .

Figures 4.7 (a) and (b) show the S_π distribution of tracks in one-prong tau decays before and after corrections to D_{pred} , D_{meas} , and σ , respectively. The description of the dE/dx of this sample is significantly improved after the application of the dE/dx corrections.

4.1.1 dE/dx in the Three-Prong Tau Decay Environment

Although the application of the above corrections significantly improves the parameterisation of dE/dx in the three-prong tau decay environment, the energy loss distribution of tracks in three-prong tau decays, unlike the dE/dx distribution of tracks in one-prong tau decays, contains a significant non-Gaussian component. This feature is most apparent in the corrected dE/dx stretch distribution of the unlike-sign tracks of tau decays classified as $\tau^- \rightarrow \nu_\tau \pi^- \pi^- X^-(\pi^0)$ ¹. The $\tau^- \rightarrow \nu_\tau \pi^- \pi^- X^-(\pi^0)$ control sample is selected using the requirement that both like-sign tracks have $S_K > 2.0$ to identify three-prong tau events with two like-sign pion candidates in the final state. Since the $\tau^- \rightarrow \nu_\tau \pi^- \pi^- K^-(\pi^0)$ final states are highly suppressed, the unlike-sign tracks in this sample are expected to be over 99.7% pure in pions. The stretch dE/dx distribution under a pion hypothesis of this sample is seen in Figure 4.8(a).

The non-Gaussian component is large in the region of the dE/dx distribution expected to be populated by kaons. Parameterisation of the non-Gaussian component would therefore lead to very large statistical and systematic uncertainties in the measurement of the $\tau^- \rightarrow \nu_\tau K^- \pi^- \pi^+(\pi^0)$ and $\tau^- \rightarrow \nu_\tau K^- \pi^- K^+(\pi^0)$ branching ratios. The tail is dramatically reduced in the dE/dx distribution of tracks in three-prong tau decays that lie closest to the anode plane, as shown in Figure 4.8(b). When tracks are spatially close together in the jet chamber cell, the tail of the pulse from the track closest to the anode can shift the pedestal of the pulse of the second track, leading to an incorrect determination of deposited

¹The unlike-sign track is the track in the three-prong decay with charge opposite that of the initial tau.

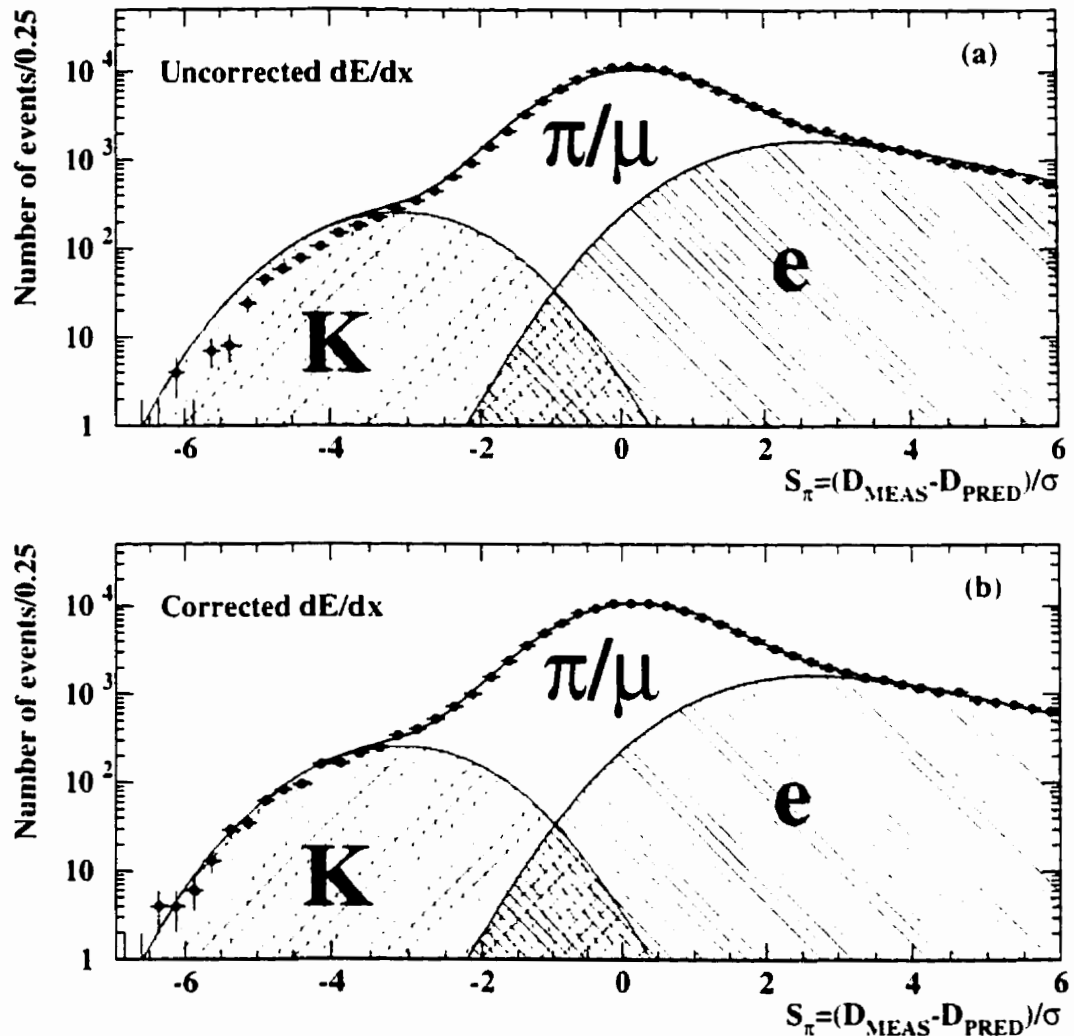


Figure 4.7: (a) shows S_π of tracks in data one-prong tau decays (points) before the application of corrections to D_{pred} , D_{meas} , and σ . The components of the predicted distribution are normalised using world average branching ratios taken from [1]. The χ^2 per degree of freedom between the data and predicted distributions is 1006/47. (b) shows S_π of the same sample after the application of corrections to D_{pred} , D_{meas} , and σ . The χ^2 per degree of freedom between the data and predicted distributions is 52/47.

charge for that track, and the observed tails in the dE/dx distribution. The low-end non-Gaussian tail exists in the measured energy loss of charged particles in hadronic Z^0 events, but is more pronounced in three-prong tau decays due to the tighter collimation of the particles in the decay.

The simplest method to minimize this effect is to only consider the dE/dx of the track in the three-prong tau decay closest to the anode plane. Tracks meeting this requirement will be referred to as the ‘first-track’ three-prong sample. Further, the effect of pulses following the first is reduced by only considering first pulses separated from the second by more than 1 cm [50].

The corrected stretch dE/dx distribution of unlike-sign tracks in the first-track $\tau^- \rightarrow \nu_\tau \pi^- \pi^- X^-$ sample, seen in Figure 4.8(b), is consistent with a Gaussian of zero mean and unit width.

Figures 4.9 (a) and (b) show the S_π distribution of first-tracks in the three-prong tau decays before and after corrections to D_{pred} , D_{meas} , and σ , respectively.

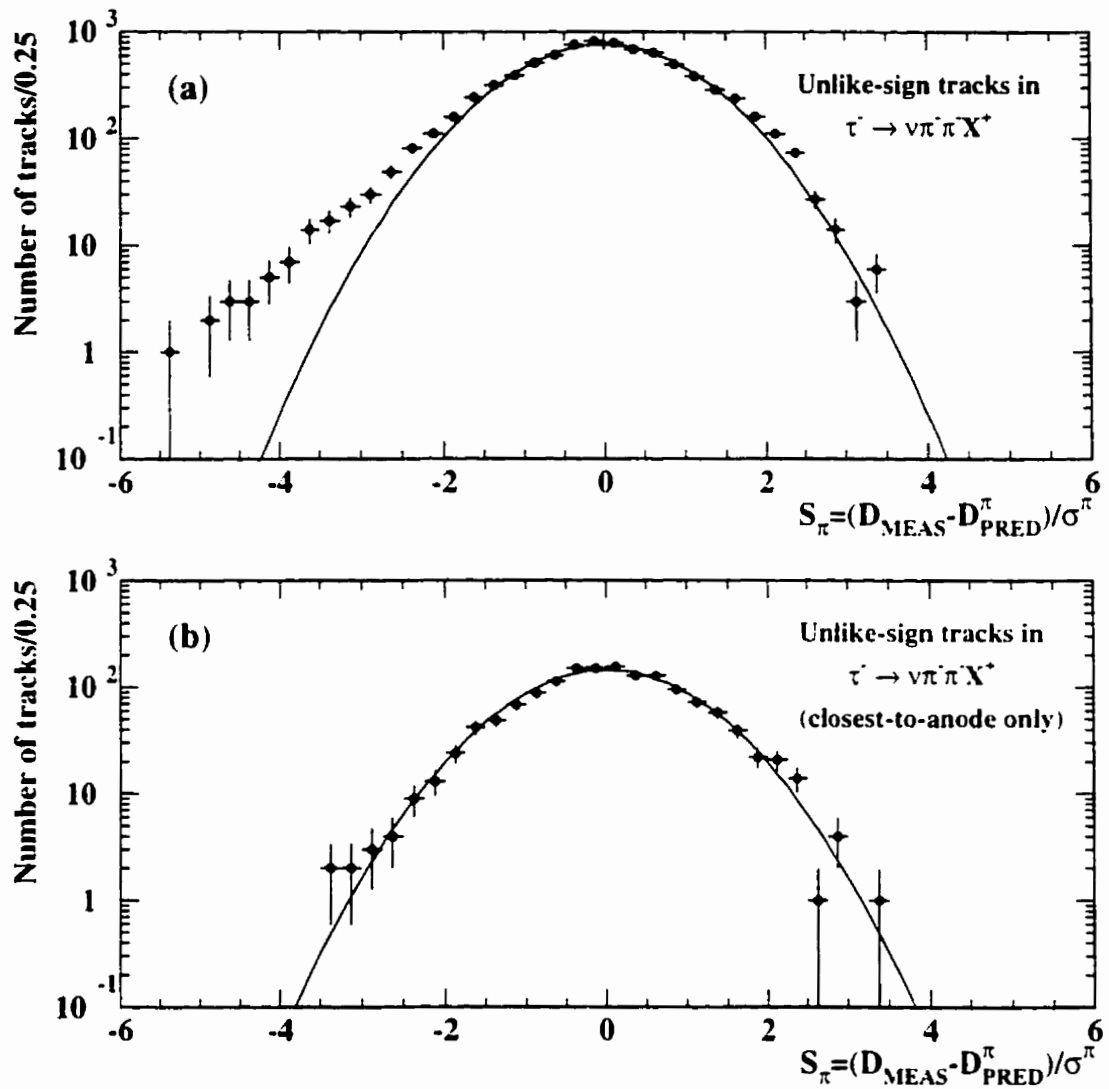


Figure 4.8: (a) is the stretch dE/dx distribution under the pion hypothesis for the unlike-sign tracks in the data $\tau^- \rightarrow \nu_\tau \pi^- \pi^- X^+ (\pi^0)$ candidate sample (points). This sample is expected to have less than three kaons present. The curve is a unit width Gaussian of zero mean, whose normalisation is fit to the central part of the distribution. A significant non-Gaussian component is evident. (b) is the same distribution for the unlike-sign tracks in the data first-track $\tau^- \rightarrow \nu_\tau \pi^- \pi^- X^+ (\pi^0)$ candidate sample. The χ^2 per degree of freedom between the data and the Gaussian is 13/18.

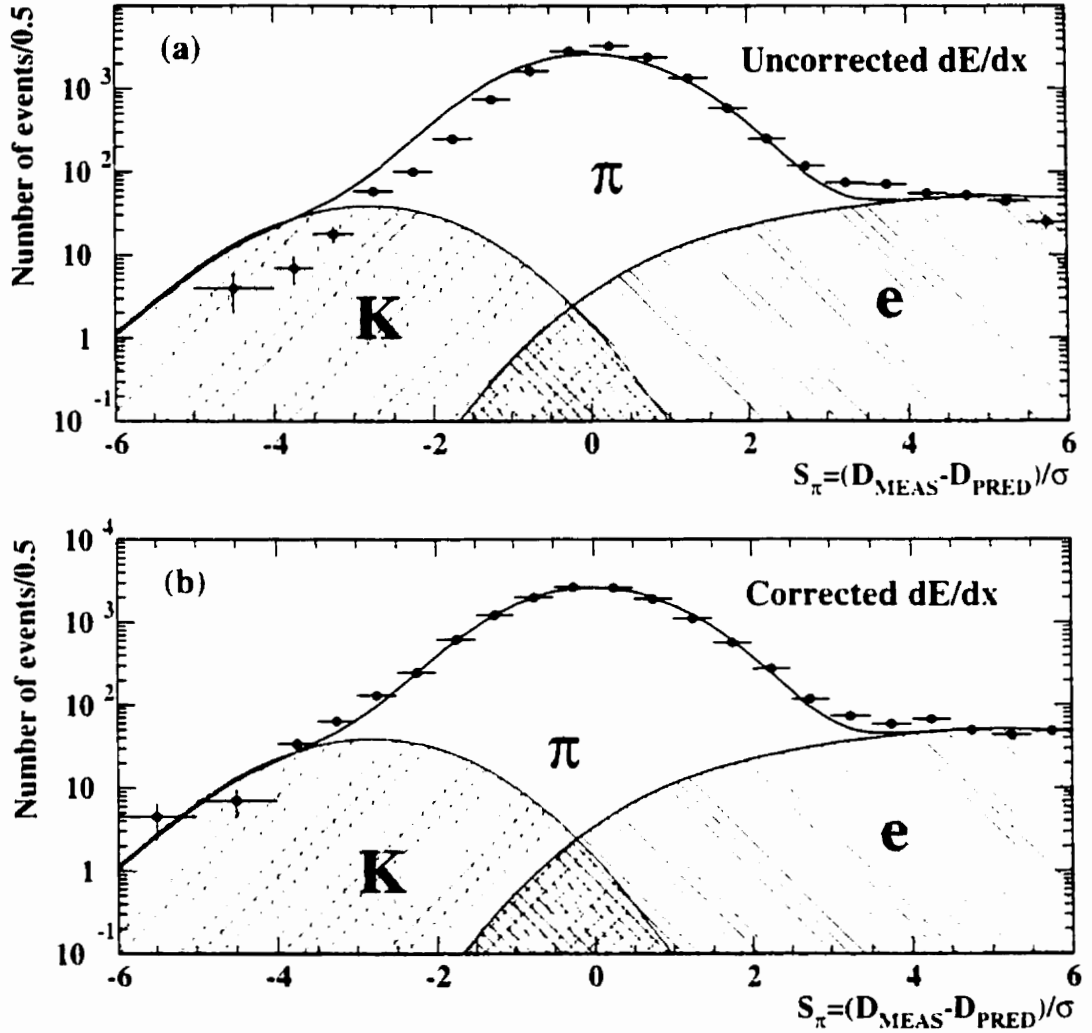


Figure 4.9: (a) shows S_π of data first-tracks in three-prong tau decays (points) before the application of corrections to D_{pred} , D_{meas} , and σ . The components of the predicted distribution are normalised using world average branching ratios taken from [1]. The χ^2 per degree of freedom between the data and predicted distributions is 1547/20. (b) shows S_π for the same sample after the application of corrections to D_{pred} , D_{meas} , and σ . The χ^2 per degree of freedom between the data and predicted distributions is 67/21.

Chapter 5

The OPAL Data Sample

This analysis uses the full data set collected by the OPAL detector between the years 1990 and 1995 at e^+e^- centre-of-mass energies close to the Z^0 resonance. Table 5.1 shows the year-by-year integrated luminosity delivered by LEP during this period. Only data for which the tracking chambers and the electromagnetic calorimeter were fully operational are retained.

5.1 The Tau-Pair Sample

The topology of $e^+e^- \rightarrow \tau^+\tau^-$ events is characterised by a pair of back-to-back, narrow jets with low particle multiplicity (Figures 5.1 and 5.2 show typical $\tau^+\tau^-$ events in the OPAL detector). Jets are defined in this analysis by grouping tracks and electromagnetic clusters into cones of 35° half opening angle, where each cone is assumed to contain the decay products of one of the tau leptons. Tau pair candidates are selected by requiring two low multiplicity jets. Background events from other lepton pairs, hadronic Z^0 events, and two-photon events are reduced with further cuts on the event topology and total visible energy. Details of the tau pair selection are:

1. Each tau-pair candidate must have exactly two jets with an average polar

year	centre-of-mass energy (GeV)	$\int \mathcal{L}$ (pb ⁻¹)
1990	88.2 to 94.2	6.6
1991	88.5 to 93.7	12.9
1992	91.3	23.9
1993	89.4 to 93.0	33.3
1994	91.1	58.0
1995	89.3 to 92.9	33.6

Table 5.1: Integrated luminosity delivered by LEP between the years 1990 and 1995.

angle of $|\cos \theta_{\text{ave}}| < 0.68$ for barrel events, and $0.68 \geq |\cos \theta_{\text{ave}}| < 0.90$ for endcap events.

2. Each of the jets must contain at least one charged track. Tracks used in the jet definition must have ¹ :

- $p_T > 100$ MeV/c.
- $d_0 < 2$ cm
- $z_0 < 75$ cm

3. Electromagnetic calorimeter clusters used in the jet definition must have recorded energies of at least 100 MeV in the barrel, or 200 MeV in the endcap. Clusters in the endcap are also required to extend over at least two lead-glass blocks, with no one block contributing more than 99% to the total cluster energy.

Backgrounds are reduced in the tau-pair sample with the following additional selections:

1. Background from hadronic Z^0 events is reduced by allowing a maximum of

¹see Appendix B for a description of the OPAL track parameters

6 charged tracks and 10 electromagnetic clusters in each event. Figure 5.3 shows a typical hadronic Z^0 decay in the OPAL detector.

2. The background from two-photon events such as $e^+e^- \rightarrow (e^+e^-)X$, where the final state electron and positron escape undetected at low angles and the system X is mis-identified as a tau pair event, is reduced by rejecting events with a separation angle between the two charged jets of less than 165° . Further rejection is obtained with cuts on the visible energy of the event.
3. Minor sources of backgrounds from cosmic rays and beam-gas interactions are suppressed with simple requirements on the location of the primary event vertex and on the time-of-flight signals associated with the tracks. Figure 5.4 shows a typical cosmic ray event in the OPAL detector.
4. Most $e^+e^- \rightarrow e^+e^-$ events are removed by rejecting events with two collinear tracks with large associated energy deposition in the electromagnetic calorimeters, consistent with the passage of electrons. Figure 5.5 shows a typical $e^+e^- \rightarrow e^+e^-$ event in the OPAL detector.
5. Most muon pair events are removed by rejecting events with two collinear tracks with associated activity in the hadronic calorimeters and/or muon chambers, and with small associated energy deposition in the electromagnetic calorimeter, consistent with the passage of muons. Figure 5.6 shows a typical $e^+e^- \rightarrow \mu^+\mu^-$ event in the OPAL detector.

The barrel tau selection yields 110326 tau pair events with background $f^{\text{non-}\tau} = 1.56 \pm 0.10\%$, estimated by data control samples and Monte Carlo background samples. The background from hadronic Z^0 decays in this sample (which is included in $f^{\text{non-}\tau}$) is $f^{Z^0 \rightarrow q\bar{q}} = 0.28 \pm 0.04\%$.

The combined barrel and endcap tau selection yields 147926 tau pair events with background $f^{\text{non-}\tau} = 2.73 \pm 0.27\%$, estimated by data control samples and Monte Carlo background samples. The background from hadronic Z^0 decays in this sample (which is again included in $f^{\text{non-}\tau}$) is $f^{Z^0 \rightarrow q\bar{q}} = 0.68 \pm 0.17\%$.

τ^- Decay Mode	Pre-selection Bias
$\tau^- \rightarrow \nu_\tau K^-$	1.009 ± 0.010
$\tau^- \rightarrow \nu_\tau K^- \pi^0$	0.992 ± 0.012
$\tau^- \rightarrow \nu_\tau K^- K^0$	1.013 ± 0.015
$\tau^- \rightarrow \nu_\tau K^- \pi^0 \pi^0$	1.016 ± 0.037
$\tau^- \rightarrow \nu_\tau K^- K^0 \pi^0$	1.001 ± 0.020
$\tau^- \rightarrow \nu_\tau K^- \pi^0 \pi^0 \pi^0$	1.009 ± 0.037
$\tau^- \rightarrow \nu_\tau K^- K^0 \pi^0 \pi^0$	0.995 ± 0.020
$\tau^- \rightarrow \nu_\tau K^- \pi^- \pi^+$	0.935 ± 0.012
$\tau^- \rightarrow \nu_\tau K^- \pi^- K^-$	0.925 ± 0.013
$\tau^- \rightarrow \nu_\tau K^- \pi^- \pi^+ \pi^0$	0.908 ± 0.012
$\tau^- \rightarrow \nu_\tau K^- \pi^- K^- \pi^0$	0.898 ± 0.013

Table 5.2: Tau-pair selection bias factors for various tau decay modes with charged kaons in the final state.

The tau-pair selection does not select all tau decay modes with equal efficiencies. The ‘selection bias factor’ for signal channel i is the enhancement of that channel (relative to all channels) caused by the tau-pair selection procedure. Thus, if there are a total of N tau decay channels, and B_i and A_i are the number of decays in channel i before and after the tau-pair selection, the selection bias factor for that channel is $(B_i \sum A_i) / (A_i \sum B_i)$, where the summation is over the N channels. In general the selection bias factors are close to unity for most tau decay channels, but they tend to be somewhat less than unity for three-prong tau decays, largely due to the requirement that selected tau-pair candidates must have no more than 6 tracks. Table 5.2 shows selection bias factors for various one- and three-prong tau decay modes that include charged kaons, as determined from a Monte Carlo generated tau-pair sample.

A more complete description of the tau-pair selection, including the details of the background assessment, can be found in reference [17] [52].

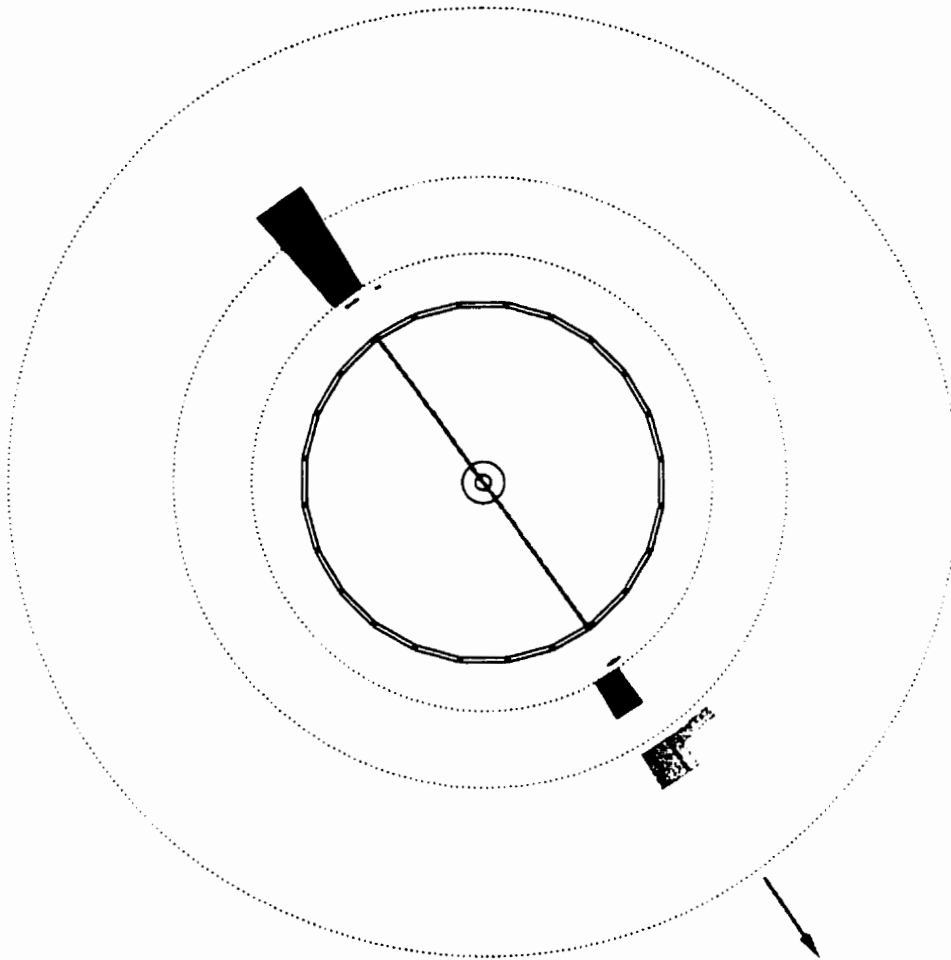


Figure 5.1: A typical $e^+e^- \rightarrow \tau^+\tau^-$ event in the OPAL detector (shown in the $r-o$ plane). The dark shaded boxes represent energy deposition in the electromagnetic calorimeter. The size of the boxes are proportional to the energy deposited by the particle. The lightly shaded boxes represent energy deposition in the hadron calorimeter. The central radial lines represent reconstructed charged particle tracks in the jet chamber, and the arrows on the outer radius of the event display represent hits in the muon chambers. The interpretation of this particular event is a tau-pair decay where one of the tau decays includes an electron, and the other includes a muon.

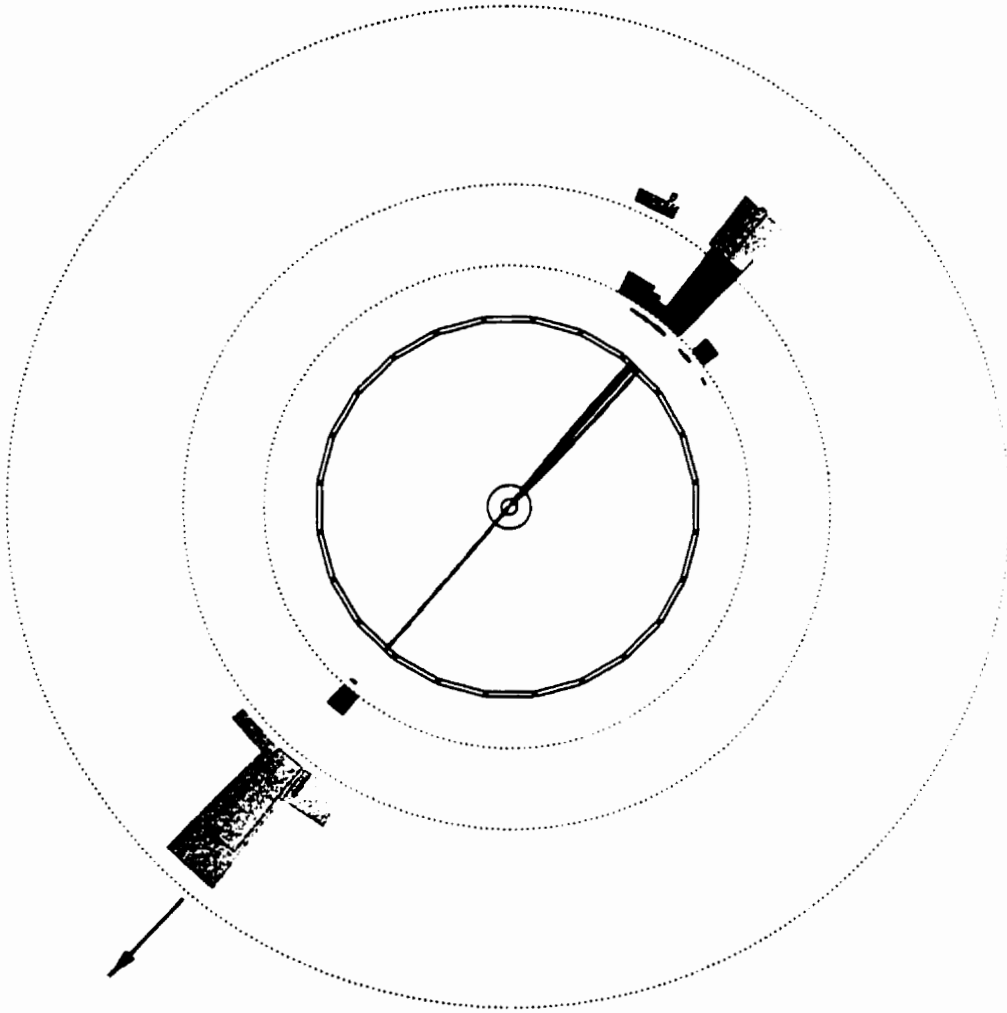


Figure 5.2: Another typical $e^+e^- \rightarrow \tau^+\tau^-$ event in the OPAL detector (shown in the $r - \phi$ plane). The interpretation of this particular event is a tau-pair decay where one of the tau leptons decays to one meson, and the other decays to three mesons.

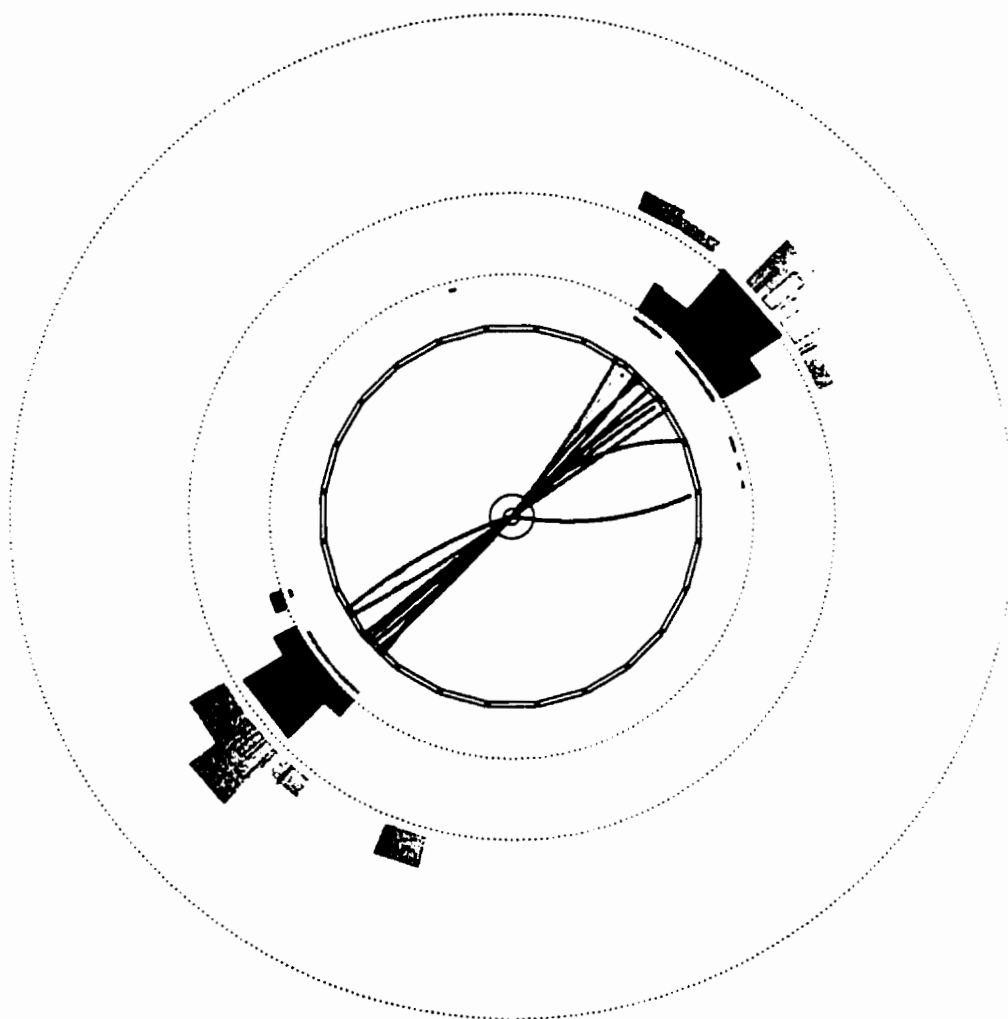


Figure 5.3: A typical hadronic Z^0 decay in the OPAL detector (shown in the $r - \phi$ plane). Note the large number of tracks and calorimeter clusters associated with the event.

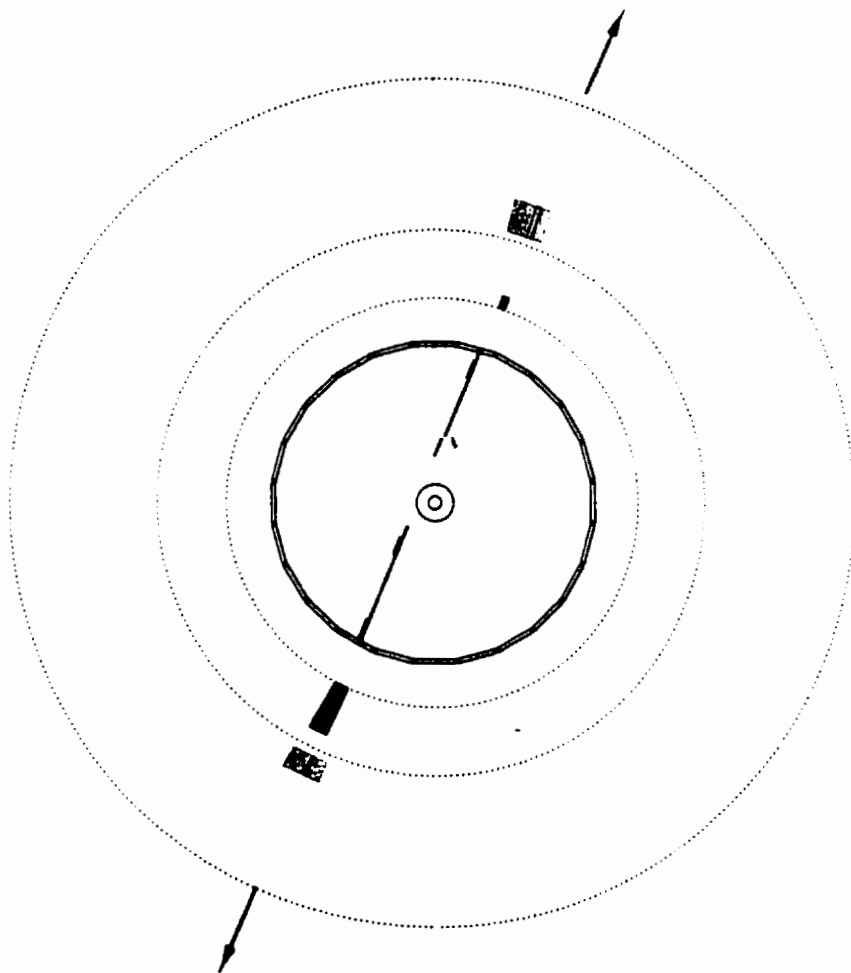


Figure 5.4: A typical cosmic ray event in the OPAL detector (shown in the $r - \phi$ plane). Note that the two tracks are collinear and do not intersect with the origin.

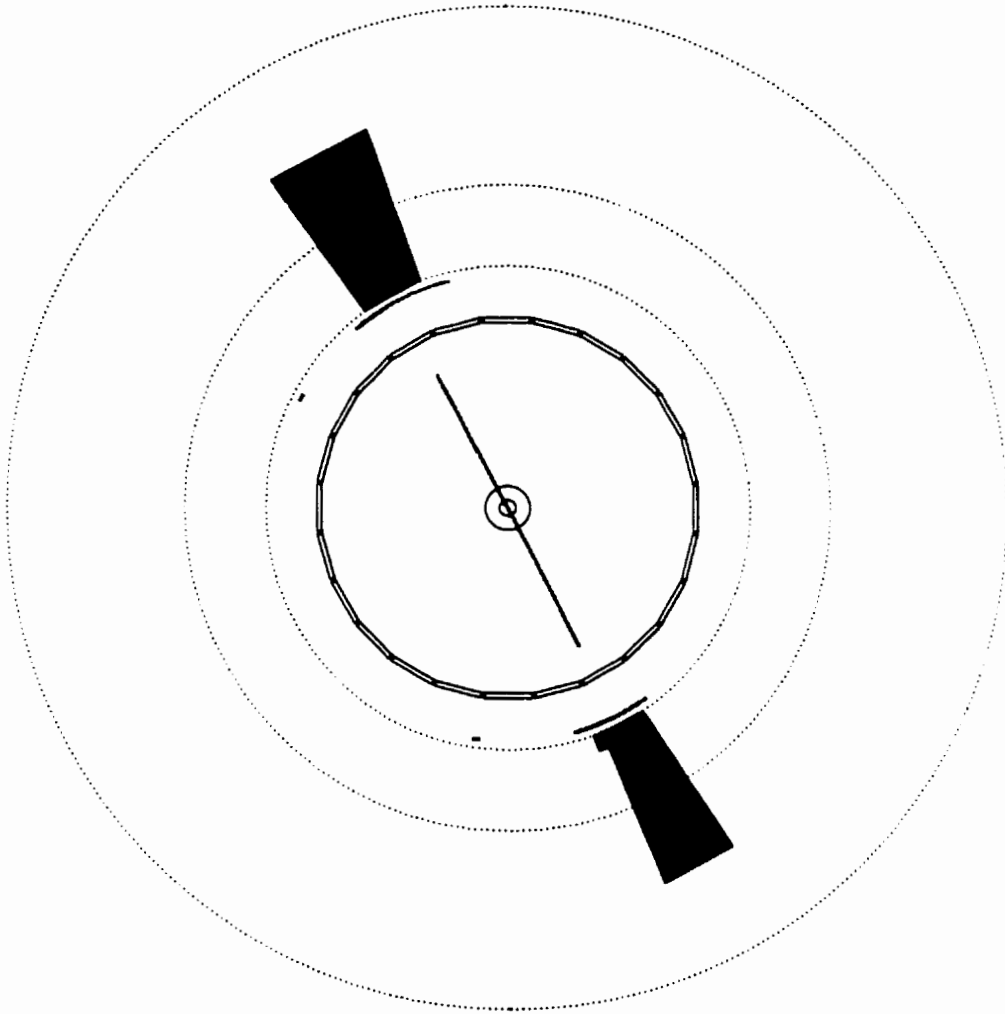


Figure 5.5: A typical $e^+e^- \rightarrow e^+e^-$ event in the OPAL detector (shown in the $r - \phi$ plane). Note the large energy deposition in the electromagnetic calorimeter associated with the two tracks in the event.

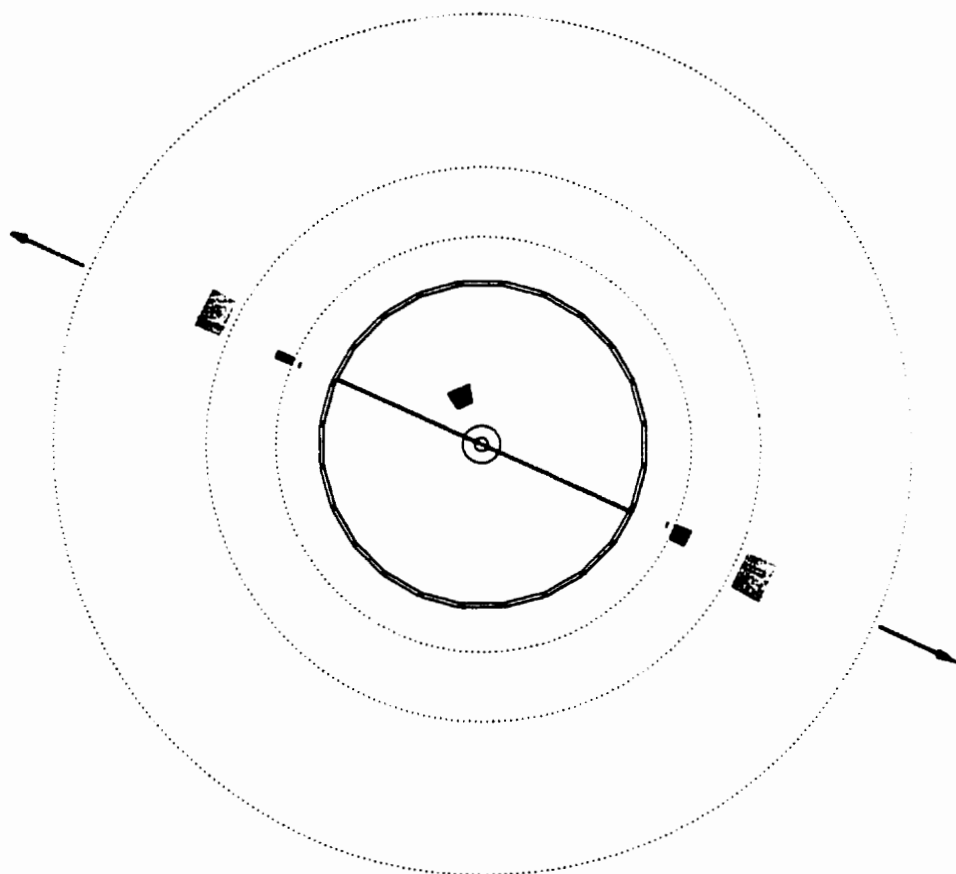


Figure 5.6: A typical $e^+e^- \rightarrow \mu^+\mu^-$ event in the OPAL detector (shown in the $r-\phi$ plane). Note the hits in the muon chambers and the small energy deposition in the electromagnetic and hadron calorimeters associated with the two tracks in the event.

Chapter 6

Monte Carlo Simulation

The simulation of $e^+e^- \rightarrow \tau^+\tau^-$ production for this analysis is performed using the KORALZ 4.0 Monte Carlo generation package [53]. This program takes into account QED bremsstrahlung radiation from the initial state e^+e^- and the final state $\tau^+\tau^-$, and $\mathcal{O}(\alpha)$ electroweak radiative corrections to the cross-section. The tau lepton decay process for the dominant tau decay modes is simulated by the TAUOLA 2.4 decay package [35], which includes both longitudinal spin polarization effects in the tau decay process, and single bremsstrahlung from the final state of the tau decay, except for tau decays to more than four mesons.

The KORALZ/TAUOLA program generates four-momenta of the final state particles of simulated tau decays. The file also includes codes identifying the type of each particle, as well as a data structure containing the history of the particle decays within each event. These four-vectors are input to the detector simulation program known as GOPAL [54], which provides a detailed description of the OPAL detector geometry to the GEANT [55] program, and uses Monte Carlo methods to simulate the passage of particles through the detector material. The results of this simulation are recorded in data structures identical to those read out by the front-end electronics of the OPAL detector. These data structures are then processed with the same software used to reconstruct the data, except that the information used to associate reconstructed quantities with the underlying particles in the event

is retained.

To estimate backgrounds in the candidate samples and the biases introduced to the branching ratios by the tau-pair selection procedure, we use a sample of 600000 simulated tau-pair events generated by the KORALZ/TAUOLA Monte Carlo package. The input branching ratios of the various tau decay modes simulated by TAUOLA 2.4 are derived from current world averages and theoretical predictions.

In order to precisely determine the branching ratios to tau final states with kaons and to study the resonant structure of $\tau^- \rightarrow \nu_\tau K^- \pi^- \pi^+$ and $\tau^- \rightarrow \nu_\tau K^- \pi^- K^+$ decays, large Monte Carlo samples of signal events are also produced. Table 6.1 shows the primary and secondary intermediate resonances used in the Monte Carlo generated sets of $\tau^- \rightarrow \nu_\tau (K\pi\pi)^-$, $\tau^- \rightarrow \nu_\tau (K\pi K)^-$, $\tau^- \rightarrow \nu_\tau (K\pi\pi\pi)^-$, and $\tau^- \rightarrow \nu_\tau (K\pi K\pi)^-$ decay modes that are used in this analysis. Entries marked with an **A** are the samples used to evaluate the efficiencies used in the calculation of the branching ratio central values. All other samples are either used to evaluate the resonant structure of $\tau^- \rightarrow \nu_\tau K^- \pi^- \pi^+$ and $\tau^- \rightarrow \nu_\tau K^- \pi^- K^+$ decays, or as cross-checks in the branching ratio analyses.

The generation of the special samples used as cross-checks in this analysis confronts the somewhat uncommon complication of the severe phase-space restrictions in tau decay chains such as $\tau^- \rightarrow \nu_\tau K_1(1270) \rightarrow \nu_\tau (\rho(770)K)^-$. Modifications to the default version of Tauola are therefore made to take these restrictions into account using the method suggested in reference [56]. Appendix A discusses this method in detail.

Decays of the $K_1(1270)$ with more than three mesons in the final state, such as $K_1(1270) \rightarrow K\omega \rightarrow K\pi\pi\pi$, are not generated for this study. The relative branching ratios of the $K_1(1270)$ to the decays which are generated, as seen in Table 6.1, are thus re-weighted to sum to 1. Interference effects between the various $K_1(1270)$ decay chains are neglected.

All Monte Carlo generated event samples used in this analysis are passed

through the full detector simulation and subjected to the same analysis chain as the data.

τ^- Decay Mode	Primary Resonance	Daughters	Comments
$\nu_\tau(\bar{K}\pi\pi)^-$	$K_1(1400)$	$(\rho(\bar{770})K)^-$ $(K^*(892)\pi)^-$	A <i>a</i>
	$K_1(1400)$	$(K^*(892)\pi)^-$	<i>b, c</i>
	$K_1(1270)$	$(\rho(\bar{770})K)^-$ (49%) $(K^*(1430)\pi)^-$ (32%) $(K^*(892)\pi)^-$ (19%)	<i>b, c, d</i>
	non-resonant	$(\rho(\bar{770})K)^-$	<i>b</i>
	non-resonant	$(K^*(892)\pi)^-$	<i>b</i>
	non-resonant	non-resonant	<i>b</i>
$\nu_\tau(\bar{K}\pi\bar{K})^-$	$a_1(1250)$ and $\rho'(1700)$	$(K^*(892)K)^-$	A <i>a</i>
	non-resonant	$(\rho(\bar{770})K)^-$	<i>b</i>
	non-resonant	$(K^*(892)K)^-$	<i>b</i>
	non-resonant	non-resonant	<i>b</i>
$\nu_\tau(\bar{K}\pi\pi\pi)^-$	non-resonant	non-resonant	A <i>b</i>
	non-resonant	ωK^-	<i>b</i>
$\nu_\tau(\bar{K}\pi\bar{K}\pi)^-$	non-resonant	non-resonant	A <i>b</i>
	non-resonant	$(K^*(892)K\pi)^-$	<i>b</i>

^A Used to calculate central values of the branching ratios.

^a Default version of Tauola 2.4.

^b Modified version of Tauola 2.4.

^c Phase-space limitations in the decay chain are taken into account.

^d Interference effects between the $K_1(1270)$ decay chains are neglected.

Table 6.1: Intermediate resonant structure assumptions made in the generation of special Monte Carlo samples of $\tau^- \rightarrow \nu_\tau(\bar{K}\pi\pi)^-$, $\tau^- \rightarrow \nu_\tau(\bar{K}\pi\bar{K})^-$, $\tau^- \rightarrow \nu_\tau(\bar{K}\pi\pi\pi)^-$, and $\tau^- \rightarrow \nu_\tau(\bar{K}\pi\bar{K}\pi)^-$ decay modes. Entries marked with an **A** are the samples used to evaluate the efficiencies used in the calculation of the branching ratio central values. All other samples are either used to evaluate the resonant structure of $\tau^- \rightarrow \nu_\tau K^- \pi^- \pi^+$ and $\tau^- \rightarrow \nu_\tau K^- \pi^- K^+$ decays, or as cross-checks in the branching ratio analyses.

Chapter 7

One-Prong Branching Ratios

Measurements of the branching ratios of one-prong tau decays to final states with a charged kaon may be used to test the theoretical predictions for those branching ratios, as shown earlier in Chapter 2 in Table 2.2.

One-prong tau decay modes with a charged kaon in the final state are dominated by the $\tau^- \rightarrow \nu_\tau K^-$ and $\tau^- \rightarrow \nu_\tau K^- \pi^0$ decay modes. Measurement of the $\tau^- \rightarrow \nu_\tau K^-$ branching ratio at OPAL relies upon the good charged particle identification capabilities of the jet chamber. Unfortunately, the electromagnetic shower shape resolution and energy resolution is too poor at OPAL to allow precise measurements of the branching ratios of other exclusive one-prong tau decay modes with charged kaons, such as $\tau^- \rightarrow \nu_\tau K^- \pi^0$, and thus such studies are not attempted here.

Measurement of the $\tau^- \rightarrow \nu_\tau K^-$ branching ratio begins with the determination of the number of $\tau^- \rightarrow \nu_\tau K^- \geq 0h^0$ decays in the one-prong tau decay sample, where the h^0 notation refers to either a π^0 or a K^0 . Information provided by the electromagnetic calorimeter is then used to determine the number of $\tau^- \rightarrow \nu_\tau K^-$ decays in this sample. The $\tau^- \rightarrow \nu_\tau K^-$ branching ratio is obtained by correcting this number for backgrounds and selection inefficiencies.

7.1 Event Selection

Event selection begins with the barrel tau-pair candidate sample described in Chapter 5.

One-prong tau decays are selected from this sample by choosing tau decay cones containing only one well-reconstructed charged track. Tracks in this sample are required to have at least 40 jet chamber hits used in the calculation of the measured dE/dx , to have at least 3 hits in the z -chambers, and to have reconstructed momentum between 2 and 50 GeV/c. The number of candidates in the sample selected by this procedure is 143528.

The number of charged kaons in the sample is determined by maximising a likelihood function based on dE/dx . After correction for backgrounds and selection inefficiencies, this yields the $\tau^- \rightarrow \nu_\tau K^- \geq 0h^0$ branching ratio. As a cross-check, to ensure that the $\tau^- \rightarrow \nu_\tau h^- \geq 0h^0$ efficiency estimates are accurate, the $\tau^- \rightarrow \nu_\tau \pi^- \geq 0h^0$ branching ratio is also determined in an analogous fashion, and compared to the world average.

7.2 Inclusive $\tau^- \rightarrow \nu_\tau K^- \geq 0h^0$ Branching Ratio

The tracks in the one-prong tau decay candidate sample consist of electrons, muons, pions, and kaons from both tau decays and non-tau sources. To determine the number of charged kaons in the sample, a maximum likelihood fit to the ionisation energy loss distribution of the tracks in the sample is performed. The likelihood function used in the fit is:

$$\mathcal{L} = \exp \left[-\frac{1}{2} \left(\frac{f'_\mu - f_\mu}{\Delta f'_\mu} \right)^2 \right] \prod_{j=1..N} \sum_{k=e,\mu,\pi,K} f_k W^{kj}. \quad (7.1)$$

where W^{kj} is the dE/dx weight of charged particle j under particle hypothesis k .

$$W^{kj} = \frac{1}{\sqrt{2\pi}s(\beta_j)s_{res}\sigma_{kj}} \exp \left[-\frac{1}{2} \left(\frac{D_{meas}^j - f(\phi_j) - s(\beta_j)D_{pred}^{kj}}{s(\beta_j)s_{res}\sigma_{kj}} \right)^2 \right]. \quad (7.2)$$

and where,

f_k is the fraction of particle type k in the sample, where k is either pion, kaon, muon, or electron. The values of f_k are constrained to be non-negative, and the sum is constrained to be 1.

f'_μ and $\Delta f'_\mu$ are the fraction, and uncertainty on the fraction, of muons in the sample, as estimated by Monte Carlo generated events, corrected using information from data and Monte Carlo muon control samples that are selected using information from the OPAL muon chambers.

N is the total number of particles in the sample.

D_{meas}^j is the measured dE/dx of the j^{th} charged particle.

D_{pred}^{kj} is the predicted dE/dx for charged particle j , calculated with the OPAL parameterisation under particle hypothesis k , as derived from the measured dE/dx of charged particles in hadronic Z^0 events.

σ_{kj} is the dE/dx uncertainty, calculated using the OPAL parameterisation, as derived from the measured dE/dx of hadronic Z^0 events.

s_{res} is the multiplicative correction to σ_{kj} , as determined from the one-prong control samples as described in Chapter 4.

$s(\beta)$ is the β dependent multiplicative correction to D_{pred} , as determined from the one-prong control samples.

$f(\phi)$ is the ϕ dependent correction to the measured dE/dx , as obtained from the one-prong control samples.

Efforts are made to obtain a dE/dx parameterisation for the tau decay environment that is optimal for many particle species over a wide range of momenta. However, it is possible that the dE/dx corrections described in Chapter 4 may be somewhat more (or less) optimal for pions than they are for kaons in the momentum range of interest. Thus, to correct for any possible species-dependent quality differences in the parameterisation of dE/dx , an extra factor, C_K , is allowed to multiply the kaon predicted energy loss, D_{pred}^K , and is allowed to vary freely in the fit using the likelihood function found in Equation 7.1. The value of C_K returned by the fit is $C_K = 0.9943 \pm 0.0009$.

Independent likelihood fits are performed in 13 momentum bins of variable size from 2 to 50 GeV/c. A test of the fit with Monte Carlo generated samples verifies that the resulting estimates for the kaon fraction have biases within the range $-0.25\sigma_{f_K}$ to $0.75\sigma_{f_K}$ at the 95% confidence level, where σ_{f_K} is the typical statistical uncertainty returned by the fit. Thus, biases resulting from the fit procedure are neglected.

The number of charged kaons and pions found in the sample, summed over all momentum bins, is given in Table 7.1, and the stretch dE/dx distribution of tracks in all momentum bins of the sample is shown in Figure 7.1. The normalisation of the predicted distributions of the kaons, pions, muons, and electrons in the sample is obtained from the results of the likelihood fit. The momentum distributions of the charged kaons and pions in the sample, as estimated by the likelihood fit, are shown in Figure 7.2.

7.2.1 The Branching Ratio Calculation

To determine the $\tau^- \rightarrow \nu_\tau K^- \geq 0h^0$ branching ratio, the number of charged kaons found by the dE/dx likelihood fit in the one-prong candidate sample is corrected for backgrounds and selection inefficiencies:

$$B_{K^- \geq 0h^0} = \frac{N_{\text{TOTAL}}^K - N_{\text{bkgnd}}^K}{\epsilon_{K^- \geq 0h^0} N_\tau (1 - f^{\text{non-}\tau})}$$

# of τ candidates	220652
$f^{\text{non-}\tau}$	$1.56 \pm 0.10\%$
# in one-prong sample	143528
N_{TOTAL}^{π}	$75566 \pm 389 \pm 246$
N_{bkgnd}^{π}	89 ± 16
$\epsilon_{\pi^- \rightarrow 0h^0}$	$0.721 \pm 0.001 \pm 0.001$
N_{TOTAL}^K	$2526.2 \pm 64.0 \pm 52.0$
N_{bkgnd}^K	8.8 ± 3.8
$\epsilon_{K^- \rightarrow 0h^0}$	$0.762 \pm 0.006 \pm 0.007$

Table 7.1: Pion and kaon composition of the one-prong tau decay candidate sample, as estimated by the likelihood fit to the measured dE/dx of tracks in the sample. The first uncertainty on N_{TOTAL}^{π} and N_{TOTAL}^K is the statistical uncertainty from the fit, and the second is due to the systematic uncertainty in the dE/dx correction factors. Also shown are the estimated backgrounds in N_{TOTAL}^{π} and N_{TOTAL}^K , along with the efficiencies for signal events to contribute to the one-prong tau decay sample. The first uncertainty on each efficiency estimate is due to the limited statistics of the Monte Carlo generated samples, while the second is due to the uncertainty in the various branching ratios used to calculate the efficiency, as listed in Table 7.3.

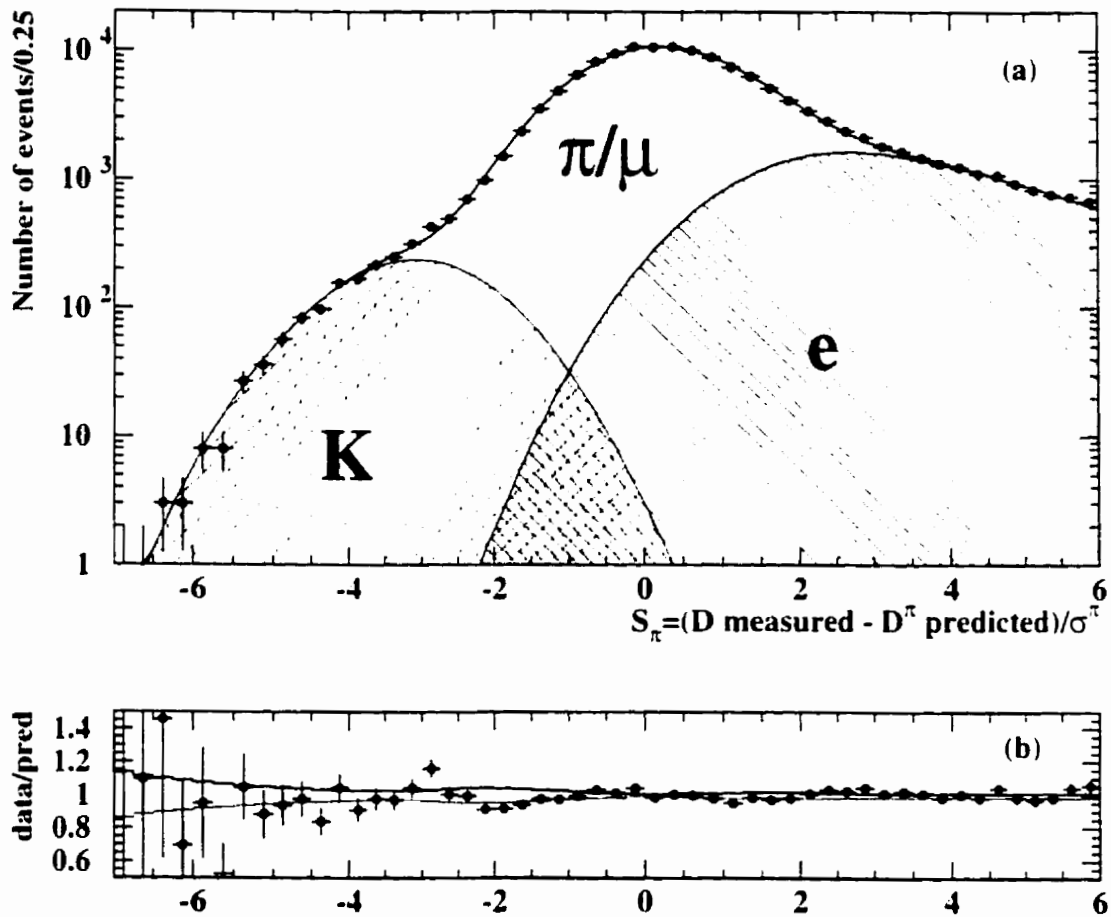


Figure 7.1: (a) is the stretch dE/dx distribution under a pion hypothesis for tracks in the data $\tau^- \rightarrow \nu_\tau h^- \geq 0h^0$ candidate sample (points). The overlaid curves are the predicted distributions for kaons, pions, muons, and electrons in the sample. The normalisation of the curves is obtained from the results of the likelihood fit described in Section 7.2. (b) is the distribution of the data points in plot (a) divided by the predicted distribution. The shaded area represents the approximate one sigma dE/dx systematic uncertainty envelope on the predicted distribution. The χ^2 per degree of freedom between the data and a line centred at $y = 1$, taking into account both statistical and dE/dx systematic uncertainties, is $36.5/47$.

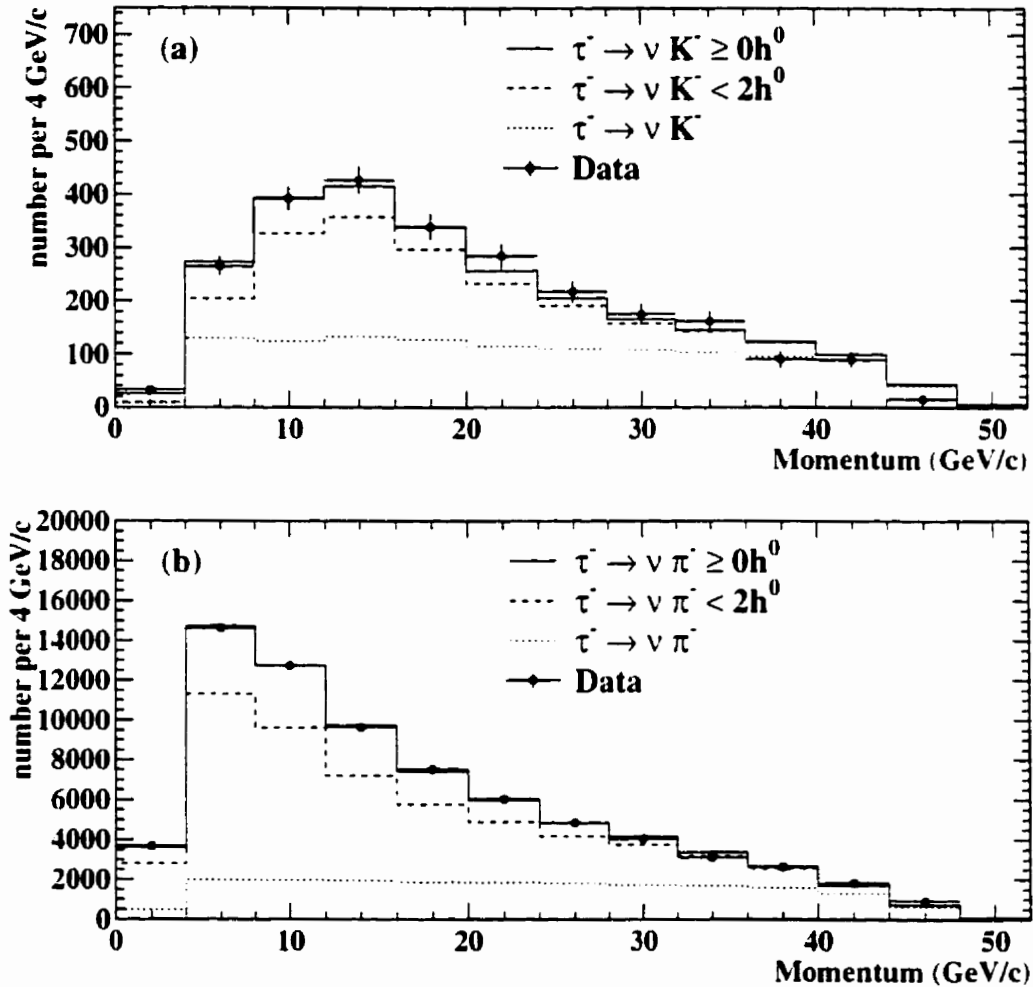


Figure 7.2: (a) and (b) are the momentum distributions of charged kaons and pions, respectively, in the data one-prong tau decay sample (points), as estimated from the results of the dE/dx likelihood fit described in Section 7.2. The histograms are the momentum distributions predicted by Monte Carlo generated $\tau^- \rightarrow \nu_\tau K^- \geq 0h^0$ and $\tau^- \rightarrow \nu_\tau \pi^- \geq 0h^0$ events. The overall normalisation of the predicted distributions comes from the results of the dE/dx likelihood fit, while the relative normalisation of the exclusive decay modes contributing to the sample is taken from the relevant world average branching ratios appearing in reference [1].

where

N_τ is the number of tau decay candidates. There were 220652 tau decay candidates recorded in the barrel region of the OPAL detector between the years 1990 and 1995.

$f^{\text{non-}\tau}$ is the estimated background from non- τ sources in the tau decay candidates ($f^{\text{non-}\tau} = 1.56 \pm 0.10\%$).

$N_{\text{TOTAL}}^{\text{K}}$ is the total number of kaons in the one-prong tau decay sample, as estimated by the likelihood fit. The number of kaons summed over all momentum bins in the sample is shown in Table 7.1.

$N_{\text{bkgrnd}}^{\text{K}}$ is the number of background kaons in the one-prong tau decay sample, as estimated by Monte Carlo generated tau decay and hadronic Z^0 samples. The number of background kaons summed over all momentum bins in the sample is shown in Table 7.1.

$\epsilon_{\text{K}^- \geq 0\text{h}^0}$ is the efficiency for $\tau^- \rightarrow \nu_\tau \text{K}^- \geq 0\text{h}^0$ decays in the tau-pair candidate sample to contribute kaons to the one-prong tau decay sample, and is shown in Table 7.1. The efficiency has been corrected for biases introduced by the tau-pair selection procedure, and the uncertainty on the efficiency includes the systematic uncertainty arising from this correction.

The result of the branching ratio calculation is

$$\text{Br}(\tau^- \rightarrow \nu_\tau \text{K}^- \geq 0\text{h}^0) = 1.525 \pm 0.039 \pm 0.036\%,$$

where the first uncertainty is statistical and the second is systematic. A summary of the systematic uncertainties, all of which will be described in proceeding sections, is shown in Table 7.2.

As a cross-check to ensure that the $\tau^- \rightarrow \nu_\tau \text{h}^- \geq 0\text{h}^0$ efficiency estimates derived from the Monte Carlo generated events are accurate, we also determine the

	Branching Ratios (%)		
	$B_{\pi^- \geq 0h^0}$	$B_{K^- \geq 0h^0}$	B_{K^-}
Central value	48.17	1.525	0.651
σ (stat)	± 0.25	± 0.039	± 0.026
σ (dE/dx sys)	± 0.16	± 0.031	± 0.018
σ (E/p and N_{clus} modelling)	-	-	± 0.009
σ (MC stat)	± 0.09	± 0.012	± 0.006
σ (efficiency sys)	± 0.05	± 0.014	± 0.010

Table 7.2: Summary of the branching ratio central values and sources of uncertainties. The last uncertainty is due to the systematic uncertainty in the efficiency correction arising from the uncertainties in the various branching ratios used in the weighted average calculation of the $\tau^- \rightarrow \nu_\tau K^- \geq 0h^0$, $\tau^- \rightarrow \nu_\tau \pi^- \geq 0h^0$, and $\tau^- \rightarrow \nu_\tau K^- \geq 1h^0$ efficiencies.

$\tau^- \rightarrow \nu_\tau \pi^- \geq 0h^0$ branching ratio. Thus, in a completely analogous fashion to the $\tau^- \rightarrow \nu_\tau K^- \geq 0h^0$ branching ratio calculation, the total number of charged pions found in the one-prong tau decay sample by the likelihood fit is corrected for backgrounds and the $\tau^- \rightarrow \nu_\tau \pi^- \geq 0h^0$ efficiency to yield:

$$\text{Br}(\tau^- \rightarrow \nu_\tau \pi^- \geq 0h^0) = 48.17 \pm 0.25 \pm 0.19\%.$$

where the first uncertainty is statistical and the second is systematic. The linear correlation coefficient between the OPAL $\tau^- \rightarrow \nu_\tau K^- \geq 0h^0$ and $\tau^- \rightarrow \nu_\tau \pi^- \geq 0h^0$ branching ratios is approximately -20% . The OPAL $\tau^- \rightarrow \nu_\tau \pi^- \geq 0h^0$ branching ratio is consistent with the world average, derived from the branching ratios of the tau to the various exclusive final states that include a charged pion listed in reference [1]

$$\text{Br}(\tau^- \rightarrow \nu_\tau \pi^- \geq 0h^0) = 48.17 \pm 0.23\%.$$

7.2.2 dE/dx Systematic Studies

A significant source of systematic uncertainty in the measurement of the inclusive branching ratio is the uncertainty in the parameterisation of the predicted energy loss. To assess this systematic, we determine the sensitivity of the likelihood estimates of the number of kaons within the data sample to the uncertainties in the dE/dx correction factors obtained from the one-prong control samples. The likelihood function shown in Equation 7.1 is therefore modified such that:

$$\mathcal{L}' = \exp\left(-\frac{1}{2}(\mathbf{n}' - \mathbf{n})^T \mathbf{V}^{-1}(\mathbf{n}' - \mathbf{n})\right) \mathcal{L},$$

where

\mathbf{n}' is a vector containing the central values of the dE/dx correction factors that describe the functions $f(\phi)$, $s(\beta)$, and s_{res} , where the central values are as derived from the fits to the one-prong control samples.

\mathbf{n} is a vector containing the dE/dx correction factors used in the likelihood fit.

\mathbf{V} is the covariance matrix for the dE/dx correction factors, as derived from the fits to the one-prong control samples.

In the first iteration, the correction factors are allowed to vary in the fit, and the returned values are found to be consistent with the input values. In the second iteration, the likelihood fit is repeated, this time keeping the dE/dx correction factors fixed to the values from the first iteration. The systematic uncertainty in N_{TOTAL}^K (and N_{TOTAL}^π) due to the parameterisation of dE/dx is then obtained from the square root of the quadrature difference of the fit uncertainties in N_{TOTAL}^K (N_{TOTAL}^π) from the two iterations, and is shown in Table 7.1.

The assessment of systematic uncertainties in this fashion is referred to as the ‘prior-belief method’. Essentially, it allows parameters to float in a fit, constrained by prior knowledge of the parameter central values and uncertainties obtained from other sources.

7.2.3 Efficiency Correction

The efficiencies for kaons and pions from signal events in the tau-pair candidate sample to enter the data sample are estimated using signal events generated with the KORALZ 4.0 Monte Carlo generator and the Tauola 2.4 decay package, as described in Chapter 6. The efficiency for $\tau^- \rightarrow \nu_\tau K^- \geq 0h^0$ decays in the tau-pair candidate sample to contribute to the one-prong sample, $\epsilon_{K^- \geq 0h^0}$, is calculated via

$$\epsilon_{K^- \geq 0h^0} = f\epsilon_{K^-} + (1 - f)\epsilon_{K^- \geq 1h^0},$$

where f is the ratio, derived from OPAL data in Section 7.3, of the exclusive $\tau^- \rightarrow \nu_\tau K^-$ branching ratio to the inclusive $\tau^- \rightarrow \nu_\tau K^- \geq 0h^0$ branching ratio. The $\epsilon_{K^- \geq 1h^0}$ efficiency is calculated from the average of the relevant efficiencies appearing in Table 7.3, weighted by the associated world average branching ratios. All efficiencies in Table 7.3 have been corrected for the relevant tau-pair selection bias factors shown in Table 5.2, and the efficiency uncertainties include the systematic uncertainty arising from this correction.

The efficiency for $\tau^- \rightarrow \nu_\tau \pi^- \geq 0h^0$ decays in the tau-pair candidate sample to contribute to the one-prong sample, $\epsilon_{\pi^- \geq 0h^0}$, is calculated in an analogous fashion, except that the ratio of the $\tau^- \rightarrow \nu_\tau \pi^-$ branching ratio relative to the $\tau^- \rightarrow \nu_\tau \pi^- \geq 0h^0$ branching ratio is taken from world averages.

The variation of the branching ratio due to alternative intermediate resonant structure scenarios for the $\tau^- \rightarrow \nu_\tau K^- \pi^0 \pi^0$ final state is assessed using efficiency estimates from signal events generated by the modified version of Tauola 2.4 through non-resonant production only. The efficiency calculated from this sample for $\tau^- \rightarrow \nu_\tau K^- \pi^0 \pi^0$ to contribute to the data candidates is within 0.4σ of the central value, where σ represents the combined Monte Carlo statistical uncertainties. Since the two different scenarios produce consistent results for the efficiency, and since there is no a priori reason to expect a strong efficiency dependence on the intermediate resonant structure, no systematic uncertainty is assigned.

In a similar fashion, the variation of the branching ratio due to alternative intermediate resonant structure scenarios for the $\tau^- \rightarrow \nu_\tau K^- K^0 \pi^0$ final state is explored using events generated through non-resonant production only. The $\tau^- \rightarrow \nu_\tau K^- K^0 \pi^0$ efficiency calculated from these events is within 0.6σ of the central value, thus no systematic uncertainty is assigned.

Since the observed momentum distributions for both the pions and the kaons in the sample are well described by the Monte Carlo generated events, and since the $\tau^- \rightarrow \nu_\tau \pi^- \geq 0h^0$ branching ratio extracted from the OPAL data is in good agreement with the world average, no systematic uncertainty is assigned for possible error in either the estimate of the total efficiency, or the momentum dependence of the efficiency estimates, since it is apparent that such errors are small relative to the other systematic uncertainties.

7.2.4 Background Correction

The number of background kaons in N_{TOTAL}^K is estimated by applying the same selection criteria to Monte Carlo samples of hadronic Z^0 decays and three-prong tau decays. From the number of selected events that contain kaons, the estimated number of background kaons is derived, as summarised in Table 7.1. The dominant source of background kaons is low-multiplicity hadronic Z^0 events.

The number of background pions in N_{TOTAL}^π is estimated in an analogous fashion.

7.3 Exclusive Branching Ratios

To distinguish between one-prong tau final states with and without accompanying neutral particles, information from the electromagnetic calorimeter is used. Tau decays that include neutral particles tend to have a larger relative electromagnetic energy deposition, E/p , associated with the tau decay cone than tau decays without accompanying neutrals. Such decays also tend to have a larger number of

τ^- Decay Mode	BR (%)	Efficiency
$\tau^- \rightarrow \nu_\tau \pi^-$	11.080 ± 0.05	0.810 ± 0.003
$\tau^- \rightarrow \nu_\tau \pi^- \pi^0$	25.310 ± 0.06	0.725 ± 0.002
$\tau^- \rightarrow \nu_\tau \pi^- K^0$	0.780 ± 0.024	0.604 ± 0.007
$\tau^- \rightarrow \nu_\tau \pi^- \pi^0 \pi^0$	9.210 ± 0.027	0.642 ± 0.003
$\tau^- \rightarrow \nu_\tau \pi^- K^0 K^0$	0.116 ± 0.031	0.454 ± 0.016
$\tau^- \rightarrow \nu_\tau \pi^- K^0 \pi^0$	0.360 ± 0.050	0.550 ± 0.015
$\tau^- \rightarrow \nu_\tau \pi^- \pi^0 \pi^0 \pi^0$	1.110 ± 0.140	0.569 ± 0.005
$\tau^- \rightarrow \nu_\tau K^-$	-	0.843 ± 0.010
$\tau^- \rightarrow \nu_\tau K^- \pi^0$	0.52 ± 0.06	0.757 ± 0.011
$\tau^- \rightarrow \nu_\tau K^- K^0$	0.161 ± 0.024	0.661 ± 0.013
$\tau^- \rightarrow \nu_\tau K^- \pi^0 \pi^0$	0.081 ± 0.027	0.664 ± 0.025
$\tau^- \rightarrow \nu_\tau K^- K^0 \pi^0$	0.133 ± 0.031	0.544 ± 0.012
$\tau^- \rightarrow \nu_\tau K^- \pi^0 \pi^0 \pi^0$	$0.25 B_{\tau^- \rightarrow \nu_\tau K^- \pi^0 \pi^0}$	0.643 ± 0.025
$\tau^- \rightarrow \nu_\tau K^- K^0 \pi^0 \pi^0$	$0.30 B_{\tau^- \rightarrow \nu_\tau K^- K^0 \pi^0}$	0.560 ± 0.012

Table 7.3: Branching ratios and efficiencies used to estimate the efficiencies for the $\tau^- \rightarrow \nu_\tau K^- \geq 0h^0$ and $\tau^- \rightarrow \nu_\tau \pi^- \geq 0h^0$ decays in the tau-pair sample to contribute to the one-prong sample. All efficiencies have been corrected for biases introduced by the tau-pair candidate selection procedure, as described in Chapter 5. The branching ratios for $\tau^- \rightarrow \nu_\tau K^- \pi^0 \pi^0 \pi^0$ and $\tau^- \rightarrow \nu_\tau K^- K^0 \pi^0 \pi^0$ are estimated from three-prong tau decay measurements and are taken to have 100% uncertainty.

associated clusters, N_{clus} , in the electromagnetic calorimeter than tau decays without neutrals. To ensure accurate modelling of the E/p and N_{clus} distributions of one-prong tau decays to charged kaons, corrections to the Monte Carlo simulation are obtained from a data $\tau^- \rightarrow \nu_\tau \pi^- \geq 0h^0$ control sample. The following sections describe these corrections, and how they are applied in the determination of the $\tau^- \rightarrow \nu_\tau K^-$ branching ratio.

7.3.1 Corrections to the Modelling of E/p and N_{clus}

The $(p, E/p)$ and (p, N_{clus}) distributions of data $\tau^- \rightarrow \nu_\tau \pi^- \geq 0h^0$ decays are used to determine corrections to the Monte Carlo modelling of the E/p and N_{clus} distributions of $\tau^- \rightarrow \nu_\tau K^- \geq 0h^0$ decays. To this aim, the data one-prong tau decay sample is divided into 13 bins of momentum between 2 to 50 GeV/c and 6 bins of E/p , and the number of charged pions and kaons within each bin is determined by maximising the dE/dx likelihood function seen in Equation 7.1. After correction for backgrounds, this procedure yields the $(p, E/p)$ distributions of $\tau^- \rightarrow \nu_\tau \pi^- \geq 0h^0$ and $\tau^- \rightarrow \nu_\tau K^- \geq 0h^0$ decays. The data one-prong sample is also divided into 13 bins of momentum and 4 bins of N_{clus} , and the (p, N_{clus}) distributions of $\tau^- \rightarrow \nu_\tau \pi^- \geq 0h^0$ and $\tau^- \rightarrow \nu_\tau K^- \geq 0h^0$ decays are determined in an analogous fashion.

The momentum distribution of the charged pions in the one-prong tau decay sample, as shown in Figure 7.2, appears to be adequately modelled by Monte Carlo generated $\tau^- \rightarrow \nu_\tau \pi^- \geq 0h^0$ events. However, the E/p and N_{clus} distributions, obtained by summing the $(p, E/p)$ and (p, N_{clus}) distributions over momentum bins, are not as well modelled by the Monte Carlo, as is shown in Figure 7.3.

Corrections to E/p

Separate corrections are derived for the Monte Carlo E/p modelling of $\tau^- \rightarrow \nu_\tau \pi^-$, $\tau^- \rightarrow \nu_\tau \pi^- \pi^0$, and $\tau^- \rightarrow \nu_\tau \pi^- \pi^0 \pi^0$ decays. These three decay modes produce 95% of the charged pions found in the one-prong tau decay sample. Since the

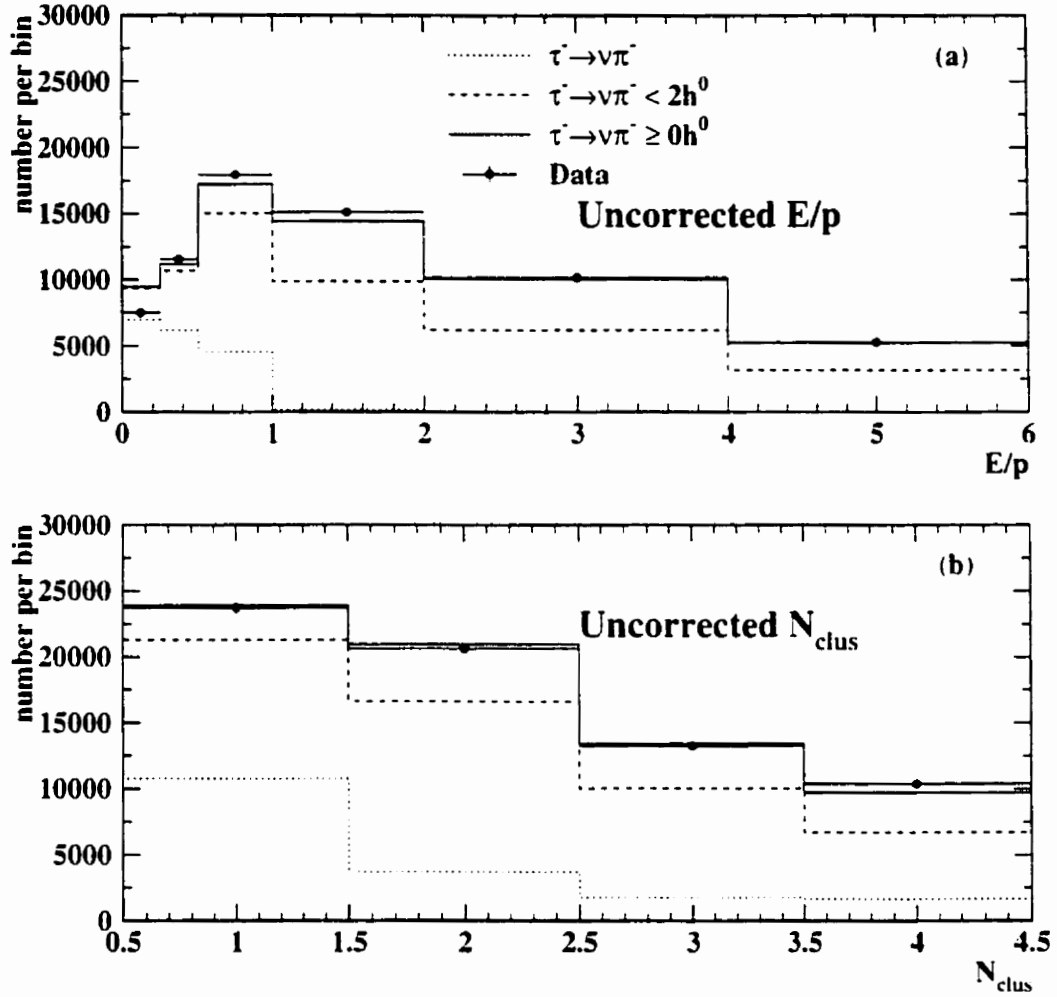


Figure 7.3: (a) and (b) are the uncorrected E/p and N_{clus} distributions, respectively, of Monte Carlo generated $\tau^- \rightarrow \nu_\tau \pi^- \geq 0h^0$ decays (histograms), along with the E/p and N_{clus} distributions of data one-prong tau decays with a charged pion in the final state (points). The relative normalisations of the various exclusive tau decays that contribute to the sample are taken from the relevant world average branching ratios listed in reference [1]. Backgrounds are on the order of 0.2% or less and are neglected in the plots. The last bin in each of the distributions contains overflow events.

$\tau^- \rightarrow \nu_\tau \pi^-$ E/p distribution is qualitatively quite similar to that of $\tau^- \rightarrow \nu_\tau K^-$, the E/p corrections obtained for $\tau^- \rightarrow \nu_\tau \pi^-$ are applied to the Monte Carlo modelling of the $\tau^- \rightarrow \nu_\tau K^-$ E/p . In a similar fashion, the shape of the $\tau^- \rightarrow \nu_\tau \pi^- \pi^0$ ($\tau^- \rightarrow \nu_\tau \pi^- \pi^0 \pi^0$) E/p distribution is qualitatively similar to that of $\tau^- \rightarrow \nu_\tau K^- h^0$ ($\tau^- \rightarrow \nu_\tau K^- \geq 2h^0$) decays, and thus the associated corrections are used to correct the E/p of the Monte Carlo generated $\tau^- \rightarrow \nu_\tau K^- h^0$ ($\tau^- \rightarrow \nu_\tau K^- \geq 2h^0$).

The corrections to the $\tau^- \rightarrow \nu_\tau \pi^-$, $\tau^- \rightarrow \nu_\tau \pi^- \pi^0$, and $\tau^- \rightarrow \nu_\tau \pi^- \pi^0 \pi^0$ Monte Carlo modelling of E/p are obtained by first correcting the number of charged pions within each $(p, E/p)$ bin of the one-prong tau decay sample for background pions from hadronic Z^0 events. The number of pions in each bin is also corrected for the number of pions from tau sources other than $\tau^- \rightarrow \nu_\tau \pi^-$, $\tau^- \rightarrow \nu_\tau \pi^- \pi^0$, and $\tau^- \rightarrow \nu_\tau \pi^- \pi^0 \pi^0$ decays using world average branching ratios and information from Monte Carlo generated events. The following χ^2 function is then minimised:

$$\chi^2 = \sum_i \sum_j \left[\frac{(N_{ij}^\pi - \sum_l N_\tau (1 - f^{\text{non-}\tau}) \epsilon_l B_l s_i^l S_{ij}^l S_j^l)}{\Delta N_{ij}^\pi} \right]^2. \quad (7.3)$$

where the index i runs over the momentum bins, the index j runs over the E/p bins, and the index l runs over $\tau^- \rightarrow \nu_\tau \pi^-$, $\tau^- \rightarrow \nu_\tau \pi^- \pi^0$, and $\tau^- \rightarrow \nu_\tau \pi^- \pi^0 \pi^0$. Also:

N_{ij}^π is the number of charged pions, after corrections for non- $\tau^- \rightarrow \nu_\tau \pi^- \leq 2\pi^0$ background, found by the dE/dx likelihood fit in the $(i, j)^{\text{th}}$ bin of the $(p, E/p)$ distribution of one-prong tau decays.

ΔN_{ij}^π is the statistical uncertainty on N_{ij}^π , as obtained from the dE/dx likelihood fit.

B_l is the world average branching ratio of tau decay l , taken from reference [1].

ϵ_l is the efficiency for events from tau decay l in the tau-pair candidate sample to contribute to the one-prong tau decay sample.

S_{ij}^l is the probability, calculated using Monte Carlo generated events, for tau de-

cays of type l in the one-prong tau decay sample to contribute to the $(i, j)^{\text{th}}$ bin of the $(p, E/p)$ distribution.

\mathcal{S}_j^l is the correction to the j^{th} bin of the Monte Carlo E/p distribution of tau decays of type l , and is allowed to float in the fit.

s_i^l is a normalisation factor used to ensure that the correction to E/p does not affect the shape of the momentum distribution of decays of type l , and is determined from the condition $\sum_j s_i^l \mathcal{S}_{ij}^l \mathcal{S}_j^l = P_i^l$, where P_i^l is the probability, as calculated from Monte Carlo generated events, for tau decays of type l to contribute to the i^{th} bin of the momentum distribution.

Corrections to N_{clus}

Corrections, \mathcal{T} , to the Monte Carlo modelling of N_{clus} of $\tau^- \rightarrow \nu_\tau \pi^-$, $\tau^- \rightarrow \nu_\tau \pi^- \pi^0$, and $\tau^- \rightarrow \nu_\tau \pi^- \pi^0 \pi^0$ decays are obtained in a completely analogous fashion to the method used to obtain the E/p corrections. Again, the $\tau^- \rightarrow \nu_\tau \pi^-$, $\tau^- \rightarrow \nu_\tau \pi^- \pi^0$, and $\tau^- \rightarrow \nu_\tau \pi^- \pi^0 \pi^0$ N_{clus} distributions are quite similar to those of $\tau^- \rightarrow \nu_\tau K^-$, $\tau^- \rightarrow \nu_\tau K^- h^0$, and $\tau^- \rightarrow \nu_\tau K^- \geq 2h^0$ decays, respectively.

The linear correlation coefficients between N_{clus} and p , and N_{clus} and E/p are less than 20% in all classes of signal. Thus, the N_{clus} and the $(p, E/p)$ distributions are used as discriminators in this analysis, and N_{clus} is treated as a variable uncorrelated to both p and E/p .

7.3.2 The $\tau^- \rightarrow \nu_\tau K^-$ Branching Ratio

The $\tau^- \rightarrow \nu_\tau K^-$ branching ratio, B_{K^-} , is determined by a χ^2 fit to the $(p, E/P)$ and N_{clus} distributions of one-prong tau decays with a charged kaon, where the modelling of the distributions is corrected using the results of the previous section.

The following χ^2 is minimised:

$$\begin{aligned} \chi^2 &= \sum_j \sum_i \left[\frac{N_{ij}^K - N_{ij}^{\text{bkgnd}} - \sum_l \epsilon_l s_i^l S_{ij}^l G_j^l R}{\Delta N_{ij}^K} \right]^2 \\ &+ \sum_k \left[\frac{N_k^K - N_k^{\text{bkgnd}} - \sum_l \epsilon_l T_k^l H_k^l R}{\Delta N_k^K} \right]^2, \end{aligned} \quad (7.4)$$

where l is an index referring to either $\tau^- \rightarrow \nu_\tau K^-$, $\tau^- \rightarrow \nu_\tau K^- h^0$, or $\tau^- \rightarrow \nu_\tau K^- \geq 2h^0$, and the indices i , j , and k run over the p , E/p , and N_{clus} bins, respectively. The number of kaons within each bin from hadronic Z^0 decays is N^{bkgnd} , while ΔN^K is the statistical uncertainty on the number of kaons within each bin, N^K . Also,

$$\begin{aligned} R &= \frac{N_{\text{TOTAL}}^K}{f \epsilon_{K^-} + (1-f) \epsilon_{K^- \geq 2h^0}} \\ G_j^{K^-} &= S_j^{\tau^-} f \\ G_j^{K^- h^0} &= S_j^{\tau^- \pi^0} (1-f) \frac{B_{K^- h^0}}{B_{K^- h^0} + B_{K^- \geq 2h^0}} \\ G_j^{K^- \geq 2h^0} &= S_j^{\tau^- \pi^0 \pi^0} (1-f) \frac{B_{K^- \geq 2h^0}}{B_{K^- h^0} + B_{K^- \geq 2h^0}} \\ H_k^{K^-} &= T_k^{\tau^-} f \\ H_k^{K^- h^0} &= T_k^{\tau^- \pi^0} (1-f) \frac{B_{K^- h^0}}{B_{K^- h^0} + B_{K^- \geq 2h^0}} \\ H_k^{K^- \geq 2h^0} &= T_k^{\tau^- \pi^0 \pi^0} (1-f) \frac{B_{K^- \geq 2h^0}}{B_{K^- h^0} + B_{K^- \geq 2h^0}}. \end{aligned}$$

and

f is the ratio of the OPAL $\tau^- \rightarrow \nu_\tau K^-$ branching ratio to the OPAL $\tau^- \rightarrow \nu_\tau K^- \geq 0h^0$ inclusive branching ratio, and is allowed to float in the fit.

N_{TOTAL}^K is the total number of charged kaons in the one-prong tau decay sample, as determined in section 7.2.1.

ϵ_l is the efficiency for events from tau decay l in the tau-pair candidate sample to contribute to the one-prong tau decay sample. The $\epsilon_{K^-h^0}$, $\epsilon_{K^- \geq 2h^0}$, and $\epsilon_{K^- \geq 1h^0}$ efficiencies are calculated from the average of the relevant efficiencies appearing in Table 7.3, weighted by the associated world average branching ratios.

$B_{K^-h^0}$ and $B_{K^- \geq 2h^0}$ are the world average branching ratios for $\tau^- \rightarrow \nu_\tau K^- h^0$ and $\tau^- \rightarrow \nu_\tau K^- \geq 2h^0$ decays, respectively, derived from results presented in reference [1].

S_j^l is the probability, calculated using Monte Carlo generated events, for tau decays of type l in the one-prong tau sample to contribute to the $(i, j)^{\text{th}}$ bin of the $(p, E/p)$ distribution.

$\mathcal{S}_j^{\pi^-}$, $\mathcal{S}_j^{\pi^- \pi^0}$, and $\mathcal{S}_j^{\pi^- \pi^0 \pi^0}$ are the corrections to the j^{th} bin of the Monte Carlo E/p distribution of the various one-prong tau decays to pions, as determined from the χ^2 fit using Equation 7.3.

s_i^l is a normalisation factor used to ensure that the correction to E/p does not affect the shape of the momentum distribution of decays of type l .

T_k^l is the probability, calculated using Monte Carlo generated events, for tau decays of type l in the one-prong tau sample to contribute to the k^{th} bin of the N_{clus} distribution.

$\mathcal{T}_j^{\pi^-}$, $\mathcal{T}_j^{\pi^- \pi^0}$, and $\mathcal{T}_j^{\pi^- \pi^0 \pi^0}$ are the corrections to the k^{th} bin of the Monte Carlo N_{clus} distribution of the various one-prong tau decays to pions, as determined in the previous section.

The $\tau^- \rightarrow \nu_\tau K^-$ branching ratio derived from the result of the fit using Equation 7.4 is

$$\text{Br}(\tau^- \rightarrow \nu_\tau K^-) = 0.651 \pm 0.026 \pm 0.023\%.$$

where the first uncertainty is statistical and the second is systematic. A summary of the systematic uncertainties is shown in Table 7.2.

The statistical uncertainty in B_{K^-} due to the statistical uncertainty in the number of kaons within each bin of the $(p, E/p)$ and N_{clus} distributions is assessed by repeating the fit many times, each time varying the central value of the number of kaons within a particular bin, a bin at a time, by plus, then minus, one statistical sigma. The square root of half of the quadrature sum of the net variations produced in the branching ratio is taken as the statistical uncertainty.

The χ^2 per degree of freedom of the fit using Equation 7.4 is 62.9/50. Figure 7.4 shows the E/p and N_{clus} distributions of one-prong tau decays with a charged kaon, where the normalisation of the contributions to the predicted distribution comes from the OPAL $\tau^- \rightarrow \nu_\tau K^-$ and $\tau^- \rightarrow \nu_\tau K^- \geq 0h^0$ branching ratios. If the E/p and N_{clus} corrections are not applied, the χ^2 per degree of freedom from the fit is 79.4/50.

To check for undue variation that may be produced by the choice of binning used in the fit, the above procedure is repeated using various binning schemes. The RMS variation of the results returned by the different fits is less than the statistical uncertainty from the original fit.

7.3.3 dE/dx Systematic Error

The uncertainty in the N^K within each N_{clus} or $(p, E/p)$ bin due to uncertainty in the dE/dx correction factors is determined as in Section 7.2.1. The dE/dx uncertainties are highly correlated between the bins.

Thus the uncertainty in B_{K^-} due to the dE/dx systematic uncertainty in the number of kaons within each bin of the $(p, E/p)$ and N_{clus} distributions is assessed by repeating the fit many times, each time varying the the central value of the number of kaons within a particular bin, a bin at a time, by plus, then minus, one sigma of the dE/dx systematic uncertainty. The average of the absolute variations produced in the branching ratio is taken as the dE/dx systematic uncertainty in

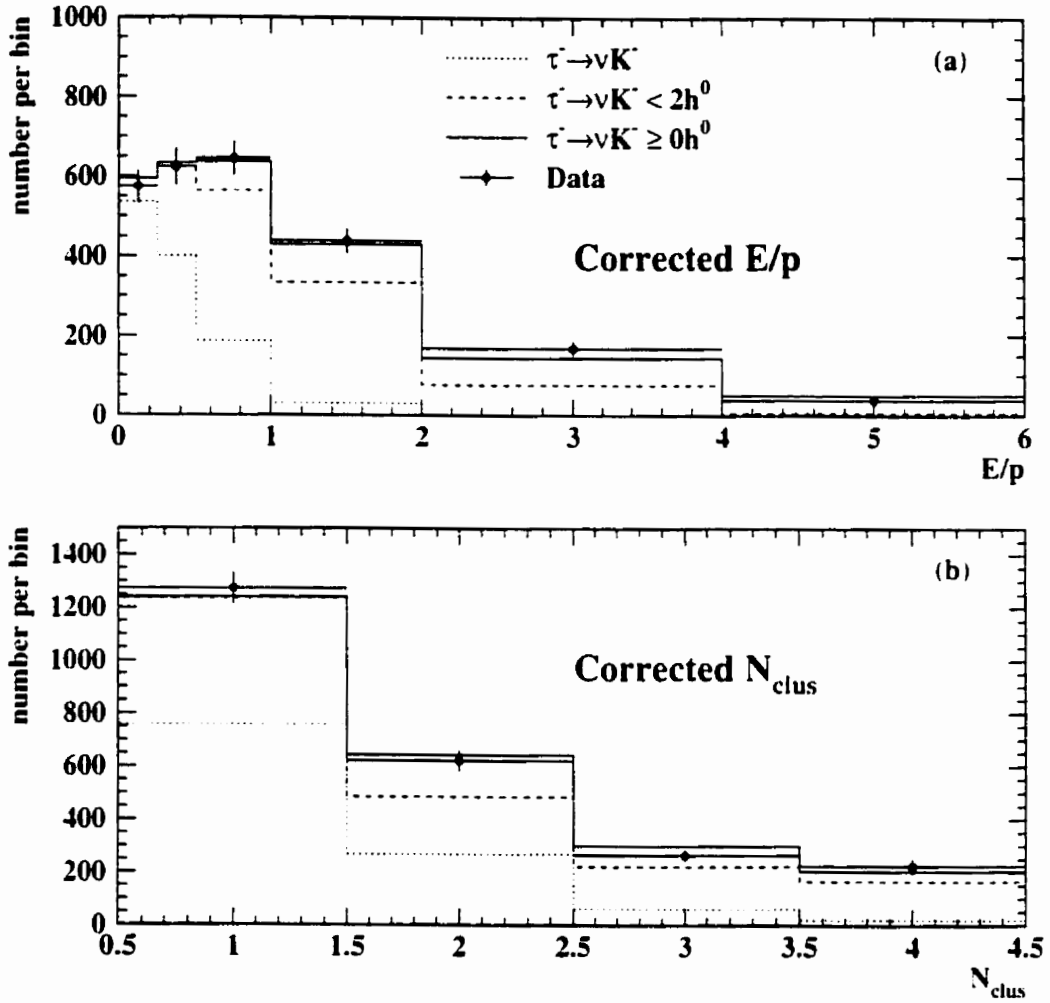


Figure 7.4: (a) and (b) are the corrected E/p and N_{clus} distributions, respectively, of Monte Carlo generated $\tau^- \rightarrow \nu_\tau K^- \geq 0h^0$ decays (histogram), along with the E/p and N_{clus} distributions of data one-prong tau decays with a charged kaon in the final state (points). The overall normalisation of Monte Carlo distributions is derived from the results of the dE/dx likelihood fit using Equation 7.1, while the normalisation of the $\tau^- \rightarrow \nu_\tau K^-$ component is obtained from the results of the χ^2 fit using Equation 7.4. Backgrounds are on the order of 0.4% or less and are neglected in this plot. The last bin in each of the distributions contains overflow events.

B_{K^-} , and is shown in Table 7.2.

7.3.4 Systematic Uncertainty Associated with the Efficiency Correction

The uncertainty in the $\tau^- \rightarrow \nu_\tau K^-$ branching ratio due to the limited Monte Carlo statistics used to determine the $\epsilon_{K^-h^0}$, $\epsilon_{K^-h^0}$, and $\epsilon_{K^- \geq 2h^0}$ efficiencies is assessed via the prior-belief method by modifying Equation 7.4 such that

$$\chi'^2 = \chi^2 + \left(\frac{\epsilon'_k - \epsilon_k}{\Delta\epsilon'_k} \right)^2,$$

where

ϵ'_k and $\Delta\epsilon'_k$ are the efficiency and associated uncertainty, due to limited Monte Carlo statistics, for kaons from signal channel k in the tau-pair candidate sample to enter the data sample.

ϵ_k is the efficiency used in the fit for kaons from signal channel k to contribute to the data sample.

In the first iteration of the fit the ϵ_k are allowed to float. In the second, they are fixed to the values from the first iteration. The square root of the quadrature difference in the errors in the branching ratio is taken as the systematic uncertainty associated with the limited Monte Carlo statistics used in the assessment of the efficiencies, and is shown in Table 7.2.

Various world average exclusive branching ratios are used in the calculation of $\epsilon_{K^-h^0}$ and $\epsilon_{K^- \geq 2h^0}$ (for instance, $\epsilon_{K^-h^0}$ is the average of $\epsilon_{K^- \pi^0}$ and $\epsilon_{K^- K^0}$, weighted by the world average branching ratios $B_{K^- \pi^0}$ and $B_{K^- K^0}$). In addition, these same branching ratios are used to assess the inclusive $\tau^- \rightarrow \nu_\tau K^- h^0$ and $\tau^- \rightarrow \nu_\tau K^- \geq 2h^0$ branching ratios appearing in Equation 7.4. The uncertainty in the $\tau^- \rightarrow \nu_\tau K^-$ branching ratio due to the uncertainties in these world average branching ratios

is again assessed using the prior-belief formalism by modifying Equation 7.4 such that

$$\chi^{2'} = \chi^2 + \left(\frac{B'_k - B_k}{\Delta B'_k} \right)^2.$$

where

B'_k and $\Delta B'_k$ are the world average branching ratio and associated uncertainty of tau decays to final state k .

B_k is the branching ratio to final state k used in the χ^2 fit.

The resulting systematic uncertainty in the $\tau^- \rightarrow \nu_\tau K^-$ branching ratio due to uncertainties in the world average branching ratios is shown in Table 7.2.

7.3.5 Systematic Uncertainty Associated with the Modelling of E/p and N_{clus}

The uncertainty in the $\tau^- \rightarrow \nu_\tau K^-$ branching ratio due to the statistical uncertainties in the E/p correction factors is assessed using the prior-belief method by modifying Equation 7.4 such that

$$\chi^{2'} = \chi^2 + (\mathbf{n}' - \mathbf{n})^T \mathbf{V}^{-1} (\mathbf{n}' - \mathbf{n}).$$

where

\mathbf{n}' is a vector containing the central values of the E/p corrections, as derived from the fit to the $\tau^- \rightarrow \nu_\tau \pi^- \leq 2\pi^0$ sample.

\mathbf{n} is a vector containing the values of the E/p corrections used in the χ^2 fit.

\mathbf{V} is the covariance matrix for the \mathcal{S} correction factors, as derived from the fit to the $\tau^- \rightarrow \nu_\tau \pi^- \leq 2\pi^0$ (p , E/p) and N_{clus} distributions.

In the first iteration, all bins of the three sets of \mathcal{S} corrections are allowed to vary in the fit, and the returned values are found to be consistent with the input values. In the second iteration, the fit is repeated, this time keeping the E/p corrections fixed to the values from the first iteration. The systematic uncertainty in B_{K^-} due to the modelling of E/p is then obtained from the square root of the quadrature difference of the fit uncertainties from the two iterations.

The uncertainty in the $\tau^- \rightarrow \nu_\tau K^-$ branching ratio due to the statistical uncertainties in the N_{clus} correction factors is assessed in a completely analogous fashion. The combined systematic uncertainty in B_{K^-} due to the corrections to the modelling of E/p and N_{clus} is shown in Table 7.2.

Chapter 8

Three-Prong Branching Ratios

Three-prong tau decay modes with charged kaons are dominated by the $\tau^- \rightarrow \nu_\tau K^- \pi^- \pi^+$ and $\tau^- \rightarrow \nu_\tau K^- \pi^- K^+$ decay modes. Theoretical predictions for the $\tau^- \rightarrow \nu_\tau K^- \pi^- \pi^+$ and $\tau^- \rightarrow \nu_\tau K^- \pi^- K^+$ branching ratios, as discussed in Chapter 2, are dependent on the assumptions made about the intermediate resonant structure inherent in these decays. Thus measurements of these branching ratios may possibly aid in distinguishing between the various models.

Measurement of the $\tau^- \rightarrow \nu_\tau K^- \pi^- \pi^+$ and $\tau^- \rightarrow \nu_\tau K^- \pi^- K^+$ branching ratios begins with the determination of the number of $\tau^- \rightarrow \nu_\tau K^- \pi^- \pi^+(\pi^0)$ and $\tau^- \rightarrow \nu_\tau K^- \pi^- K^+(\pi^0)$ decays in the tau-pair candidate sample, where the ‘ (π^0) ’ notation indicates that an extra π^0 may or may not be present. Information from the electromagnetic calorimeter is then used to distinguish between events with and without accompanying π^0 's, thus allowing the determination of the $\tau^- \rightarrow \nu_\tau K^- \pi^- \pi^+$ and $\tau^- \rightarrow \nu_\tau K^- \pi^- K^+$ branching ratios.

8.1 Event Selection

Event selection begins with tau-pair candidate selection described in Chapter 5. Both barrel and endcap events are used in this analysis to increase the statistics in the event samples. Endcap events are not used in the one-prong anal-

ysis because the larger backgrounds in the endcap tau pair events override any gains in precision that are added by the increased statistics. The precision of the three-prong analysis, however, benefits slightly from the addition of the endcap events.

The sum of the charges of the particles in each tau-pair candidate event is required to be equal to zero. Three-prong tau decay candidates are selected from the jets in this sample containing three well-reconstructed charged tracks. The sum of the charges of the three tracks is required to be equal to either +1 or -1. Decays with K_S^0 candidates are excluded by rejecting tau decay cones containing a secondary neutral vertex. The neutral vertex is defined as the intersection of a pair of oppositely charged tracks in the plane perpendicular to the beam direction, and is taken to be consistent with the decay of a K_S^0 if the $\pi^+\pi^-$ invariant mass of the two tracks in the vertex is between 400 and 600 MeV. This selection yields 38995 three-prong tau decay candidates.

8.1.1 Inclusive Candidate Samples (no π^0 Identification)

The ‘first-track’ sample is formed by selecting the track in each three-prong tau decay candidate that is closest to the anode plane. This track is also required to lie within $|\cos\theta| < 0.90$, and have at least 40 jet chamber hits used in the measurement of the dE/dx . All tracks in the first-track sample are also required to have reconstructed momentum between 3 and 90 GeV/c. Tracks in the barrel region of the OPAL detector ($|\cos\theta| < 0.72$) are required to have at least 3 hits in the z -chambers. In addition, tracks with projections in the $x-y$ plane that cross the $x-y$ projection of another track within the volume of the OPAL jet chamber are rejected from this sample. The ‘like-sign’ and ‘unlike-sign’ track samples are formed by selecting tracks in the first-track sample that have the same and opposite charge as that of the initial tau, respectively. The number of tracks in these two samples are 9296 and 4722, respectively.

In first-order weak decays of the tau only the $\tau^- \rightarrow \nu_\tau K^- \pi^- K^-(\pi^0)$ de-

cay modes contribute kaons to the unlike-sign sample, whereas both the $\tau^- \rightarrow \nu_\tau K^- \pi^- K^+(\pi^0)$ and $\tau^- \rightarrow \nu_\tau K^- \pi^- \pi^+(\pi^0)$ decay modes contribute kaons to the like-sign sample. Thus, after corrections for efficiencies and subtraction of background kaons, the numbers of kaons in these two samples are used to deduce the branching ratios to the $\tau^- \rightarrow \nu_\tau K^- \pi^- \pi^+(\pi^0)$ and $\tau^- \rightarrow \nu_\tau K^- \pi^- K^+(\pi^0)$ final states.

As a consistency check, we verify that the $\tau^- \rightarrow \nu_\tau \pi^- \pi^- K^+(\pi^0)$ final states are indeed suppressed. To do this, we form a sample depleted in $\tau^- \rightarrow \nu_\tau K^- \pi^- K^+(\pi^0)$ decays from the unlike-sign sample by requiring both associated like-sign tracks to have $S_\mp > -1.0$. The $K^- \pi^- K^+$ -enhanced sample is formed from tracks in the unlike-sign sample which do not satisfy this requirement. The number of tracks in these two samples is 1527 and 3195, respectively. The numbers of kaons in the $K^- \pi^- K^+$ -depleted sample, the $K^- \pi^- K^+$ -enhanced sample, and the like-sign sample are used to simultaneously determine the tau branching fractions to the $\nu_\tau K^- \pi^- \pi^+(\pi^0)$, $\nu_\tau K^- \pi^- K^+(\pi^0)$, and $\nu_\tau \pi^- \pi^- K^+(\pi^0)$ final states.

8.1.2 π^0 Identification

To determine the branching ratios for decays with and without π^0 's, we divide all the inclusive samples into separate π^0 -enhanced and π^0 -depleted samples using $E/\sum p > 0.5$ and $E/\sum p \leq 0.5$, respectively, where E is the total energy deposited in the electromagnetic calorimeter associated with the tau decay cone, and $\sum p$ is the scalar sum of the momenta of the charged particles in the decay. The $E/\sum p$ distributions for the Monte Carlo $\tau^- \rightarrow \nu_\tau K^- \pi^- \pi^+(\pi^0)$ and $\tau^- \rightarrow \nu_\tau K^- \pi^- K^+(\pi^0)$ samples are shown in Figure 8.1. The number of tracks in the $K^- \pi^- K^+$ -depleted, like-sign, and unlike-sign π^0 -depleted samples are 1110, 5984, and 3188, respectively.

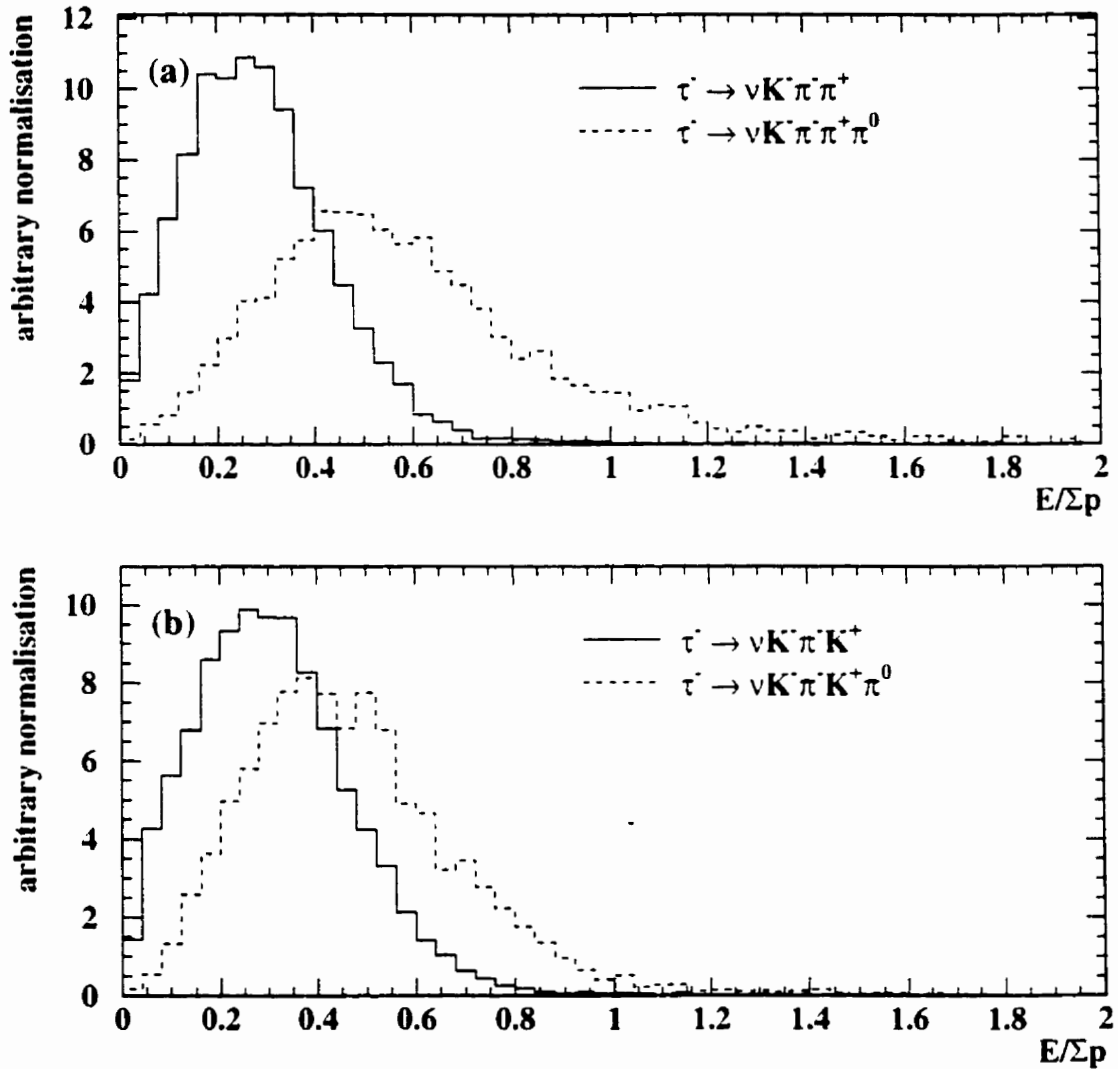


Figure 8.1: (a) shows the $E/\Sigma p$ distributions for Monte Carlo generated $\tau^- \rightarrow \nu_{\tau} K^- \pi^- \pi^+$ and $\tau^- \rightarrow \nu_{\tau} K^- \pi^- \pi^+ \pi^0$. (b) shows the same distributions for Monte Carlo generated $\tau^- \rightarrow \nu_{\tau} K^- \pi^- K^+$ and $\tau^- \rightarrow \nu_{\tau} K^- \pi^- K^+ \pi^0$.

8.2 Estimation of the Number of Kaons in the Samples

To determine the number of kaons in the data candidate samples described in Sections 8.1.1 and 8.1.2, we maximise a likelihood function based on dE/dx :

$$\mathcal{L} = \prod_{j=1..N} \sum_{i=e,\pi,K} f_i W^{ij}, \quad (8.1)$$

where W^{ij} is the dE/dx weight of charged particle j under particle hypothesis i ,

$$W^{ij} = \frac{1}{\sqrt{2\pi} s'(\beta_j) s_{res} \sigma_{ij}} \exp \left[-\frac{1}{2} \left(\frac{D_{meas}^j - f(\phi_j) - s'(\beta_j) D_{pred}^{ij}}{s'(\beta_j) s_{res} \sigma_{ij}} \right)^2 \right], \quad (8.2)$$

and where

f_i is the fraction of particle type i in the sample, where i is either pion, kaon, or electron. The values of f_i are constrained to be non-negative, and the sum is constrained to be 1.

N is the total number of particles in the sample.

D_{meas}^j is the measured dE/dx of the j^{th} charged particle.

D_{pred}^{ij} is the predicted dE/dx for charged particle j , calculated with the OPAL parameterisation under particle hypothesis i , as derived from the measured dE/dx of charged particles in hadronic Z^0 events.

σ_{ij} is the uncertainty on D_{pred}^{ij} , calculated using the OPAL parameterisation, as derived from hadronic Z^0 events.

s_{res} is the multiplicative correction to σ_{ij} for all particle hypotheses i , and is allowed to vary without constraint in each fit. Separate s_{res} factors are used for charged particles in the barrel and endcap regions of the OPAL detector. The central values of these parameters are about 0.84 and 0.73, respectively.

$s'(\beta)$ is the β dependent multiplicative correction to D_{pred} , and is equal to $s(\beta)+\alpha$, where $s(\beta)$ is determined from the one-prong control samples, and α is a correction allowed to vary in each fit to compensate for possible slight differences between the dE/dx of the one-prong and three-prong decay environments. Separate $s'(\beta)$ factors are needed for charged particles from three-prong tau decays in the barrel and endcap regions of the OPAL detector. These extra constant terms yield a correction to the dE/dx of approximately 1%.

$f(o)$ is the o dependent correction to the measured dE/dx , as obtained from the one-prong control samples.

To account for possible species-dependent quality differences in the parameterisation of dE/dx , an extra factor, C_k , derived from dE/dx of the one-prong tau decay sample, as described in the previous chapter, is allowed to multiply the kaon predicted energy loss, D_{pred}^k , in the likelihood function found in Equation 8.1.

Independent likelihood fits are performed for different ranges of momentum (13 bins of variable size between 3 and 90 GeV/c). A test of the fit with large Monte Carlo samples verifies that the resulting estimates for the kaon fraction have biases within the range $-0.5\sigma_{f_k}$ to $0.3\sigma_{f_k}$ at the 95% confidence level, where σ_{f_k} is the typical statistical uncertainty on the kaon fraction returned by the fit. Thus, biases resulting from the fit procedure are neglected.

The number of kaons found within each of the samples is given in Table 8.1, and the stretch dE/dx distributions of tracks in all momentum bins of the inclusive data like-sign and unlike-sign samples are shown in Figure 8.2. The normalisation of the predicted distributions of the kaons, pions, and electrons in each sample is obtained from the results of the likelihood fits. The χ^2 per degree of freedom between the first 11 bins of the data and predicted distributions, which is the portion of the dE/dx distribution populated by kaons, is 15.9/10 and 10.6/7 for the like-sign and unlike-sign samples, respectively.

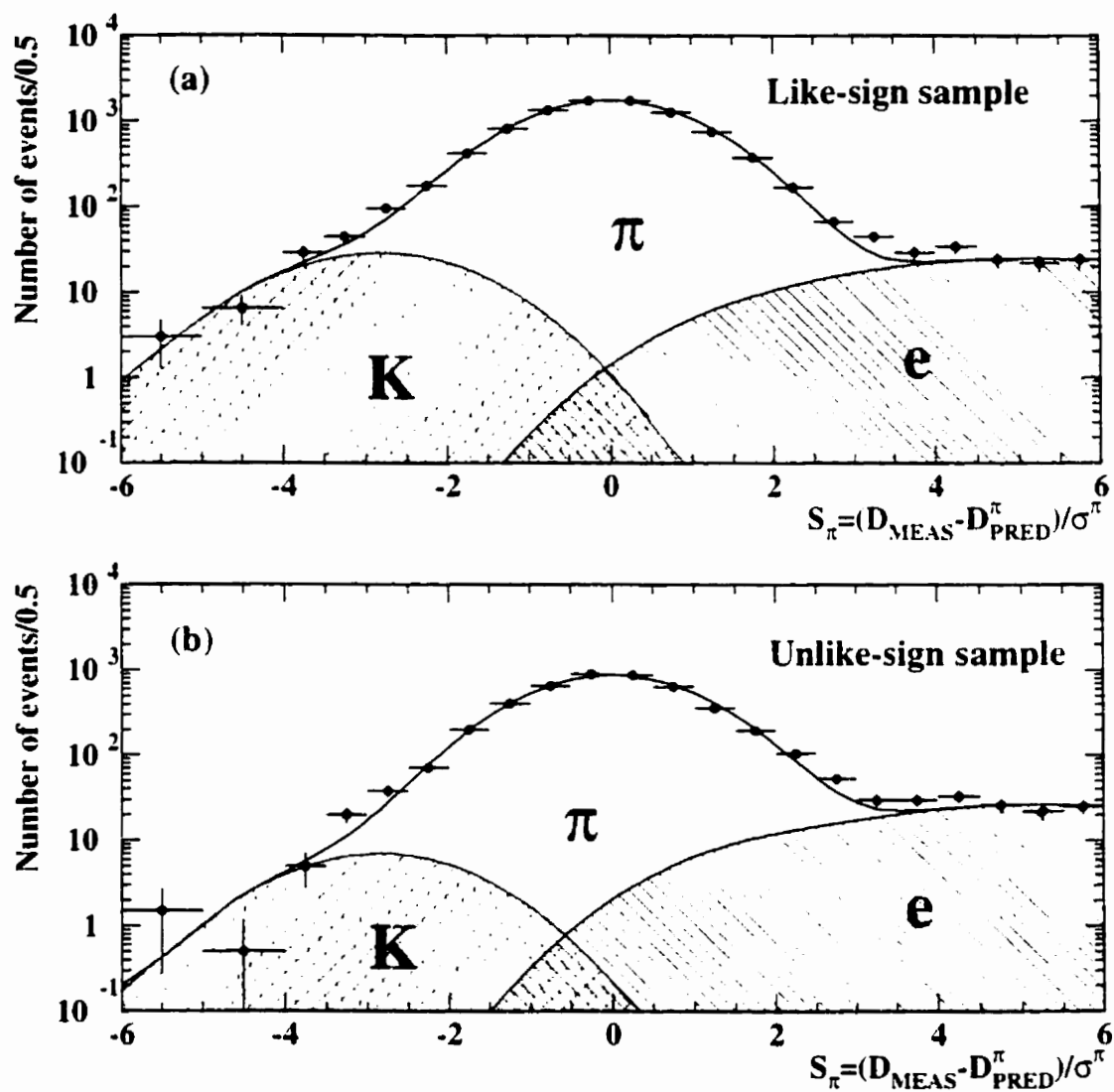


Figure 8.2: (a) shows the stretch dE/dx distribution of tracks in the data inclusive like-sign sample (points). The overlaid curves are the predicted distributions for the kaons, pions and electrons in the sample, assuming a Gaussian resolution function for the dE/dx measurements. The normalisation of the curves comes from the results of the likelihood fit. (b) shows the same distribution for tracks in the data inclusive unlike-sign sample.

8.3 The Branching Ratio Calculation

The branching ratios in the tau decay channels of interest are calculated from the numbers of kaons, as estimated by the likelihood fit, in the 13 momentum bins of the exclusive candidate samples, listed in Table 8.1. The number of kaons within each momentum bin i of candidate sample j is corrected for background, yielding

$$R_{ij} = \frac{(\mathcal{N}_{ij}^K - \mathcal{N}_{ij}^{\text{bkgnd}})}{\mathcal{N}_\tau(1 - f^{\text{non-}\tau})}$$

where

\mathcal{N}_τ is the number of tau decay candidates. There were 295852 tau decay candidates recorded in the OPAL detector between the years 1990 and 1995.

$f^{\text{non-}\tau}$ is the estimated background from non- τ sources in the tau decay candidates ($f^{\text{non-}\tau} = 2.73 \pm 0.27\%$).

\mathcal{N}_{ij}^K is the number of kaons in momentum bin i of candidate sample j , as estimated by the likelihood fit. The number of kaons summed over all momentum bins of each sample is shown in Table 8.1.

$\mathcal{N}_{ij}^{\text{bkgnd}}$ is the estimated number of background kaons in momentum bin i of candidate sample j , as estimated from Monte Carlo tau decay and hadronic Z^0 decay samples. The number of background kaons summed over all momentum bins of each sample is shown in Table 8.1.

A set of linear equations that relate the R_{ij} to the tau branching ratios are solved simultaneously to determine the branching ratios. The set of equations includes efficiency corrections as a function of momentum for each decay channel, as determined from Monte Carlo generated events, as described in Section 8.4. The efficiency correction does not assume that the momentum distribution of the signal kaons in each sample follows those of kaons from the Monte Carlo. For background

corrections, however, the momentum distributions of Monte Carlo generated events are used.

In the first step of the branching ratio calculation, the $\tau^- \rightarrow \nu_\tau \pi^- \pi^- K^+(\pi^0)$ branching ratios are not assumed to be zero. The branching ratio calculation uses the division of the unlike-sign samples into the $K^- \pi^- K^-$ -enhanced and $K^- \pi^- K^+$ -depleted samples in conjunction with the like-sign samples, for a total of six exclusive samples, as listed in Table 8.1. The results of the calculation are:

$$\begin{aligned}
 \text{Br}(\tau^- \rightarrow \nu_\tau K^- \pi^- \pi^+(\pi^0)) &= +0.404 \pm 0.083 \% \\
 \text{Br}(\tau^- \rightarrow \nu_\tau K^- \pi^- K^-(\pi^0)) &= +0.066 \pm 0.079 \% \\
 \text{Br}(\tau^- \rightarrow \nu_\tau \pi^- \pi^- K^-(\pi^0)) &= +0.077 \pm 0.070 \% \\
 \text{Br}(\tau^- \rightarrow \nu_\tau K^- \pi^- \pi^- \pi^0) &= +0.064 \pm 0.086 \% \\
 \text{Br}(\tau^- \rightarrow \nu_\tau K^- \pi^- K^+ \pi^0) &= -0.110 \pm 0.128 \% \\
 \text{Br}(\tau^- \rightarrow \nu_\tau \pi^- \pi^- K^+ \pi^0) &= +0.137 \pm 0.109 \% \\
 \text{Br}(\tau^- \rightarrow \nu_\tau K^- \pi^- \pi^-) &= +0.340 \pm 0.086 \% \\
 \text{Br}(\tau^- \rightarrow \nu_\tau K^- \pi^- K^-) &= +0.176 \pm 0.078 \% \\
 \text{Br}(\tau^- \rightarrow \nu_\tau \pi^- \pi^- K^+) &= -0.060 \pm 0.068 \%.
 \end{aligned}$$

where the uncertainties are statistical only, and where the inclusive branching ratios are obtained from the sums of the exclusive branching ratios. Correlations between the exclusive branching ratios are taken into account in this calculation. The results for the branching ratios to the $\nu_\tau \pi^- \pi^- K^+(\pi^0)$ final states, which can only occur as second-order weak interactions, are consistent with zero, as expected, indicating that there are no significant biases in the kaon identification procedure.

To obtain more precise branching ratios for the first-order weak decays, we set the $\tau^- \rightarrow \nu_\tau \pi^- \pi^- K^+(\pi^0)$ branching ratios to zero and repeat the calculation. In this iteration, the calculation uses the unlike-sign and like-sign exclusive samples.

for a total of four samples. The results of this calculation are:

$$\text{Br}(\tau^- \rightarrow \nu_\tau \text{K}^- \pi^- \pi^+(\pi^0)) = +0.343 \pm 0.073 \pm 0.031 \%$$

$$\text{Br}(\tau^- \rightarrow \nu_\tau \text{K}^- \pi^- \text{K}^+(\pi^0)) = +0.159 \pm 0.053 \pm 0.020 \%$$

$$\text{Br}(\tau^- \rightarrow \nu_\tau \text{K}^- \pi^- \pi^+ \pi^0) = -0.017 \pm 0.076 \pm 0.060 \%$$

$$\text{Br}(\tau^- \rightarrow \nu_\tau \text{K}^- \pi^- \text{K}^+ \pi^0) = +0.072 \pm 0.085 \pm 0.051 \%$$

$$\text{Br}(\tau^- \rightarrow \nu_\tau \text{K}^- \pi^- \pi^+) = +0.360 \pm 0.082 \pm 0.048 \%$$

$$\text{Br}(\tau^- \rightarrow \nu_\tau \text{K}^- \pi^- \text{K}^-) = +0.087 \pm 0.056 \pm 0.040 \%$$

where the first uncertainties are statistical and the second are systematic. The summary of the systematic uncertainties for each branching ratio is shown in Table 8.2. The correlation matrix for the exclusive branching ratios is found in Table 8.3.

The $\tau^- \rightarrow \nu_\tau \text{K}^- \pi^- \pi^-(\pi^0)$ branching ratios from the first and second calculations are approximately 70% correlated, and the $\tau^- \rightarrow \nu_\tau \text{K}^- \pi^- \text{K}^-(\pi^0)$ branching ratios from the first and second calculations are approximately 50% correlated. In both cases, the resulting differences in the branching ratios between the two iterations are consistent to within 1.3σ of the combined statistical uncertainties.

The central values of the branching ratios are evaluated using an $E/\Sigma p$ selection of 0.5 to distinguish between states including and not including a π^0 . The branching ratios are also evaluated using $E/\Sigma p$ selections of 0.3, 0.4, 0.6, and 0.7. The branching ratio systematic uncertainty associated with the $E/\Sigma p$ selection is taken as the RMS spread of the five values, and is quoted in Table 8.2.

8.4 dE/dx Systematic Studies

A significant source of systematic uncertainty in this measurement is the uncertainty in the parameterisation of the predicted energy loss. To assess this sys-

	π^0 -depleted Sample				π^0 -enhanced Sample			
	like-sign		unlike-sign		like-sign		unlike-sign	
	$K^- \pi^- K^+$ enhanced	$K^- \pi^- K^+$ depleted	$K^- \pi^- K^+$ enhanced	$K^- \pi^- K^+$ depleted	$K^- \pi^- K^+$ enhanced	$K^- \pi^- K^+$ depleted	$K^- \pi^- K^+$ enhanced	$K^- \pi^- K^+$ depleted
N_{TOTAL}	$128.4 \pm 16.5 \pm 2.3$	$1.4 \pm 3.7 \pm 0.5$	$36.7 \pm 9.5 \pm 1.2$	$1.4 \pm 3.7 \pm 0.5$	$29.5 \pm 9.2 \pm 1.1$	$4.6 \pm 3.7 \pm 0.3$	$5.9 \pm 5.6 \pm 0.6$	$4.6 \pm 3.7 \pm 0.3$
N_{bkgnd}	5.8 ± 1.8	0	0	0	8.5 ± 2.1	0	2.5 ± 1.5	0
$\epsilon_{K^- \pi^- \pi^+}$	0.094 ± 0.003	< 0.001	< 0.001	< 0.001	0.013 ± 0.001	< 0.001	< 0.001	< 0.001
$\epsilon_{K^- \pi^- K^+}$	0.078 ± 0.003	0.104 ± 0.003	0.104 ± 0.003	0.003 ± 0.001	0.007 ± 0.001	0.008 ± 0.001	0.008 ± 0.001	< 0.001
$\epsilon_{\pi^+ \pi^- K^+}$	< 0.001	0.065 ± 0.006	0.065 ± 0.006	0.029 ± 0.002	< 0.001	0.008 ± 0.001	0.008 ± 0.001	0.005 ± 0.001
$\epsilon_{K^- \pi^- \pi^+ \pi^0}$	0.044 ± 0.002	< 0.001	< 0.001	< 0.001	0.047 ± 0.002	< 0.001	< 0.001	< 0.001
$\epsilon_{K^- \pi^- K^+ \pi^0}$	0.048 ± 0.003	0.053 ± 0.003	0.053 ± 0.003	0.001 ± 0.001	0.030 ± 0.002	0.032 ± 0.002	0.032 ± 0.002	< 0.001
$\epsilon_{\pi^+ \pi^- K^+ \pi^0}$	< 0.001	0.033 ± 0.002	0.033 ± 0.002	0.012 ± 0.001	< 0.001	0.036 ± 0.001	0.036 ± 0.001	0.011 ± 0.001

Table 8.1: The number of kaons in each data sample, N_K , where the first uncertainty is the statistical uncertainty from the maximum likelihood fit to the measured dE/dx of the tracks in the sample, and the second is the systematic uncertainty arising from the uncertainties in the parameterisation of dE/dx . Also shown are the estimated backgrounds and the average efficiencies for the various signal channels which contribute to each sample.

	Branching Ratios (%)					
	$B_{K^- \pi^+ \pi^0}$	$B_{K^- \pi^+ \pi^0}$	$B_{K^- \pi^+ \pi^0}$	$B_{K^- \pi^+ \pi^0}$	$B_{K^- \pi^+ \pi^0}$	$B_{K^- \pi^+ \pi^0}$
Central value	0.343	0.159	-0.017	0.072	0.360	0.087
σ (stat)	± 0.073	± 0.053	± 0.076	± 0.085	± 0.082	± 0.056
σ (dE/dx sys)	± 0.017	± 0.010	± 0.020	± 0.015	± 0.013	± 0.016
σ (MC stat)	± 0.023	± 0.012	± 0.029	± 0.018	± 0.029	± 0.018
σ (E/ Σp sys)	± 0.012	± 0.012	± 0.049	± 0.045	± 0.036	± 0.032

Table 8.2: Summary of the branching ratio central values and sources of uncertainty.

	$B_{K^-\pi^-\pi^+}$	$B_{K^-\pi^-K^+}$	$B_{K^-\pi^-\pi^+\pi^0}$	$B_{K^-\pi^-K^+\pi^0}$
$B_{K^-\pi^-\pi^+}$	+1.0	-0.3	-0.6	+0.1
$B_{K^-\pi^-K^+}$	-0.3	+1.0	+0.4	-0.8
$B_{K^-\pi^-\pi^+\pi^0}$	-0.6	+0.3	+1.0	-0.5
$B_{K^-\pi^-K^+\pi^0}$	+0.1	-0.8	-0.5	+1.0

Table 8.3: Correlations between the exclusive branching ratios.

tematic, we determine the sensitivity of the likelihood estimates of the number of kaons within each of the data samples to the uncertainties in the dE/dx correction factors obtained from the one-prong samples. The likelihood function shown in Equation 8.1 is therefore modified such that:

$$\mathcal{L}' = \exp\left(-\frac{1}{2}(\mathbf{n}' - \mathbf{n})^T \mathbf{V}^{-1}(\mathbf{n}' - \mathbf{n})\right) \mathcal{L},$$

where

\mathbf{n}' is a vector containing the central values of the seven dE/dx correction factors that describe the function $f(\phi)$, and the three correction factors that describe the function $s(\beta)$, where the central values are as derived from the fits to the one-prong control samples.

\mathbf{n} is a vector containing the dE/dx correction factors used in the likelihood fit.

\mathbf{V} is the covariance matrix for the dE/dx correction factors, as derived from the fits to the one-prong control samples.

In the first iteration, the correction factors are allowed to vary in the fit, and the returned values are found to be consistent with the input values. In the second iteration, the likelihood fit is repeated, this time keeping the dE/dx correction factors fixed to the values from the first iteration. The systematic uncertainty in N_{TOTAL}^K due to the parameterisation of dE/dx is then obtained from the square root of the quadrature difference of the fit uncertainties in N_{TOTAL}^K from the two iterations, and is shown in Table 8.1.

8.5 Efficiency Correction

The efficiencies for kaons from signal events in the tau-pair candidate sample to enter the candidate samples are estimated using signal events generated with the KORALZ 4.0 Monte Carlo generator and the Tauola 2.4 decay package, as described in Chapter 6.

Table 8.1 shows the average efficiency estimates for the various signal channels in the tau decay sample that contribute kaons to the data samples described in Sections 8.1.1 and 8.1.2. All efficiencies are corrected for biases introduced by the tau-pair selection using a Monte Carlo tau-pair sample, and the efficiency uncertainties include the systematic uncertainty arising from this correction. The selection bias factors are described in Chapter 5 and are shown in Table 5.2.

Figure 8.3 shows the efficiency versus momentum for $\tau^- \rightarrow \nu_\tau K^- \pi^- \pi^-$ and $\tau^- \rightarrow \nu_\tau K^- \pi^- K^+$ in the tau-pair candidate sample to contribute kaons to the inclusive like-sign and unlike-sign samples, respectively. The branching ratio analysis is performed using an efficiency correction that is binned in momentum.

The variation of the branching ratios due to alternative intermediate resonant structure scenarios for the $\tau^- \rightarrow \nu_\tau K^- \pi^- \pi^-$ final state is assessed using efficiency estimates from signal events generated by the modified version of Tauola 2.4 through the $K_1(1270)$ and $K_1(1400)$ intermediate states as described in Chapter 6. The mixture of $K_1(1270)$ and $K_1(1400)$ is taken from the results of the analysis of the intermediate resonant structure of $\tau^- \rightarrow \nu_\tau K^- \pi^- \pi^+$ candidates, as described in Chapter 9. $R = \text{Br}(\tau^- \rightarrow \nu_\tau K_1(1270)) / \text{Br}(\tau^- \rightarrow \nu_\tau (K_1(1400) \text{ or } K_1(1270))) = 0.71 \pm 0.19$. The branching ratios obtained within this range are found to be in agreement with the central values to within 1.5σ of the combined Monte Carlo statistical uncertainty.

As a further cross-check, the branching ratios are evaluated using $\tau^- \rightarrow \nu_\tau K^- \pi^- \pi^+$ and $\tau^- \rightarrow \nu_\tau K^- \pi^- K^+$ efficiencies estimated using Monte Carlo events generated through non-resonant production only. The resulting branching

ratios are in agreement with the branching ratio central values to within 1σ of the combined Monte Carlo statistical uncertainty.

8.6 Kaon Background Correction

Background kaons in the data samples described in Sections 8.1.1 and 8.1.2 are estimated by applying the same selection criteria to Monte Carlo samples of hadronic Z^0 decays and tau-pair decays. From the number of selected events that contain kaons, the estimated number of background kaons are derived, as summarised in Table 8.1. Dominant sources of background kaons include low-multiplicity hadronic Z^0 events, and $\tau^- \rightarrow \nu_\tau K^- \geq 0$ neutrals decays.

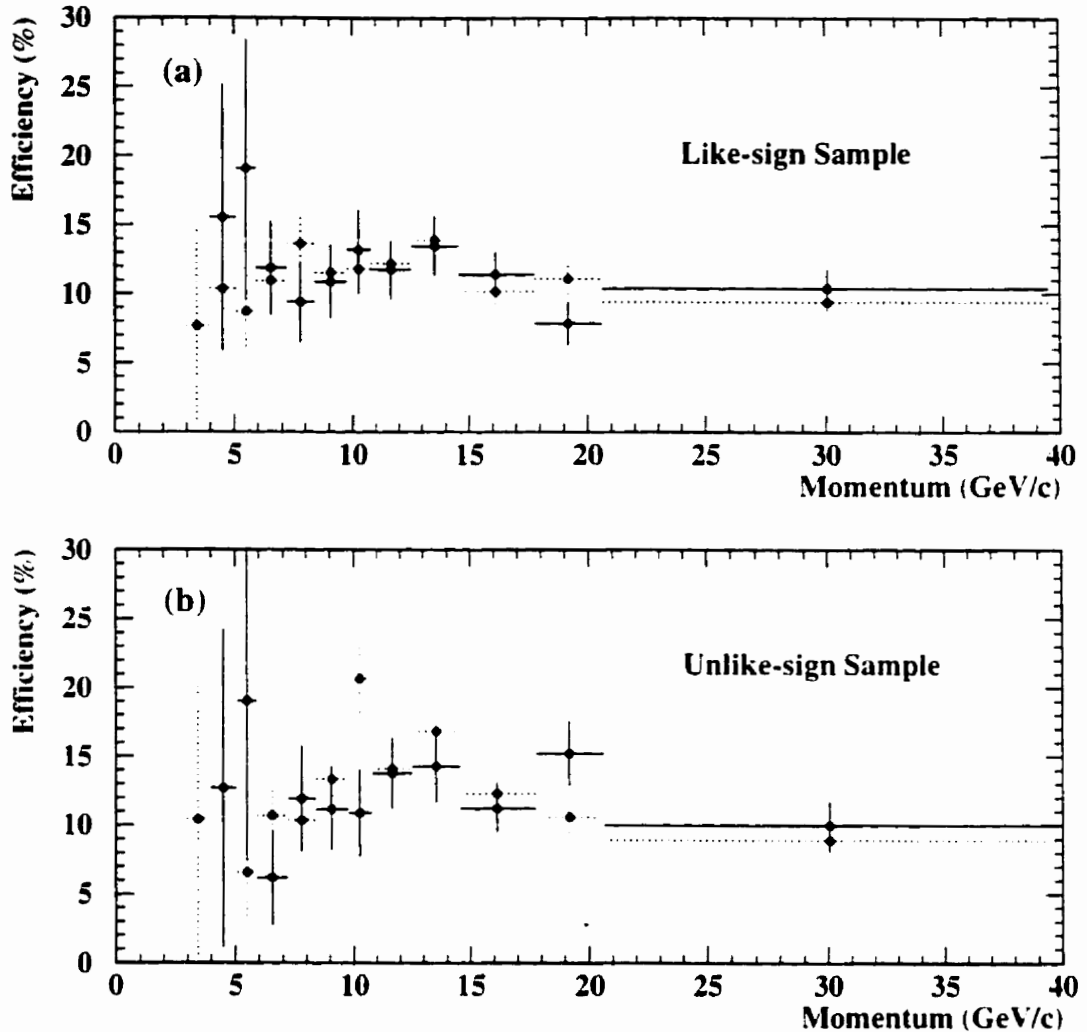


Figure 8.3: (a) shows the efficiency as a function of kaon momentum for $\tau^- \rightarrow \nu_\tau K^- \pi^- \pi^+$ in the tau-pair candidate sample to contribute kaons to the like-sign sample: the solid points represent the default Tauola 2.4 generation of $\tau^- \rightarrow \nu_\tau K^- \pi^- \pi^+$ and the dotted points are calculated using $\tau^- \rightarrow \nu_\tau K^- \pi^- \pi^+$ generated through phase space only. (b) shows the efficiency versus kaon momentum for $\tau^- \rightarrow \nu_\tau K^- \pi^- K^+$ in the tau-pair candidate sample to contribute kaons to the unlike-sign sample; the solid points represent the default Tauola 2.4 generation of $\tau^- \rightarrow \nu_\tau K^- \pi^- K^+$ and the dotted points are calculated using $\tau^- \rightarrow \nu_\tau K^- \pi^- K^+$ generated through phase space only. The branching ratio central values are calculated using $\tau^- \rightarrow \nu_\tau K^- \pi^- \pi^+$ and $\tau^- \rightarrow \nu_\tau K^- \pi^- K^+$ efficiencies estimated with the default version of Tauola 2.4.

Chapter 9

Three-Prong Resonant Structure

As mentioned in Chapter 2, current theoretical models and experimental evidence indicate that the resonant structure of the $\tau^- \rightarrow \nu_\tau K^- \pi^- \pi^+$ decay mode is dominated by the $K_1(1400)$ and $K_1(1270)$ decay modes. To test this prediction, the good charged particle identification capabilities of the OPAL detector are exploited to study the invariant mass distributions of events identified, using dE/dx , as $\tau^- \rightarrow \nu_\tau K^- \pi^- \pi^+$ candidates. The prediction of reference [38] that the widths of the $K_1(1400)$ and $K_1(1270)$ resonances may actually be larger than the widths given in reference [1] is also explored in these studies. In addition, other possible, non- K_1 , resonant modes are also compared to the resonant structure seen in the data.

Unfortunately, the phase-space suppression of the $\tau^- \rightarrow \nu_\tau K^- \pi^- K^+$ decay mode results in a dearth of candidates in that channel at OPAL, making precision studies of the resonant structure of that mode difficult. The studies presented here are thus limited to comparing the resonant structure seen in $\tau^- \rightarrow \nu_\tau K^- \pi^- K^+$ candidates with that predicted by three different models.

9.1 Event Selection

The selection of events used in the study of the resonant structure begins with the three-prong tau decay candidate sample described in Chapter 8. Events which include an e^+e^- pair from a photon converting in the detector material are identified and rejected on the basis of a topological conversion finder [57]. All three tracks in each decay are required to have at least 40 jet chamber hits used in the measurement of dE/dx . Tracks in the barrel region of the OPAL detector are required to have at least 3 hits in the z -chambers.

Using $S_\pi < -2.0$ to identify kaons, and $|S_\pi| < 1.5$ to identify pions, events are classified into the following channels:

- $\tau^- \rightarrow \nu_\tau K^- \pi^- \pi^+$ candidates have one like-sign kaon, and an unlike-sign and like-sign pion.
- $\tau^- \rightarrow \nu_\tau K^- \pi^- K^+$ candidates have one like-sign pion, and an unlike-sign and like-sign kaon.
- $\tau^- \rightarrow \nu_\tau \pi^- \pi^- \pi^+ (\pi^0)$ candidates have all three tracks identified as pions.

The number of kaons in the lowest momentum bin of the candidate samples used in the branching ratio analysis is found to be consistent with zero. Thus, to increase the signal to noise ratio in the samples used in the resonant studies, all kaon candidates are required to have momentum of at least 5 GeV/c. Pion candidates are required to have momentum of at least 0.75 GeV/c. The above selections produce 950 $\tau^- \rightarrow \nu_\tau K^- \pi^- \pi^+$ and 79 $\tau^- \rightarrow \nu_\tau K^- \pi^- K^+$ candidates.

The non-Gaussian tails in the data dE/dx distribution are not as problematic in this portion of the analysis as they are in the branching ratio analysis (and thus no attempt is made to remove them). This is because the differing shapes of the signal and the $\tau^- \rightarrow \nu_\tau \pi^- \pi^- \pi^+ (\pi^0)$ invariant mass distributions provide some separation power between signal and background in the data samples, and the dE/dx selections used to identify pions and kaons in this study are loose selections only.

designed to provide three-prong tau decay samples enhanced with $\tau^- \rightarrow \nu_\tau K^- \pi^- \pi^+$ or $\tau^- \rightarrow \nu_\tau K^- \pi^- K^+$ decays. Other than these initial selections, dE/dx is not used to distinguish between signal and background.

9.2 $\tau^- \rightarrow \nu_\tau K^- \pi^- \pi^+$

The background in the $\tau^- \rightarrow \nu_\tau K^- \pi^- \pi^+$ event sample consists primarily of $\tau^- \rightarrow \nu_\tau \pi^- \pi^- \pi^+ (\pi^0)$ events, along with small contributions from $\tau^- \rightarrow \nu_\tau K^- \pi^- \pi^- \pi^0$, other tau decays, and hadronic Z^0 events.

To analyse the resonant structure of these decays, we examine the $M_{K^- \pi^- \pi^+}$, $M_{K^- \pi^+}$, and $M_{\pi^- \pi^+}$ invariant mass distributions of the candidates, shown in Figure 9.1. To estimate the shape of the dominant three-pion background in these distributions, we use the $\tau^- \rightarrow \nu_\tau \pi^- \pi^- \pi^+ (\pi^0)$ candidate sample, with the 5 GeV/c momentum selection placed on the particle which corresponds to the like-sign kaon candidate. This selection produces a sample of about 16000 events. To ensure that the dE/dx cuts used in selection of pion and kaon candidates do not bias the momentum distribution of this control sample, a sample of $\tau^- \rightarrow \nu_\tau \pi^- \pi^- K^-$ candidates is selected in a completely analogous fashion to the $\tau^- \rightarrow \nu_\tau K^- \pi^- \pi^+$ candidate sample. Because $\tau^- \rightarrow \nu_\tau \pi^- \pi^- K^-$ decays are highly suppressed due to the strangeness constraints in tau decays, this sample is expected to be entirely $\tau^- \rightarrow \nu_\tau \pi^- \pi^- \pi^+ \geq 1\pi^0$ background. Figure 9.2 compares the invariant mass and $\sum p$ distributions of this sample to those of the $\tau^- \rightarrow \nu_\tau \pi^- \pi^- \pi^+ \geq 1\pi^0$ control sample. No bias is evident.

The shape of the $\tau^- \rightarrow \nu_\tau K^- \pi^- \pi^+ \pi^0$ background in the distributions is parameterised with Monte Carlo $\tau^- \rightarrow \nu_\tau K^- \pi^- \pi^+ \pi^0$ events generated through non-resonant production. Other background fractions are expected to be on the order of a percent or less and are neglected.

The description of the shape of the signal portion of these invariant mass distributions depends upon assumptions made about the intermediate resonant

structure of $\tau^- \rightarrow \nu_\tau K^- \pi^- \pi^+$ decays. We consider four different scenarios:

1. The $\tau^- \rightarrow \nu_\tau K^- \pi^- \pi^+$ decays occur through a mixture of $K_1(1270)$ and $K_1(1400)$. For this study we assume that the $K_1(1270)$ has a width of 90 MeV, and the $K_1(1400)$ has a width of 174 MeV, the current world average widths of these resonances [1].
2. The $\tau^- \rightarrow \nu_\tau K^- \pi^- \pi^+$ decays occur through the $K_1(1270)$ and $K_1(1400)$ resonances, and that the widths of these resonances are both 300 MeV [37].
3. The $\tau^- \rightarrow \nu_\tau K^- \pi^- \pi^+$ decays occur through a mixture of $K^*(892)\pi^-$ and $\rho(770)K^-$.
4. The $\tau^- \rightarrow \nu_\tau K^- \pi^- \pi^+$ decays occur through non-resonant production (phase space) only.

Monte Carlo samples having at least 10 times the statistics of the expected signal component of the data $\tau^- \rightarrow \nu_\tau K^- \pi^- \pi^+$ candidates are generated with a modified version of Tauola 2.4 under each of these resonant structure assumptions.

To estimate the background and signal fractions in a way that accounts for correlations between the invariant mass distributions, we divide the $M_{K-\pi-\pi^+}$, $M_{K-\pi^-}$, and $M_{\pi^-\pi^+}$ invariant masses of the data, signal Monte Carlo sets, and background samples into $\bar{\tau}$ bins each, to form a $\bar{\tau} \times \bar{\tau} \times \bar{\tau}$ matrix. Further discrimination between signal and background is obtained by dividing the scalar sum of the momenta in each three-prong decay into 24 bins between 0 and 48 GeV/c. The correlations between $\sum p$ and the invariant masses are not significant compared to the inter-correlations between the invariant masses.

Using the various simulated signal and background distributions as templates, a binned maximum likelihood fit is performed simultaneously to the data $\bar{\tau} \times \bar{\tau} \times \bar{\tau}$ matrix and the $\sum P$ distribution to determine the most probable fractions of signal and $\tau^- \rightarrow \nu_\tau K^- \pi^- \pi^+ \pi^0$ background in the $\tau^- \rightarrow \nu_\tau K^- \pi^- \pi^+$ candidates. For the first three scenarios, two signal fractions are allowed to float. Bins in the matrix and

ΣP distribution which contain data events but no predicted signal or background events are neglected in the fit ¹. A test of the procedure using a Monte Carlo event sample of the same size and approximate composition of the data sample reveals no significant bias in the estimates of the signal and background fractions from the fit.

The results of the fits are shown in Table 9.1. Table 9.1 also gives the χ^2 per degree of freedom between the data and predicted ΣP , $M_{K^-\pi^-\pi^+}$, $M_{K^-\pi^+}$, and $M_{\pi^-\pi^+}$ distributions, where the normalisation of the predicted distributions is obtained from the fit results. The binning of these distributions is the same as that seen in Figure 9.1, which displays the results of the fit to the data using the assumption of the world average widths for the two K_1 resonances. The correlation between the estimated fractions of $K_1(1270)$ and $K_1(1400)$ obtained from this fit is -0.30 . A fit where the signal and $\tau^- \rightarrow \nu_\tau K^-\pi^-\pi^+\pi^0$ fractions are set to zero yields $-2 \log \mathcal{L}/\mathcal{L}_{\max} = 107$. Since this fit has three fewer degrees of freedom than the first, the difference in $-2 \log \mathcal{L}$ should be χ^2 distributed with three degrees of freedom if the sample does indeed consist of only three-pion background. This test disfavors this hypothesis at a confidence level of over 99%.

Table 9.1 includes estimates of the efficiencies for $\tau^- \rightarrow \nu_\tau K^-\pi^-\pi^+$ and $\tau^- \rightarrow \nu_\tau K^-\pi^-\pi^+\pi^0$ in the pre-selected tau-pair sample to contribute to the $\tau^- \rightarrow \nu_\tau K^-\pi^-\pi^+$ candidate samples. These efficiencies are not corrected for biases introduced by the $\tau^- \rightarrow \nu_\tau K^-\pi^-\pi^+$ selection procedure. In order to verify that the signal fractions returned by the fit are reasonable, we use these efficiencies and the fit fractions to calculate estimates of the $\tau^- \rightarrow \nu_\tau K^-\pi^-\pi^+$ and $\tau^- \rightarrow \nu_\tau K^-\pi^-\pi^+\pi^0$ branching ratios, which are also given in Table 9.1. Although the efficiencies have not been corrected for bias, these estimates are in agreement with the branching ratios obtained in Chapter 8 for all resonant structure assumptions, except for $\tau^- \rightarrow \nu_\tau K^-\pi^-\pi^+$ through phase space only.

¹Only one such bin exists in the fit for the central values of the signal and background fractions, and it contains only one event.

As a cross-check, Monte Carlo generated $\tau^- \rightarrow \nu_\tau K^- \omega$ decays are used to estimate the shape of the $\tau^- \rightarrow \nu_\tau K^- \pi^- \pi^+ \pi^0$ in the data distributions, rather than $\tau^- \rightarrow \nu_\tau K^- \pi^- \pi^+ \pi^0$ generated through non-resonant production. For all four assumptions made about the $\tau^- \rightarrow \nu_\tau K^- \pi^- \pi^+$ intermediate resonant structure, these fits return signal fractions within 0.15σ of the central values, and $\tau^- \rightarrow \nu_\tau K^- \pi^- \pi^+ \pi^0$ fractions within 0.35σ of the central values, where σ refers to the statistical uncertainties of the central values of the fractions.

9.2.1 $\tau^- \rightarrow \nu_\tau K_1$

Under the assumption that resonant structure of $\tau^- \rightarrow \nu_\tau K^- \pi^- \pi^+$ decays is dominated by the K_1 intermediate resonances, we derive

$$R_{\text{fit}} = \frac{\text{fraction of } K_1(1270) \text{ in } K^- \pi^- \pi^+ \text{ candidates}}{\text{fraction of } K_1(1400) + K_1(1270) \text{ in } K^- \pi^- \pi^+ \text{ candidates}} = 0.69 \pm 0.16.$$

where the uncertainty is statistical, and where the fractions of $K_1(1270)$ and $K_1(1400)$ are taken from the fit which assumes the widths of these resonances are 90 MeV and 174 MeV, respectively.

The signal and background template distributions used in the binned likelihood fit have statistical uncertainties associated with them. To determine the systematic uncertainties on the fit fractions arising from these uncertainties, the fit is repeated 25 times, each time randomly varying each bin of the template distributions by sampling Poisson distributions with means equal to the original bin contents. The resulting systematic uncertainties are included in Table 9.1, and are derived from the RMS spread of the signal fraction estimates from the 25 fits.

To check for undue variation that may be produced by the choice of binning used in the fit, the above procedure is repeated for various binning schemes. In all cases, the RMS variation of the results returned by the different fits is less than the statistical uncertainty from the original fit. The variation of R_{fit} due to uncertainty in the $K_1(1270)$ branching fractions is also studied, and found to be

$\tau^- \rightarrow \nu K^- \pi^- \pi^+$ candidates

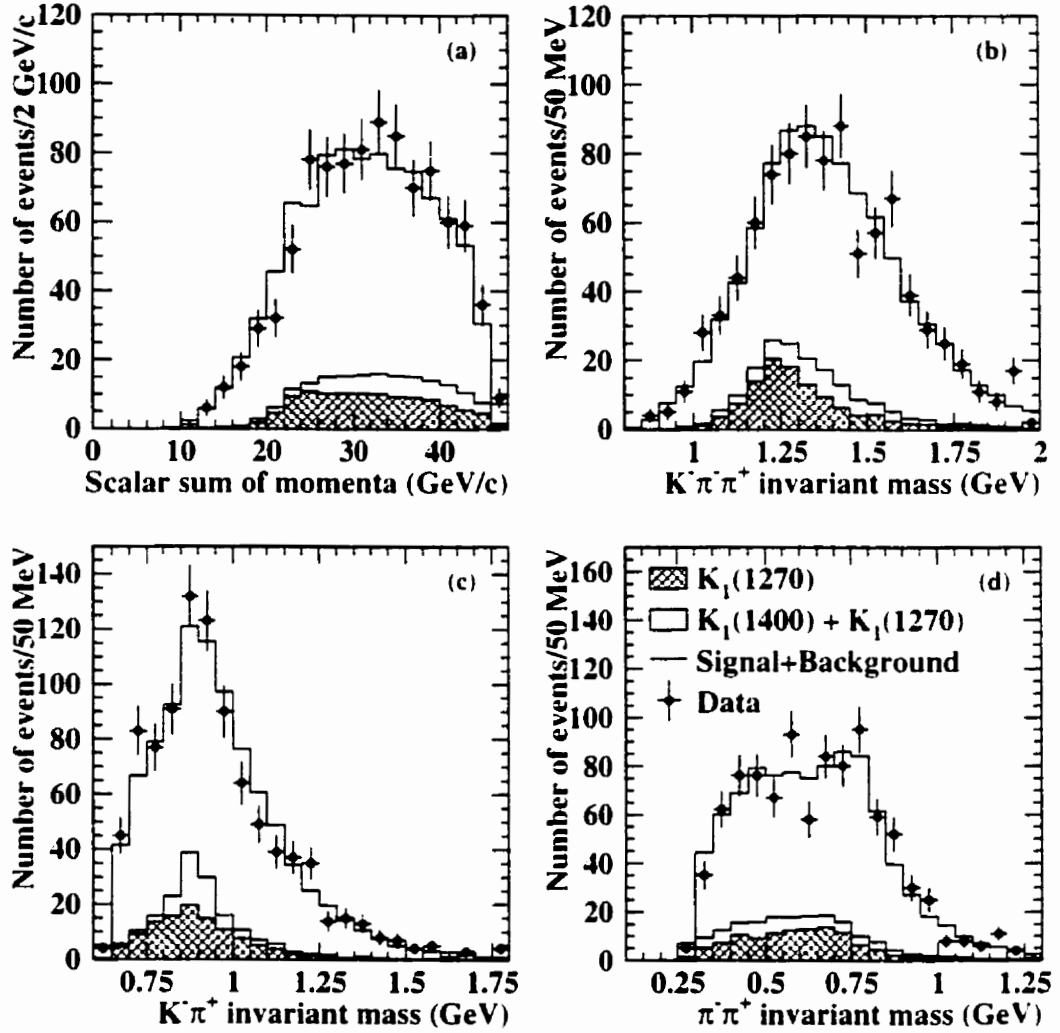


Figure 9.1: (a) is the $\sum p$ distribution and (b), (c), and (d) are the invariant mass distributions of the data $\tau^- \rightarrow \nu_\tau K^- \pi^- \pi^+$ candidate sample (points). The histogram represents the predicted distribution, in which the normalisation of the background and signal components comes from the best fit results of the binned maximum likelihood fit which took the correlations between the invariant mass distributions into account. The shape of the signal is estimated using $\tau^- \rightarrow \nu_\tau K^- \pi^- \pi^- \pi^+$ events generated through the $K_1(1270)$ and the $K_1(1400)$ resonances, where the widths of the resonances are taken to be 90 and 174 MeV, respectively [1]. The shape of the $\tau^- \rightarrow \nu_\tau \pi^- \pi^- \pi^+ (\pi^0)$ background in the distributions is obtained from a data control sample.

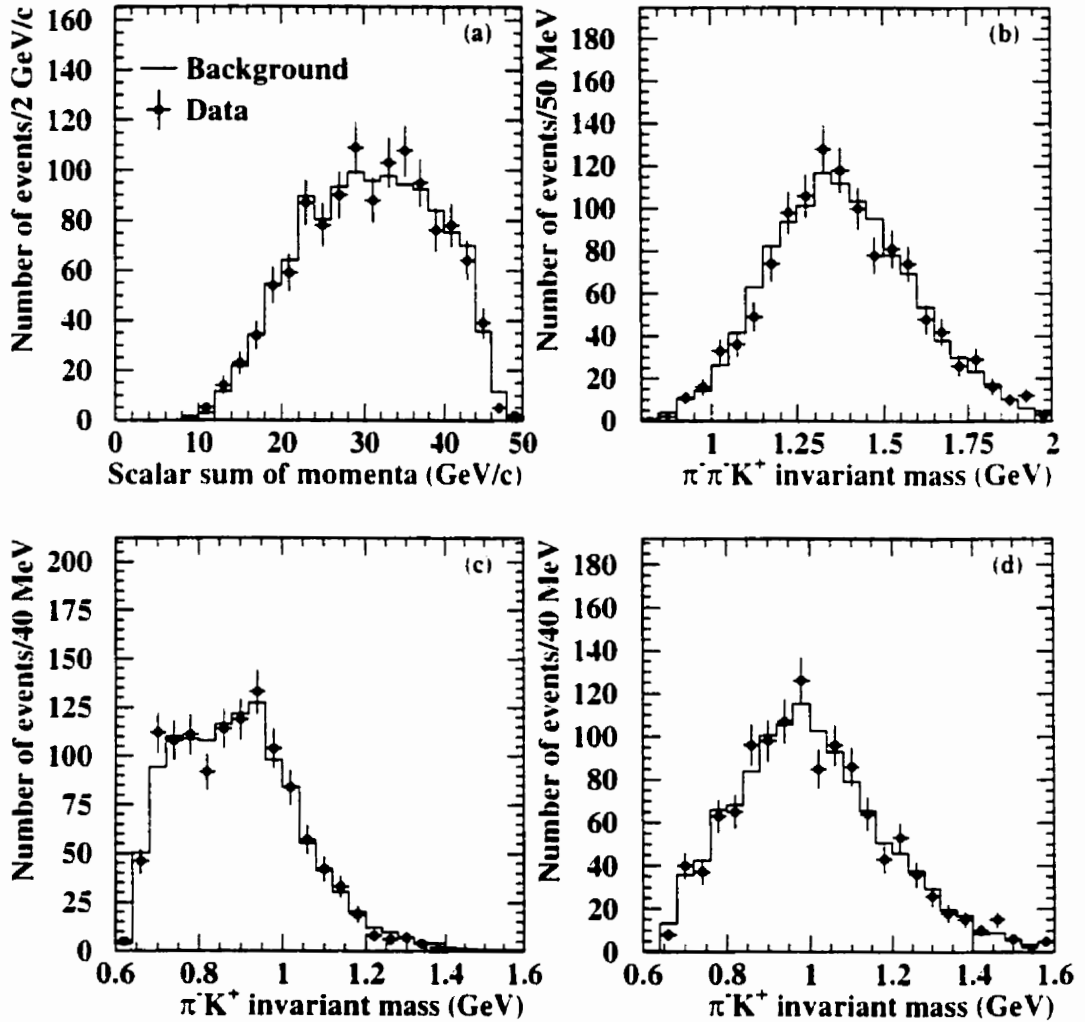
$\tau^- \rightarrow \nu \pi^- \pi^- K^+$ candidates


Figure 9.2: $\sum p$ and invariant mass distributions of the data $\tau^- \rightarrow \nu \pi^- \pi^- K^+$ candidate sample (points). Due to the strangeness constraints in tau decays, this sample is expected to consist entirely of $\tau^- \rightarrow \nu \pi^- \pi^- \pi^+ \geq 1\pi^0$ background, which is parameterised in the histogram by a data control sample of $\tau^- \rightarrow \nu \pi^- \pi^- \pi^+ \geq 1\pi^0$ events.

	$K_1(1270)$ and $K_1(1400)$ $\Gamma_{1270} = 90 \text{ MeV}$ $\Gamma_{1400} = 174 \text{ MeV}$	$K_1(1270)$ and $K_1(1400)$ $\Gamma_{1270} = 300 \text{ MeV}$ $\Gamma_{1400} = 300 \text{ MeV}$	$K^*(892)\pi^-$ and $\rho(770)K^-$	Phase Space
$f_{\text{signal}\#1}$	$f_{K_1(1400)} = 0.043 \pm 0.025 \pm 0.017$	$f_{K_1(1400)} = 0.065 \pm 0.025 \pm 0.021$	$f_{K^*\pi} = 0.100 \pm 0.027$	0.029 ± 0.033
$f_{\text{signal}\#2}$	$f_{K_1(1270)} = 0.096 \pm 0.034 \pm 0.028$	$f_{K_1(1270)} = 0.121 \pm 0.039 \pm 0.036$	$f_{\rho K} = 0.040 \pm 0.235$	-
$f_{K^-\pi^-\pi^+\pi^0}$	0.066 ± 0.028	0.048 ± 0.036	0.076 ± 0.030	0.082 ± 0.029
$-2 \log \mathcal{L}/\mathcal{L}_{\text{max}}$	8	0	3	96
$\chi^2(\Sigma p)$	15.9/18	17.4/18	17.3/18	22.9/18
$\chi^2(M_{K^-\pi^-\pi^+})$	26.5/20	23.7/20	26.7/20	29.0/20
$\chi^2(M_{K^-\pi^+})$	22.3/17	19.5/17	21.2/17	37.0/17
$\chi^2(M_{\pi^-\pi^+})$	26.1/18	27.8/18	26.3/18	25.9/18
$\chi^2 \text{ total}$	90.8/73	88.4/73	91.5/73	114.8/73
$\epsilon_{K^-\pi^-\pi^+}$	0.22	0.22	0.22	0.21
$\epsilon_{K^-\pi^+\pi^0}$	0.17	0.17	0.17	0.17
$B_{K^-\pi^-\pi^+}(\%)$	0.207 ± 0.054	0.271 ± 0.058	0.205 ± 0.334	0.045 ± 0.052
$B_{K^-\pi^-\pi^+\pi^0}(\%)$	0.128 ± 0.054	0.093 ± 0.069	0.147 ± 0.058	0.158 ± 0.056

Table 9.1: Summary of the $\tau^- \rightarrow \nu_\tau K^- \pi^- \pi^+$ signal and $\tau^- \rightarrow \nu_\tau K^- \pi^- \pi^+ \pi^0$ background fractions obtained from the binned maximum likelihood fits to the data $\tau^- \rightarrow \nu_\tau K^- \pi^- \pi^+$ candidate invariant mass and ΣP distributions. The first uncertainties are the statistical uncertainties from the fits. The second uncertainties for $f_{K_1(1400)}$ and $f_{K_1(1270)}$ are the systematic uncertainties due to the limited statistics in the Monte Carlo generated samples. Also shown are the values of $-2 \log \mathcal{L}/\mathcal{L}_{\text{max}}$ from the fit (relative to the best fit), and the resulting χ^2 per degree of freedom between the various data and predicted distributions. Estimates of the efficiencies for signal and $\tau^- \rightarrow \nu_\tau K^- \pi^- \pi^+ \pi^0$ decays in the tau-pair candidate sample to contribute to the $\tau^- \rightarrow \nu_\tau K^- \pi^- \pi^+$ sample are given. From these efficiencies and the fraction estimates from the fits, estimates of the branching ratios are calculated. These branching ratios have not been corrected for biases introduced by the event selection and are used as a cross-check of the analysis only. The branching ratio uncertainties are from the statistical uncertainties of the fit fractions.

negligible.

The value of R_{fit} is corrected for the efficiencies for $K_1(1270)$ and $K_1(1400)$ in the pre-selected tau-pair sample to contribute to the $\tau^- \rightarrow \nu_\tau K^- \pi^- \pi^+$ candidate sample (0.052 ± 0.001 and 0.058 ± 0.002 , respectively). This yields:

$$R = \frac{\text{Br}(\tau^- \rightarrow \nu_\tau K_1(1270))}{\text{Br}(\tau^- \rightarrow \nu_\tau K_1(1400)) + \text{Br}(\tau^- \rightarrow \nu_\tau K_1(1270))} = 0.71 \pm 0.16 \pm 0.11.$$

where the first uncertainty is due to the statistical uncertainty from the fit, and the second arises from the limited statistics of the Monte Carlo generated samples and the contribution from other systematic effects, the dominant source of which is the statistical variation in the signal and background template distributions.

To determine if R depends on assumptions made about the widths of the K_1 resonances, the above procedure is repeated, simulating the signal portion of the distributions using $\tau^- \rightarrow \nu_\tau K^- \pi^- \pi^+$ Monte Carlo events generated through the $K_1(1270)$ and $K_1(1400)$ resonances, both with width 300 MeV. This procedure yields:

$$R = 0.68 \pm 0.13 \pm 0.11.$$

which is in agreement with the central value of R to within 0.2σ of the combined Monte Carlo statistical uncertainty.

9.3 $\tau^- \rightarrow \nu_\tau K^- \pi^- K^+$

The sample of $\tau^- \rightarrow \nu_\tau K^- \pi^- K^+$ candidates is expected to consist of $\tau^- \rightarrow \nu_\tau \pi^- \pi^- \pi^+ (\pi^0)$ background, along with $\tau^- \rightarrow \nu_\tau K^- \pi^- K^+$ signal, some $\tau^- \rightarrow \nu_\tau K^- \pi^- K^+ \pi^0$ contamination, and some contamination from other tau decays and hadronic Z^0 events.

To analyse the resonant structure of $\tau^- \rightarrow \nu_\tau K^- \pi^- K^+$ decays, we examine the $M_{K^- \pi^- K^+}$, $M_{K^- K^+}$, and $M_{\pi^- K^+}$ invariant mass distributions of the candidates.

shown in Figure 9.3. To estimate the shape of the dominant three-pion background in these distributions, we use the $\tau^- \rightarrow \nu_\tau \pi^- \pi^- \pi^+ (\pi^0)$ candidate sample, with the 5 GeV/c momentum selection placed on the particles which correspond to the two kaon candidates. This selection produces a sample of over 10000 events.

The shape of the $\tau^- \rightarrow \nu_\tau K^- \pi^- K^+ \pi^0$ background in the distributions is parameterised with Monte Carlo $\tau^- \rightarrow \nu_\tau K^- \pi^- K^+ \pi^0$ events generated through phase space. Other background fractions are expected to be on the order of a percent or less and are neglected.

To describe the shape of the signal portion of these invariant mass distributions, we consider three different scenarios:

1. The $\tau^- \rightarrow \nu_\tau K^- \pi^- K^-$ decays occur through the same intermediate resonant structure used in the default version of Tauola 2.4.
2. The $\tau^- \rightarrow \nu_\tau K^- \pi^- K^-$ decays occur through $K^*(892)K^-$.
3. The $\tau^- \rightarrow \nu_\tau K^- \pi^- K^-$ decays occur through phase space only.

Monte Carlo samples having at least 10 times the statistics of the expected signal component of the data $\tau^- \rightarrow \nu_\tau K^- \pi^- \pi^+$ candidates are generated under each of these resonant structure assumptions.

To determine the composition of the candidate sample, we divide the $M_{K^- \pi^- K^+}$, $M_{K^- K^+}$, and $M_{\pi^- K^+}$ invariant masses of the data, signal Monte Carlo, and background samples into 24 bins each. Further discrimination between signal and background is obtained by dividing the scalar sum of the momenta in each three-prong decay into 24 bins between 0 and 48 GeV/c. Since this study is qualitative in nature only, correlations between the distributions are ignored.

The results of the fits using the three resonant structure assumptions are shown in Table 9.2. Table 9.2 also gives the χ^2 per degree of freedom between the data and predicted $\sum P$, $M_{K^- \pi^- K^+}$, $M_{K^- K^+}$, and $M_{\pi^- K^+}$ distributions, where the normalisation of the predicted distributions is obtained from the fit results. The binning of these distributions is the same as that seen in Figure 9.3, which displays

the results of the best fit to the data. A fit where the signal and $\tau^- \rightarrow \nu_\tau K^- \pi^- K^+ \pi^0$ fractions are set to zero yields $-2 \log \mathcal{L} / \mathcal{L}_{\max} = 51$. Since this fit has two fewer degrees of freedom than the first, the difference in $-2 \log \mathcal{L}$ should be χ^2 distributed with two degrees of freedom if the sample does indeed consist of only three-pion background. This test disfavours this hypothesis at a confidence level of over 99%.

Table 9.2 includes estimates of the efficiencies for $\tau^- \rightarrow \nu_\tau K^- \pi^- K^+$ and $\tau^- \rightarrow \nu_\tau K^- \pi^- K^+ \pi^0$ in the tau-pair sample to contribute to the $\tau^- \rightarrow \nu_\tau K^- \pi^- K^+$ candidate samples. These efficiencies are not corrected for biases introduced by the $\tau^- \rightarrow \nu_\tau K^- \pi^- K^+$ selection procedure. In order to verify that the signal fractions returned by the fit are reasonable, we use these efficiencies and the fit fractions to calculate estimates of the $\tau^- \rightarrow \nu_\tau K^- \pi^- K^+$ and $\tau^- \rightarrow \nu_\tau K^- \pi^- K^+ \pi^0$ branching ratios, which are also given in Table 9.2. Although the efficiencies have not been corrected for bias, these estimates are in agreement with the branching ratios obtained in Chapter 8 for all resonant structure assumptions.

As a cross-check, Monte Carlo generated $\tau^- \rightarrow \nu_\tau (K^*(892)K\pi)^-$ decays are used to estimate the shape of the $\tau^- \rightarrow \nu_\tau K^- \pi^- K^+ \pi^0$ in the data distributions, rather than $\tau^- \rightarrow \nu_\tau K^- \pi^- K^+ \pi^0$ generated through non-resonant production. For all three assumptions made about the $\tau^- \rightarrow \nu_\tau K^- \pi^- K^+$ intermediate resonant structure, these fits return signal fractions within 0.25σ of the central values, and $\tau^- \rightarrow \nu_\tau K^- \pi^- K^+ \pi^0$ fractions within 0.40σ of the central values, where σ refers to the statistical uncertainties of the central values of the fractions.

	Tauola 2.4 default mix of $a_1(1260)$ and $\rho'(1690)$	$K^*(892)K^-$	Phase Space
$f_{K^-\pi^-K^+}$	0.473 ± 0.057	0.447 ± 0.074	0.517 ± 0.086
$f_{K^-\pi^-K^+\pi^0}$	0.000 ± 0.304	0.141 ± 0.059	0.109 ± 0.061
$-2 \log \mathcal{L}/\mathcal{L}_{\max}$	0	18	21
$\chi^2 (\sum p)$	7.6/5	7.3/5	8.4/5
$\chi^2 (M_{K^-\pi^-K^+})$	7.0/6	8.7/6	7.8/6
$\chi^2 (M_{K^-K^+})$	5.5/6	10.6/6	8.5/6
$\chi^2 (M_{\pi^-K^+})$	3.8/5	4.5/5	8.6/5
χ^2 total	23.9/22	31.1/22	33.3/22
$\epsilon^{K^-\pi^-K^+}$	0.13	0.14	0.15
$\epsilon^{K^-\pi^-K^+\pi^0}$	0.10	0.10	0.10
$B_{K^-\pi^-K^+}(\%)$	0.096 ± 0.012	0.085 ± 0.014	0.096 ± 0.016
$B_{K^-\pi^-K^+\pi^0}(\%)$	0.000 ± 0.079	0.037 ± 0.015	0.028 ± 0.016

Table 9.2: Summary of the $\tau^- \rightarrow \nu_\tau K^-\pi^-K^+$ signal and $\tau^- \rightarrow \nu_\tau K^-\pi^-K^+\pi^0$ background fractions obtained from the binned maximum likelihood fits to the data $\tau^- \rightarrow \nu_\tau K^-\pi^-K^+$ candidate invariant mass and $\sum P$ distributions. The uncertainties are the statistical uncertainties from the fits. Also shown are the values of $-2 \log \mathcal{L}/\mathcal{L}_{\max}$ from the fit (relative to the best fit), and the resulting χ^2 per degree of freedom between the various data and predicted distributions. Estimates of the efficiencies for signal and $\tau^- \rightarrow \nu_\tau K^-\pi^-K^+\pi^0$ decays in the tau-pair candidate sample to contribute to the $\tau^- \rightarrow \nu_\tau K^-\pi^-K^+$ sample are given. From these efficiencies and the fraction estimates from the fits, estimates of the branching ratios are calculated. These branching ratios have not been corrected for biases introduced by the event selection and are used as a cross-check of the analysis only. The branching ratio uncertainties are from the statistical uncertainties of the fit fractions.

$\tau^- \rightarrow \nu K^- \pi^- K^+$ candidates

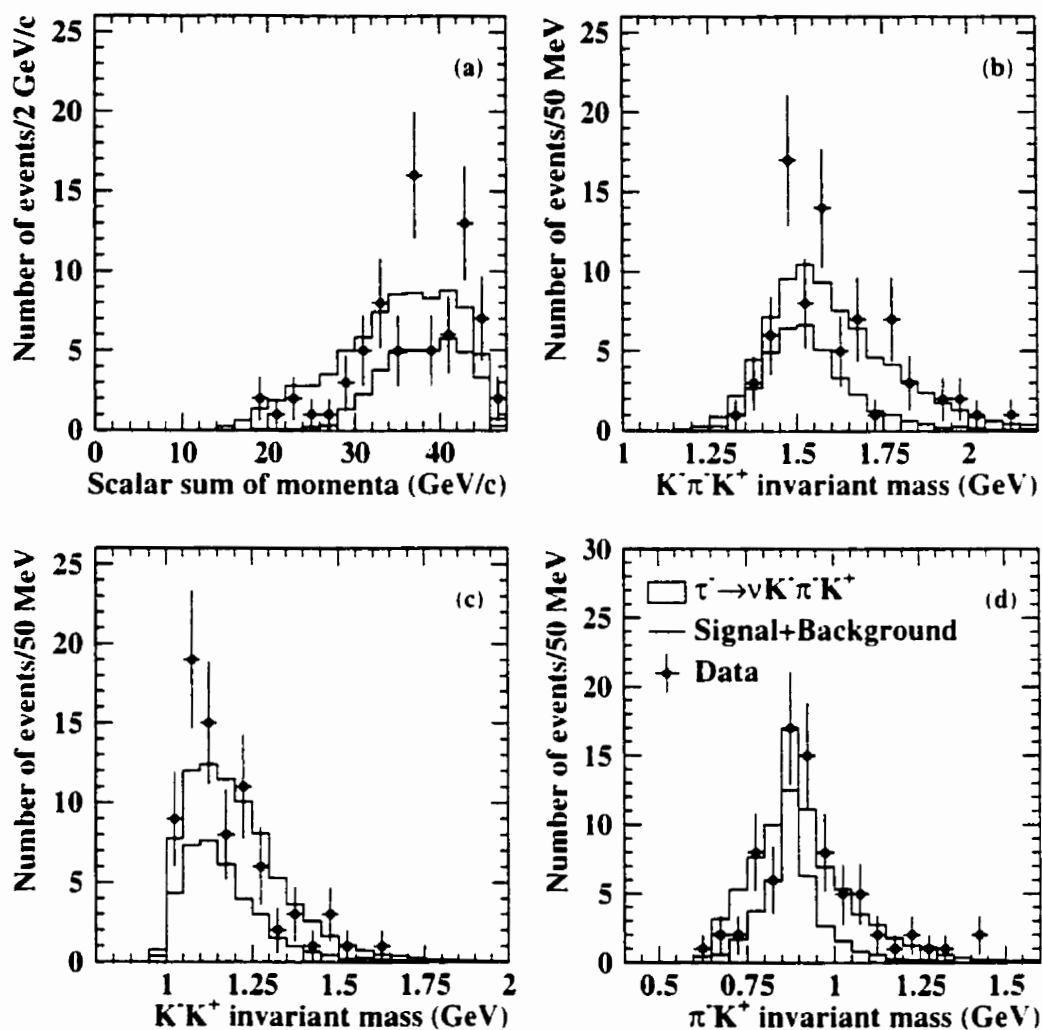


Figure 9.3: (a) is the Σp distribution and (b), (c), and (d) are the invariant mass distributions of the data $\tau^- \rightarrow \nu_\tau K^- \pi^- K^+$ candidate sample (points). The histogram represents the predicted distribution, in which the normalisation of the background and signal components comes from the results of the binned maximum likelihood fit to the four distributions. The shape of the $\tau^- \rightarrow \nu_\tau K^- \pi^- K^+$ signal distribution is simulated in the fit by Monte Carlo events generated by the default version of Tauola 2.4. The shape of the $\tau^- \rightarrow \nu_\tau \pi^- \pi^- \pi^+ (\pi^0)$ background in the distributions is obtained from a data control sample.

Chapter 10

Summary of Results and Conclusions

10.1 One-prong Tau Decays

From an analysis of the ionisation energy loss of charged particles selected from a sample of 220624 tau decay candidates recorded in the barrel region of the OPAL detector at e^-e^- centre-of-mass energies close to the Z^0 resonance, we determine the branching ratios:

$$\text{Br}(\tau^- \rightarrow \nu_\tau K^- \geq 0h^0) = 1.525 \pm 0.039 \pm 0.036\%$$

$$\text{Br}(\tau^- \rightarrow \nu_\tau K^-) = 0.651 \pm 0.026 \pm 0.023\%$$

where the first uncertainties are statistical and the second are systematic. Both the inclusive and exclusive branching ratios are in agreement with the world averages shown in Table 10.1. The OPAL $\tau^- \rightarrow \nu_\tau K^- \geq 0h^0$ branching ratio is the world's most precise measurement, while the OPAL $\tau^- \rightarrow \nu_\tau K^-$ branching ratio contributes significantly to the reduction of the uncertainty on the world average of that quantity.

The theoretical prediction for the $\tau^- \rightarrow \nu_\tau K^-$ branching ratio is calculated via:

$$\begin{aligned} \text{Br}(\tau^- \rightarrow \nu_\tau K^-) &= \frac{m_\tau^3 (1 - m_K^2/m_\tau^2)^2}{2m_K m_\mu^2 (1 - m_\mu^2/m_K^2)^2} \frac{\tau_\tau}{\tau_K} \text{Br}(K^- \rightarrow \mu^- \bar{\nu}_\mu) \\ &= 0.705 \pm 0.008\%. \end{aligned} \quad (10.1)$$

where the value of $\text{Br}(K^- \rightarrow \mu^- \bar{\nu}_\mu) = 0.6324 \pm 0.0044$ is taken from reference [1]. The OPAL measurement is in agreement with this prediction to within about 1.5 sigma of the combined uncertainties.

The theoretical prediction for the $\tau^- \rightarrow \nu_\tau K^- \geq 0h^0$ branching ratio is obtained by summing the theoretical predictions for the first five states appearing in Table 2.2.

$$\text{Br}(\tau^- \rightarrow \nu_\tau K^- \geq 0h^0) = 1.571 \pm 0.043\%.$$

The OPAL measurement is in agreement with this prediction to within 0.7 sigma of the combined uncertainties.

10.2 Three-prong Tau Decays

From a sample of 295852 tau decays recorded in the barrel and endcap regions of the OPAL detector at e^-e^- centre-of-mass energies close to the Z^0 resonance, we have determined the branching ratios:

$$\text{Br}(\tau^- \rightarrow \nu_\tau K^- \pi^- \pi^+ (\pi^0)) = 0.343 \pm 0.073 \pm 0.031 \%$$

$$\text{Br}(\tau^- \rightarrow \nu_\tau K^- \pi^- K^+ (\pi^0)) = 0.159 \pm 0.053 \pm 0.020 \%$$

$$\text{Br}(\tau^- \rightarrow \nu_\tau K^- \pi^- \pi^+ \pi^0) < 0.173 \% \quad (95\% \text{ CL})$$

$$\text{Br}(\tau^- \rightarrow \nu_\tau K^- \pi^- K^+ \pi^0) < 0.266 \% \quad (95\% \text{ CL})$$

$$\text{Br}(\tau^- \rightarrow \nu_\tau K^- \pi^- \pi^+) = 0.360 \pm 0.082 \pm 0.048 \%$$

τ^- DECAY MODE	EXPERIMENT BR (%)	
$\tau^- \rightarrow \nu_\tau K^-$	0.696 ± 0.029	ALEPH99[36]
	0.85 ± 0.18	DELPHI94[61]
	0.66 ± 0.11	CLEO94[62]
	0.59 ± 0.18	DELCO84[63]
	0.694 ± 0.027	(average)
	0.651 ± 0.035	(this analysis)
$\tau^- \rightarrow \nu_\tau K^- \geq 0h^0$	1.52 ± 0.06	ALEPH99[36]
	1.54 ± 0.24	DELPHI94[61]
	1.70 ± 0.22	CLEO94[62]
	1.71 ± 0.29	DELCO84[63]
	1.54 ± 0.06	(average)
	1.525 ± 0.052	(this analysis)

Table 10.1: Summary of the $\tau^- \rightarrow \nu_\tau K^-$ and $\tau^- \rightarrow \nu_\tau K^- \geq 0h^0$ branching ratios (charge conjugate decays are implied). Experimental uncertainties are the combined statistical and systematic uncertainties, and the averages do not include the results presented here.

$$\text{Br}(\tau^- \rightarrow \nu_\tau K^- \pi^- K^+) = 0.087 \pm 0.056 \pm 0.040 \%,$$

where the first uncertainty is statistical and the second is systematic. The 95% confidence limits are derived for the branching ratio measurements less than $+1\sigma$ from zero, using the method recommended in reference [67].

The $\tau^- \rightarrow \nu_\tau K^- \pi^- \pi^+$ inclusive and exclusive branching ratios are in agreement with previous experimental measurements, as listed in Table 10.2. The OPAL exclusive $\tau^- \rightarrow \nu_\tau K^- \pi^- \pi^+$ branching ratio agrees best with the theoretical prediction of reference [38], which assumes in the calculation that the intermediate resonant structure of the final state is dominated by K_1 resonances with widths of 250 MeV.

In a separate analysis, we explore the resonant structure of $\tau^- \rightarrow \nu_\tau K^- \pi^- \pi^+$ and $\tau^- \rightarrow \nu_\tau K^- \pi^- K^+$ decays. Under the assumption that the intermediate resonant structure of the tau decay to the $\nu_\tau K^- \pi^- \pi^+$ final state is dominated by the K_1 intermediate resonances, we determine:

$$R = \frac{\text{Br}(\tau^- \rightarrow \nu_\tau K_1(1270))}{\text{Br}(\tau^- \rightarrow \nu_\tau K_1(1400)) + \text{Br}(\tau^- \rightarrow \nu_\tau K_1(1270))} = 0.71 \pm 0.16 \pm 0.11.$$

There are two previously published results for R :

$$R = 0.35_{-0.21}^{+0.29} \quad \text{TPC}/2\gamma \text{ 1994 [40]}$$

$$R = 0.91 \pm 0.29 \quad \text{ALEPH 1999 [27]}.$$

with an average of 0.63 ± 0.21 . The OPAL result is in agreement with this average.

It has been suggested in [38] that theoretical predictions best match the world averages for the $\tau^- \rightarrow (K\pi\pi)^-$ branching ratios if the K_1 resonances are in fact wider than the current world average widths. $\Gamma_{K_1(1270)} = 90$ MeV and $\Gamma_{K_1(1400)} = 174$ MeV. From $SU(3)$ flavour symmetry arguments, reference [38] suggests that the actual widths of these resonances are likely to be approximately the $a_1(1260)$ width (250 MeV or greater). We find that the data do indeed favour wider K_1 resonances, but that the world average widths are also consistent with

the data.

We also examine the resonant structure of $\tau^- \rightarrow \nu_\tau K^- \pi^- K^+$ candidates, and find evidence for $K^- K^*(892)$ production, in a manner consistent with the model used in reference [35].

10.3 Conclusions

Dramatic inroads have been made in the past two years into the understanding of the physics of tau decays to final states with kaons. The studies presented here have contributed significantly to this knowledge.

Many questions still remain however. For instance, the few experimental studies that have been done to-date of $\tau^- \rightarrow \nu_\tau K^- \pi^- \pi^-$ decays have not definitively unlocked the mysteries of the resonant structure of these decays. In addition, it is still possible that future $\tau^- \rightarrow \nu_\tau K^- \pi^- \pi^-$ data may yet provide measurements of the K_1 resonant widths, either confirming or rejecting the theoretical predictions that use SU(3) flavour symmetry arguments to relate the properties of the K_1 resonances to the properties of the a_1 .

The exact nature of the resonant structure of $\tau^- \rightarrow \nu_\tau K^- \pi^- K^-$ decays has also yet to be satisfactorily studied. In addition, the resonant structure of four meson final states that include kaons is, as yet, unknown, and precision measurements of the branching ratios to these final states are lacking.

One of the most likely venues to answer these remaining questions is the BaBar experiment at the PEP-II electron-positron colliding beam facility at the Stanford Linear Accelerator Center. In spring 1999 this detector began taking data with the primary aim of studying the production and decay of mesons which include a b quark. However, the excellent charge particle identification capabilities of this detector will also make the experiment a promising laboratory for the study of tau decays with charged kaons in the final state. Other experiments which may also be able to precisely study these final states are the Belle experiment at the

τ^- DECAY MODE	EXPERIMENT BR (%)		THEORY BR (%)
$\nu_\tau K^- \pi^- \pi^+ (\pi^0)$	0.275 ± 0.064	ALEPH98[41]	-
	0.421 ± 0.068	CLEO98[66]	
	$0.58^{+0.19}_{-0.18}$	TPC/2-94[40]	
	$0.22^{+0.17}_{-0.16}$	DELCO85[65]	
	0.348 ± 0.044	(average)	
	0.343 ± 0.079	(this analysis)	
$\nu_\tau K^- \pi^- K^+ (\pi^0)$	0.238 ± 0.042	ALEPH98[41]	-
	0.178 ± 0.036	CLEO98[66]	
	$0.15^{+0.09}_{-0.08}$	TPC/2-94[40]	
	0.198 ± 0.026	(average)	
	0.159 ± 0.057	(this analysis)	
$\nu_\tau K^- \pi^- \pi^-$	0.214 ± 0.047	ALEPH98[41]	0.77 [37]
	0.346 ± 0.061	CLEO98[66]	0.35 to 0.45 [38]
	0.263 ± 0.037	(average)	0.18 [42]
	0.360 ± 0.095	(this analysis)	
$\nu_\tau K^- \pi^- K^-$	0.163 ± 0.027	ALEPH98[41]	0.20 [37]
	0.145 ± 0.031	CLEO98[66]	0.26 [42]
	$0.22^{+0.18}_{-0.12}$	DELCO85[65]	
	0.156 ± 0.020	(average)	
	0.087 ± 0.069	(this analysis)	
$\nu_\tau K^- \pi^- \pi^+ \pi^0$	0.061 ± 0.043	ALEPH98[41]	-
	0.075 ± 0.032	CLEO98[66]	
	0.070 ± 0.026	(average)	
	< 0.173	(this analysis)	
$\nu_\tau K^- \pi^- K^+ \pi^0$	0.075 ± 0.033	ALEPH98[41]	-
	0.033 ± 0.019	CLEO98[66]	
	0.043 ± 0.016	(average)	
	< 0.266	(this analysis)	

Table 10.2: Summary of the dominant branching ratios of three-prong decays of the tau lepton that include charged kaons in the final state (charge conjugate decays are implied). Experimental uncertainties are the combined statistical and systematic uncertainties. Branching ratios quoted as limits are the 95% confidence limits, and the (π^0) notation refers to decay modes with or without an accompanying π^0 . The averages do not include the results presented here.

KEKB e^+e^- colliding beam facility, and the CLEO-III experiment at the CESR e^+e^- colliding beam facility, both of which also began taking data in 1999. Over the next five to ten years, it will be very interesting to watch the developments in tau physics achieved by these, and possibly other, experiments.

Appendix A

Phenomenological Parameterisation of Resonant Amplitudes

The amplitude for the production of a resonant state of mass M_0 and width Γ_0 in a multi-particle decay is usually parameterised as a function of the energy \mathcal{Q} using the Breit-Wigner form such as [68]:

$$\mathcal{A}(\mathcal{Q}) = \frac{M_0^2}{(\mathcal{Q}^2 - M_0^2 + iM_0\Gamma_0)}. \quad (\text{A.1})$$

In the neighbourhood of the pole of a very narrow resonance, equation A.1 yields a good approximation to the experimentally observed $|\mathcal{A}|^2$. However, the correct threshold behaviour of $|\mathcal{A}|^2$ for wide resonances can only be achieved if the width of the resonance in Equation A.1 is a function of \mathcal{Q} [68]:

$$\mathcal{A}(\mathcal{Q}) = \frac{M_0^2}{(\mathcal{Q}^2 - M_0^2 + iM_0\gamma_0(\mathcal{Q}))}. \quad (\text{A.2})$$

The following is a discussion of the parameterisation of γ_0 for the decay of a resonance to two stable particles, and for the quasi-two-body decay of a resonance

to a final state which consists of a stable particle and a second resonance [56].

A.1 Decay of a Resonance to Two Stable Particles

For the decay of a resonance of mass M_0 , width Γ_0 , and orbital angular momentum l , to a final state which consists of two stable particles of masses m_1 and m_2 , we have that the energy dependent width is:

$$\gamma_0(\mathcal{Q}, m_1, m_2) = \Gamma_0 \frac{\rho(\mathcal{Q}, m_1, m_2)}{\rho(M_0, m_1, m_2)}, \quad (\text{A.3})$$

where

$$\rho(\mathcal{Q}, m_1, m_2) = \left[a(\mathcal{Q}, m_1, m_2) \right]^{(2l+1)/2},$$

and where

$$a(\mathcal{Q}, m_1, m_2) = \frac{[\mathcal{Q}^2 - (m_1 + m_2)^2][\mathcal{Q}^2 - (m_1 - m_2)^2]}{4\mathcal{Q}^2}. \quad (\text{A.4})$$

The function $a(\mathcal{Q})$ is taken to be zero if $\mathcal{Q} < (m_1 + m_2)$.

A.2 Decay of a Resonance to a Stable Particle and a Secondary Resonance

Now consider the quasi-two-body decay of a primary resonance of mass M and width Γ to a final state which consists of a stable particle of mass m_3 and a second resonance of mass M_0 and width Γ_0 , which in turn decays to two stable particles of masses m_1 and m_2 . The orbital angular momentum of the primary resonance is

L , and its energy dependent width is given by:

$$\gamma(\mathcal{Q}, m_1, m_2, m_3) = \Gamma \frac{\rho(\mathcal{Q}, m_1, m_2, m_3)}{\rho(\mathcal{M}, m_1, m_2, m_3)},$$

where

$$\rho(\mathcal{Q}, m_1, m_2, m_3) = \int_{m_1+m_2}^{\mathcal{Q}-m_3} \sigma(\mathcal{M}, M_0, m_1, m_2) \left[a(\mathcal{Q}, m_3, \mathcal{M}) \right]^{(2L-1)/2} d\mathcal{M},$$

and where the function $a(\mathcal{Q}, m_3, \mathcal{M})$ is the same as in Equation A.4. The distribution function $\sigma(\mathcal{M}, M_0, m_1, m_2)$ is

$$\sigma(\mathcal{M}, M_0, m_1, m_2) = \frac{\gamma_0(\mathcal{M}, m_1, m_2)/2\pi}{(\mathcal{M} - M_0)^2 + (\gamma_0(\mathcal{M}, m_1, m_2)/2)^2},$$

where the function $\gamma_0(\mathcal{M}, m_1, m_2)$ is the same as in Equation A.3.

Note that $\gamma(\mathcal{Q}, m_1, m_2, m_3)$ is, in general, non-zero if the mass of the secondary resonance exceeds that of the primary resonance. However, $\gamma(\mathcal{Q}, m_1, m_2, m_3)$ will be zero if $\mathcal{Q} < (m_1 + m_2 + m_3)$.

Also note that in the limit $\Gamma_0 \rightarrow 0$ we have that $\sigma(\mathcal{M}, M_0, m_1, m_2) \rightarrow \delta(\mathcal{M} - M_0)$, and ρ becomes a function of only \mathcal{Q} , M_0 , and m_3 (ie: the quasi-two-body decay can now be treated as a two-body decay).

Appendix B

OPAL Track Parameters

The geometry associated with the OPAL track parameters, $(\kappa, \phi_0, d_0, \tan \lambda, z_0)$, is shown in Figure B.1. The track parameters are defined as follows:

- κ is the curvature with

$$|\kappa| = \frac{1}{2\rho}$$

where ρ is the radius of curvature of the track and κ is signed such that positive κ means that ϕ increases when moving along the track from the point of closest approach to the origin in the $r - \phi$ plane (point-of-closest-approach). Note that for an axial magnetic field with B_z along the positive z axis, positive κ corresponds to a particle with negative physical charge.

- ϕ_0 is the azimuthal angle made by the tangent to the track at the point-of-closest-approach.
- The impact parameter d_0 is the transverse distance from the origin to the point-of-closest-approach. $d_0 = y_0 \cos \phi_0 - x_0 \sin \phi_0$.
- $\tan \lambda = \cot \theta$, where θ is the track polar angle measured from the $+ve z$ axis.
- The impact parameter z_0 is the z co-ordinate when the track is at the point-of-closest-approach.

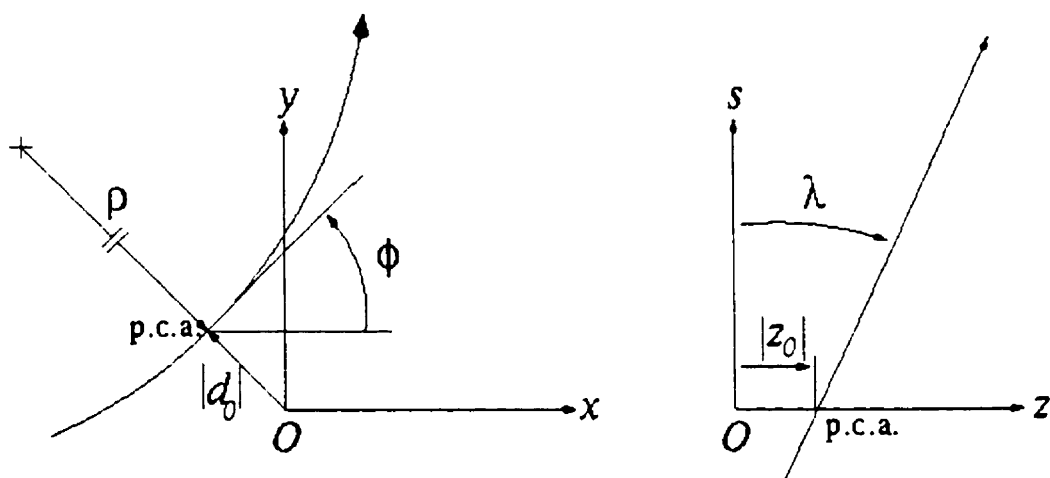


Figure B.1: Geometry associated with the OPAL track parameters. (a) shows the track $x - y$ projection, perpendicular to the z axis, while (b) shows the projection in the $s - z$ plane, where s is the track path-length measured from the point-of-closest-approach (p.c.a) to the origin

The impact parameters d_0 and z_0 are defined with respect to the origin of the coordinate system and not with respect to the actual beam interaction point.

The transverse momentum of the track, p_T , is related to the track parameters by

$$p_T = a \left| \frac{B_z}{\kappa} \right|.$$

If p_T is measured in GeV/c, B_z in kG and κ in cm^{-1} , then

$$a = \frac{c}{2} \times 10^{-14} \simeq 1.5 \times 10^{-4}.$$

The various components of the three-momentum are:

$$p_x = p_T \cos \phi_0$$

$$p_y = p_T \sin \phi_0$$

$$p_z = p_T \tan \lambda$$

$$p = p_T \sqrt{1 + \tan^2 \lambda}.$$

Appendix C

The OPAL Collaboration

The following list reflects the OPAL author list as of June 1999. Past members of the OPAL collaboration may be found in the list of authors in earlier OPAL publications.

G. Abbiendi², K. Ackerstaff⁸, G. Alexander²³, J. Allison¹⁶, K.J. Anderson⁹,
S. Anderson¹², S. Arcelli¹⁷, S. Asai²⁴, S.F. Ashby¹, D. Axen²⁹, G. Azuelos^{18,a},
A.H. Ball⁸, E. Barberio⁸, R.J. Barlow¹⁶, J.R. Batley⁵, S. Baumann³, J. Bechtluft¹⁴,
T. Behnke²⁷, K.W. Bell²⁰, G. Bella²³, A. Bellerive⁹, S. Bentvelsen⁸, S. Bethke¹⁴,
S. Betts¹⁵, O. Biebel¹⁴, A. Biguzzi⁵, I.J. Bloodworth¹, P. Bock¹¹, J. Böhme¹⁴,
O. Boeriu¹⁰, D. Bonacorsi², M. Boutemeur³³, S. Braibant⁸, P. Bright-Thomas¹,
L. Brigliadori², R.M. Brown²⁰, H.J. Burekhart⁸, P. Capiluppi², R.K. Carnegie⁶,
A.A. Carter¹³, J.R. Carter⁵, C.Y. Chang¹⁷, D.G. Charlton^{1,b}, D. Chrisman⁴,
C. Ciocca², P.E.L. Clarke¹⁵, E. Clay¹⁵, I. Cohen²³, J.E. Conboy¹⁵, O.C. Cooke⁸,
J. Couchman¹⁵, C. Couyoumtzelis¹³, R.L. Coxe⁹, M. Cuffiani², S. Dado²²,
G.M. Dallavalle², S. Dallison¹⁶, R. Davis³⁰, S. De Jong¹², A. de Roeck⁸,
P. Dervan¹⁵, K. Desch²⁷, B. Dienes^{32,h}, M.S. Dixit⁷, M. Donkers⁶, J. Dubbert³³,
E. Duchovni²⁶, G. Duckeck³³, I.P. Duerdoth¹⁶, P.G. Estabrooks⁶, E. Etzion²³,
F. Fabbri², A. Fanfani², M. Fanti², A.A. Faust³⁰, L. Feld¹⁰, P. Ferrari¹²,
F. Fiedler²⁷, M. Fierro², I. Fleck¹⁰, A. Frey⁸, A. Fürtjes⁸, D.I. Futyan¹⁶,

P. Gagnon⁷, J.W. Gary⁴, G. Gaycken²⁷, C. Geich-Gimbel³, G. Giacomelli²,
 P. Giacomelli², W.R. Gibson¹³, D.M. Gingrich^{30,a}, D. Glenzinski⁹, J. Goldberg²²,
 W. Gorn⁴, C. Grandi², K. Graham²⁸, E. Gross²⁶, J. Grunhaus²³, M. Gruwé²⁷,
 C. Hajdu³¹, G.G. Hanson¹², M. Hansroul⁸, M. Hapke¹³, K. Harder²⁷, A. Harel²²,
 C.K. Hargrove⁷, M. Harin-Dirac⁴, M. Hauschild⁸, C.M. Hawkes¹, R. Hawkings²⁷,
 R.J. Hemingway⁶, G. Herten¹⁰, R.D. Heuer²⁷, M.D. Hildreth⁸, J.C. Hill⁵,
 P.R. Hobson²⁵, A. Hocker⁹, K. Hoffman⁸, R.J. Homer¹, A.K. Honma^{28,a},
 D. Horváth^{31,c}, K.R. Hossain³⁰, R. Howard²⁹, P. Hüntemeyer²⁷, P. Igo-Kemenes¹¹,
 D.C. Imrie²⁵, K. Ishii²⁴, F.R. Jacob²⁰, A. Jawahery¹⁷, H. Jeremie¹⁸, M. Jimack¹,
 C.R. Jones⁵, P. Jovanovic¹, T.R. Junk⁶, N. Kanaya²⁴, J. Kanzaki²⁴, D. Karlen⁶,
 V. Kartvelishvili¹⁶, K. Kawagoe²⁴, T. Kawamoto²⁴, P.I. Kayal³⁰, R.K. Keeler²⁸,
 R.G. Kellogg¹⁷, B.W. Kennedy²⁰, D.H. Kim¹⁹, A. Klier²⁶, T. Kobayashi²⁴,
 M. Kobel^{3,d}, T.P. Kokott³, M. Kolrep¹⁰, S. Komamiya²⁴, R.V. Kowalewski²⁸,
 T. Kress¹, P. Krieger⁶, J. von Krogh¹¹, T. Kuhl³, P. Kyberd¹³, G.D. Lafferty¹⁶,
 H. Landsman²², D. Lanske¹⁴, J. Lauber¹⁵, I. Lawson²⁸, J.G. Layter¹, D. Lellouch²⁶,
 J. Letts¹², L. Levinson²⁶, R. Liebisch¹¹, J. Lillich¹⁰, B. List⁸, C. Littlewood⁵,
 A.W. Lloyd¹, S.L. Lloyd¹³, F.K. Loebinger¹⁶, G.D. Long²⁸, M.J. Losty⁷, J. Lu²⁹,
 J. Ludwig¹⁰, D. Liu¹², A. Macchiolo¹⁸, A. Macpherson³⁰, W. Mader³, M. Mannelli⁸,
 S. Marcellini², T.E. Marchant¹⁶, A.J. Martin¹³, J.P. Martin¹⁸, G. Martinez¹⁷,
 T. Mashimo²⁴, P. Mättig²⁶, W.J. McDonald³⁰, J. McKenna²⁹, E.A. Mckigney¹⁵,
 T.J. McMahon¹, R.A. McPherson²⁸, F. Meijers⁸, P. Mendez-Lorenzo³³,
 F.S. Merritt⁹, H. Mes⁷, I. Meyer⁵, A. Michelini², S. Mihara²⁴, G. Mikenberg²⁶,
 D.J. Miller¹⁵, W. Mohr¹⁰, A. Montanari², T. Mori²⁴, K. Nagai⁸, I. Nakamura²⁴,
 H.A. Neal^{12,g}, R. Nisius⁸, S.W. O'Neale¹, F.G. Oakham⁷, F. Odorici²,
 H.O. Ogren¹², A. Okpara¹¹, M.J. Oreglia⁹, S. Orito²⁴, G. Pásztor³¹, J.R. Pater¹⁶,
 G.N. Patrick²⁰, J. Patt¹⁰, R. Perez-Ochoa⁸, S. Petzold²⁷, P. Pfeifenschneider¹⁴,
 J.E. Pilcher⁹, J. Pinfold³⁰, D.E. Plane⁸, P. Poffenberger²⁸, B. Poli², J. Polok⁸,
 M. Przybycień^{8,e}, A. Quadt⁸, C. Rembser⁸, H. Rick⁸, S. Robertson²⁸,
 S.A. Robins²², N. Rodning³⁰, J.M. Roney²⁸, S. Rosati³, K. Roscoe¹⁶, A.M. Rossi².

Y. Rozen²², K. Runge¹⁰, O. Runolfsson⁸, D.R. Rust¹², K. Sachs¹⁰, T. Saeki²⁴,
 O. Sahr³³, W.M. Sang²⁵, E.K.G. Sarkisyan²³, C. Sbarra²⁹, A.D. Schaile³³,
 O. Schaile³³, P. Scharff-Hansen⁸, J. Schieck¹¹, S. Schmitt¹¹, A. Schöning⁸,
 M. Schröder⁸, M. Schumacher³, C. Schwick⁸, W.G. Scott²⁰, R. Seuster¹⁴,
 T.G. Shears⁸, B.C. Shen⁴, C.H. Shepherd-Themistocleous⁵, P. Sherwood¹⁵,
 G.P. Sirolì², A. Skuja¹⁷, A.M. Smith⁸, G.A. Snow¹⁷, R. Sobie²⁸,
 S. Söldner-Rembold^{10,f}, S. Spagnolo²⁰, M. Sproston²⁰, A. Stahl³, K. Stephens¹⁶,
 K. Stoll¹⁰, D. Strom¹⁹, R. Ströhmer³³, B. Surrow⁸, S.D. Talbot¹, P. Taras¹⁸,
 S. Tarem²², R. Teuscher⁹, M. Thiergen¹⁰, J. Thomas¹⁵, M.A. Thomson⁸,
 E. Torrence⁸, S. Towers⁶, T. Trefzger³³, I. Trigger¹⁸, Z. Trócsányi^{32,h}, E. Tsur²³,
 M.F. Turner-Watson¹, I. Ueda²⁴, R. Van Kooten¹², P. Vannerem¹⁰, M. Verzocchi⁷,
 H. Voss³, F. Wäckerle¹⁰, A. Wagner²⁷, D. Waller⁶, C.P. Ward⁵, D.R. Ward⁵,
 P.M. Watkins¹, A.T. Watson¹, N.K. Watson¹, P.S. Wells⁸, N. Wermes⁴,
 D. Wetterling¹¹, J.S. White⁶, G.W. Wilson¹⁶, J.A. Wilson¹, T.R. Wyatt¹⁶,
 S. Yamashita²⁴, V. Zacek¹⁸, D. Zer-Zion⁸

¹School of Physics and Astronomy, University of Birmingham, Birmingham B15
 2TT, UK

²Dipartimento di Fisica dell' Università di Bologna and INFN, I-40126 Bologna,
 Italy

³Physikalisches Institut, Universität Bonn, D-53115 Bonn, Germany

⁴Department of Physics, University of California, Riverside CA 92521, USA

⁵Cavendish Laboratory, Cambridge CB3 0HE, UK

⁶Ottawa-Carleton Institute for Physics, Department of Physics, Carleton Univer-
 sity, Ottawa, Ontario K1S 5B6, Canada

⁷Centre for Research in Particle Physics, Carleton University, Ottawa, Ontario
 K1S 5B6, Canada

⁸CERN, European Organisation for Particle Physics, CH-1211 Geneva 23, Switzer-
 land

⁹Enrico Fermi Institute and Department of Physics, University of Chicago, Chicago IL 60637, USA

¹⁰Fakultät für Physik, Albert Ludwigs Universität, D-79104 Freiburg, Germany

¹¹Physikalisches Institut, Universität Heidelberg, D-69120 Heidelberg, Germany

¹²Indiana University, Department of Physics, Swain Hall West 117, Bloomington IN 47405, USA

¹³Queen Mary and Westfield College, University of London, London E1 4NS, UK

¹⁴Technische Hochschule Aachen, III Physikalisches Institut, Sommerfeldstrasse 26-28, D-52056 Aachen, Germany

¹⁵University College London, London WC1E 6BT, UK

¹⁶Department of Physics, Schuster Laboratory, The University, Manchester M13 9PL, UK

¹⁷Department of Physics, University of Maryland, College Park, MD 20742, USA

¹⁸Laboratoire de Physique Nucléaire, Université de Montréal, Montréal, Quebec H3C 3J7, Canada

¹⁹University of Oregon, Department of Physics, Eugene OR 97403, USA

²⁰CLRC Rutherford Appleton Laboratory, Chilton, Didcot, Oxfordshire OX11 0QX, UK

²²Department of Physics, Technion-Israel Institute of Technology, Haifa 32000, Israel

²³Department of Physics and Astronomy, Tel Aviv University, Tel Aviv 69978, Israel

²⁴International Centre for Elementary Particle Physics and Department of Physics, University of Tokyo, Tokyo 113-0033, and Kobe University, Kobe 657-8501, Japan

²⁵Institute of Physical and Environmental Sciences, Brunel University, Uxbridge, Middlesex UB8 3PH, UK

²⁶Particle Physics Department, Weizmann Institute of Science, Rehovot 76100, Israel

²⁷Universität Hamburg/DESY, II Institut für Experimental Physik, Notkestrasse

85. D-22607 Hamburg, Germany

²⁸University of Victoria, Department of Physics, P O Box 3055, Victoria BC V8W 3P6, Canada

²⁹University of British Columbia, Department of Physics, Vancouver BC V6T 1Z1, Canada

³⁰University of Alberta, Department of Physics, Edmonton AB T6G 2J1, Canada

³¹Research Institute for Particle and Nuclear Physics, H-1525 Budapest, P O Box 49, Hungary

³²Institute of Nuclear Research, H-4001 Debrecen, P O Box 51, Hungary

³³Ludwigs-Maximilians-Universität München, Sektion Physik, Am Coulombwall 1, D-85748 Garching, Germany

^a and at TRIUMF, Vancouver, Canada V6T 2A3

^b and Royal Society University Research Fellow

^c and Institute of Nuclear Research, Debrecen, Hungary

^d on leave of absence from the University of Freiburg

^e and University of Mining and Metallurgy, Cracow

^f and Heisenberg Fellow

^g now at Yale University, Dept of Physics, New Haven, USA

^h and Department of Experimental Physics, Lajos Kossuth University, Debrecen, Hungary.

Bibliography

- [1] *Review of Particle Physics*. Eur. Phys. J. C, **Vol. 3**, Number 1-4 (1998).
- [2] S.L. Glashow. Nucl. Phys. **22** (1961) 579.
- [3] S. Weinberg. Phys. Rev. Lett. **19** (1967) 1264.
- [4] A. Salam. Elementary Particle Theory (N. Svartholm, ed) (1968).
- [5] P.W. Higgs. Phys. Rev. Lett. **12** (1964) 132.
- [6] P.W. Higgs. Phys. Rev. Lett. **13** (1964) 508.
- [7] G. D'Agostini and G. Degrossi. Eur. Phys. J **C10** (1999) 663.
- [8] UA1 Collaboration. G. Arnison *et al.*. Phys. Lett. **B126** (1983) 398.
- [9] UA2 Collaboration. R. Ansari *et al.*. Phys. Lett. **B194** (1987) 158.
- [10] G. Altarelli *et al.*. CERN yellow report 89-08. **Volumes 1-3**. 1989.
- [11] The LEP Electroweak Working Group. CERN-PPE/99-15.
- [12] M. Perl *et al.*. Phys. Lett. **B63** (1976) 466.
- [13] M. Perl *et al.*. Phys. Lett. **B70** (1977) 487.
- [14] DELCO Collaboration. Bacino *et al.*. Phys. Rev. Lett. **41** (1978) 13.
- [15] BES Collaboration. Bai *et al.*. Phys. Rev. **D53** (1996) 20.

- [16] CLEO Collaboration, Balest *et al.*, Phys. Rev. **D47** (1993) R3671.
- [17] OPAL Collaboration, G. Alexander *et al.*, Phys. Lett. **B374** (1996) 341.
- [18] ALEPH Collaboration, R. Barate *et al.*, Phys. Lett. **B414** (1997) 362.
- [19] B. Barish and R. Stroynowski, Phys. Rep. **157** (1988) 1.
- [20] E. Berger and H. Lipkin, Phys. Lett. **B189** (1987) 226.
- [21] CLEO Collaboration, Goldberg *et al.*, Phys. Lett. **B251** (1990) 223.
- [22] OPAL Collaboration, Ackerstaff *et al.*, Z. Phys **C75** (1997), 593.
- [23] Argus Collaboration, Albrecht *et al.*, Z. Phys **C58** (1993), 61.
- [24] CELLO Collaboration, Behrend *et al.*, Z. Phys **C23** (1984), 103.
- [25] M. Suzuki, Phys. Rev. **D49** (1994) 2634.
- [26] L3 Collaboration, Acciarri *et al.*, Phys. Lett. **B352** (1995) 487.
- [27] ALEPH Collaboration, Barate *et al.*, CERN-EP/99-026 (submitted to Eur. Phys. J. C)
- [28] H. Lipkin, Phys. Lett. **B72** (1977) 249.
- [29] H. Blundell, S. Godfrey, B. Phelps, Phys. Rev. **D53** (1996) 3712.
- [30] M. Suzuki, Phys. Rev. **D50** (1994) 4708.
- [31] H. Thacker and J. Sakurai, Phys. Lett. **B36** (1971) 103.
- [32] S. Eidelman *et al.*, Nucl. Phys. B (Proc. Suppl.), **55C** (1997) 181.
- [33] Y. S. Tsai, Phys. Rev. **D4** (1971) 2821.
- [34] T. Das, V. Mathur, and S. Okubo, Phys. Rev. Lett. **18** (1967) 761.

- [35] S. Jadach, Z. Wajs, R. Decker and J. H. Kühn. Comp. Phys. Comm. **76** (1993) 361.
- [36] ALEPH Collaboration. Barate *et al.*. CERN-EP/99-025 (submitted to Eur. Phys. J. C)
- [37] M. Finkemeier and E. Mirkes. Z. Phys **C69** (1996). 243.
- [38] E. Mirkes. Nuclear Physics B (Proc. Suppl.), **55C** (1997) 169-178.
- [39] ACCMOR Collaboration. C. Daum *et al.*. Nucl. Phys. **B187** (1981) 1.
- [40] TPC/2 ν Collaboration. D.A. Bauer *et al.*. Phys. Rev. **D50** (1994) R13.
- [41] ALEPH Collaboration. Eur. Phys. J **C1** (1998) 65.
- [42] B. A. Li. Phys. Rev. **D55** (1997) 1436.
- [43] European Laboratory for Particle Physics. Annual Report 1994. Volume II (1995).
- [44] OPAL Collaboration. K. Ahmet *et al.*. Nucl. Inst. and Meth. **A305** (1991) 275.
- [45] M. Arignon *et al.*. Nucl. Inst. and Meth. **A313** (1992) 103.
- [46] J.T.M. Baines *et al.*. Nucl. Inst. and Meth. **A325** (1993) 271.
- [47] D.G. Charlton, F. Meijers, T.J. Smith, and P.S. Wells. Nucl. Inst. and Meth. **A325** (1993) 129.
- [48] P. Billoir. Nucl. Inst. and Meth. **225** (1984) 352.
- [49] R. Fernow . *Introduction to Experimental Particle Physics*. Cambridge University Press, 1986.
- [50] M. Hauschild *et al.*. Nucl. Inst. and Meth. **A314** (1992) 74; O. Biebel *et al.*. Nucl. Inst. and Meth. **A323** (1992) 169.

- [51] M. Hauschild , Nucl. Inst. and Meth. **A379** (1996) 436.
- [17] OPAL Collaboration. K. Ackerstaff *et al.*, Eur. Phys. J. **C4** (1998) 193.
- [52] OPAL Collaboration. G. Abbiendi *et al.*, CERN-EP/99-095. (accepted by Eur. Phys. J.).
- [53] S. Jadach. B.F.L. Ward and Z. Was. Comp. Phys. Comm. **79** (1994) 503.
- [54] J. Allison *et al.*, Nucl. Instr. and Meth. **A317** (1993) 47.
- [55] R. Brun *et al.*, CERN DD/EE/84-1. 1984.
- [56] D.M. Manley and E.M. Saleski. Phys. Rev. **D45** (1992). 4002.
- [57] OPAL Collaboration. K. Ackerstaff *et al.*, Zeit. Phys. **C68** (1995) 555.
- [58] Rosen *et al.*, Phys. Rev. **D6** (1972) 1254.
- [59] Johnston *et al.*, Nouvo Cimento **6** (1957) 478.
- [60] Perkins *et al.*, Nouvo Cimento **4** (1956) 834.
- [61] DELPHI Collaboration. Abreu *et al.*, Phys. Lett. **B334** (1994) 435.
- [62] CLEO Collaboration. Battle *et al.*, Phys. Rev. Lett. **73** (1994) 1079.
- [63] DELCO Collaboration. G. B. Mills *et al.*, Phys. Rev. Lett. **52** (1984) 1944.
- [64] CLEO Collaboration. Coan *et al.*, Phys. Rev. **D53** (1996) 6037.
- [65] DELCO Collaboration. G. B. Mills *et al.*, Phys. Rev. Lett. **54** (1985) 624.
- [66] CLEO Collaboration. CLNS 98/1573 (submitted to Phys. Rev. D).
- [67] G.J. Feldman and R.D. Cousins. Phys. Rev. **D57** (1998) 3873.
- [68] D.B. Lichtenberg, Phys. Rev. **D10** (1974) 3865.